SAPIENZA
UNIVERSITÀ DI ROMA

INAF
ISTITUTO NAZIONALE
DI ASTROFISICA

Sapienza Università di Roma

Facoltà di Scienze Matematiche, Fisiche e Naturali

Istituto Nazionale di Astrofisica (INAF)

PhD in Astronomy, Astrophysics and Space Science
XXXVI cycle

Binary Neutron Star mergers in the multi-messenger era: from astrophysics to cosmology

Supervisor:
Dr. Luigi Piro

Co-supervisors:
Prof. Fulvio Ricci
Prof. Francesco Pannarale

Candidate:
Giulia Gianfagna
ID number 1665033

Academic year 2022/2023

ABSTRACT

In August 2017, the groundbreaking observation of GW170817 marked the first-ever identification of a binary neutron star merger, accompanied by the detection of a Gravitational Wave (GW) and a gamma-ray burst (GRB). The GRB exhibited prompt gamma-ray emission and an afterglow across radio, optical, and X-ray bands, originating from a relativistic jet formed post-merger at an angle of 20-30 degrees from its axis. This PhD thesis joins the GW and afterglow datasets of GW170817 through simultaneous fitting using Bayesian statistics. The key parameters shared between the two models, namely the inclination of the binary system (or viewing angle) and the luminosity distance, facilitate this joint analysis. The afterglow dataset includes a broadband light curve and the motion of the relativistic jet centroid over time. The thesis delves into significant challenges in both astrophysics and cosmology. In astrophysics, the investigation focuses on understanding the angular structure and energetics of the jet, influenced by its opening angle. The analysis of the GW and afterglow light curves reveals a jet opening angle and energetics consistent with population studies. Considering the centroid motion results instead in higher energetics compared to population studies. The jet's structure is discerned through the early rising phase of the afterglow, indicating a structured jet with an energetic core and less energetic wings. In the realm of cosmology, GWs emerge as a potent tool. The GW luminosity distance enables an independent estimation of the Hubble constant (H_0), crucial for addressing the Hubble tension. While a sole GW fit lacks the precision required for H_0, incorporating the afterglow light curve and centroid motion improves precision threefold. However, this precision has not yet reached the level of other cosmological H_0 estimations but may do so in the future. Additionally, the thesis explores future perspectives on new binary neutron star events.

PUBLICATIONS

I declare that this thesis and the work presented in it are my original own work. Part of it has already appeared previously in the following publications:

Joint analysis of gravitational-wave and electromagnetic data of mergers: breaking an afterglow model degeneracy in GW170817 and in future events, **Giulia Gianfagna**, Luigi Piro, Francesco Pannarale, Hendrik Van Eerten, Fulvio Ricci, Geoffrey Ryan, Eleonora Troja, *Monthly Notices of the Royal Astronomical Society*, Volume 523, Issue 3, August 2023, Pages 4771–4784, https://doi.org/10.1093/mnras/stad1728, [95].

Potential biases and prospects for the Hubble constant estimation via electromagnetic and gravitational-wave joint analyses, **Giulia Gianfagna**, Luigi Piro, Francesco Pannarale, Hendrik Van Eerten, Fulvio Ricci, Geoffrey Ryan, *Monthly Notices of the Royal Astronomical Society*, Volume 528, Issue 2, February 2024, Pages 2600–2613, https://doi.org/10.1093/mnras/stae198 [94].

CONTENTS

LIST OF FIGURES

LIST OF TABLES

INTRODUCTION

Binary neutron star (NS) mergers are astrophysical events where two NSs merge due to gravitational interactions. These mergers have gained particular attention in the field of multi-messenger astronomy.

Multi-messenger astronomy involves the simultaneous observation and study of astrophysical events using different types of messengers, such as electromagnetic (EM) waves (visible light, X-rays and radio waves), gravitational waves (GW), and high-energy particles. NS mergers provide a prime example of such studies. Indeed, they are powerful sources of GWs, ripples in spacetime predicted by Albert Einstein's theory of general relativity. They can be detected by ground-based GW observatories like LIGO (Laser Interferometer Gravitational-Wave Observatory) and Virgo, while the two NSs merge. After the merging, there is the emission of electromagnetic radiation across the entire spectrum, from gamma-rays to radio waves. In particular, a jet is formed, which emits a Gamma-ray burst (GRB), and the following afterglow. Another part of the merger ejecta, concentrated around the remnant, continues to emit light across the optical and infrared wavelengths, the so called kilonova emission. This radioactive-powered transient is produced by a neutron-rich material, indeed NS merger might be the primary source of heavy elements in the Universe.

By combining information from different messengers, we can gain a more comprehensive understanding of NS mergers and their implications for astrophysics. The first observed NS merger, known as GW170817, observed in 2017 [4], marked a groundbreaking event in multi-messenger astronomy, as it provided the first simultaneous detection of GW and EM radiation from the same event [5]. This has opened up a new era in our exploration of the universe, where multiple observational techniques converge to enhance our understanding of astrophysical phenomena.

In this thesis work, the GW170817 event is analysed, introducing for the first time a truly joint fit of some of the available data sets. In particular, the GW and the broad-band afterglow emission [141] will be joined, allowing to have a strong constraining power on the shared parameters between the two domains. The latter are the viewing angle (the angle between the jet axis and the observer line of sight), which corresponds also to the inclination of the binary system, and the luminosity distance. The main return from a joint analysis is the constraining power, not only on the shared parameters, but also on the parameters correlated to them. Generally, an independent information on one of the two correlated parameters can break this degeneracy. Such correlations afflict both the GW and the afterglow analyses. In the afterglow case, the viewing angle is correlated (or degenerate) with the jet width, the so called jet opening angle. In the GW case, the viewing angle is instead correlated with the luminosity distance.

The aforementioned method will be used to try to solve main issues on both astrophysics and cosmology. In particular, in the astrophysics of GRB jets, establishing the angular structure of the jet and its energetics, which are influenced by

the jet opening angle, is of primary importance. GRBs are collimated with rather narrow opening angles. The emission of the GRB and the early afterglow is visible only for observers within the jet opening angle (on axis), due to Doppler beaming limiting the visibility region to an angle $1/\gamma$, where γ is the bulk Lorentz factor of the jet treated as a whole, with typical value of ~ 100. The jet's γ is a rapidly decreasing function of time. This means that the collimation angle $1/\gamma$ with time will increase, up to the point of being comparable to the jet opening angle, this is the so called jet break. From this moment on, the observer can see the entire jet. The beaming of GRBs affects the estimation of the bursts true energy, but gives also information of the launching mechanism and on the central engine. Moreover, beaming affects the event rate. Indeed, the emission of the GRB is visible only to line of sights that intercepts the jet's cone, so the observed rate is smaller than the true one.

Before GW170817, the detected GRBs were mainly on axis, always identified thanks to the prompt emission, and often the assumption of a uniform jet was preferred with respect to a structured jet, usually composed by a more energetic core and less energetic wings. The typical light curve for on axis observers is decreasing, with a steepening after the jet break. The fact that GRBs are collimated with narrow opening angles, while the following afterglow could be observed over a wider angular range, led to the search for the so called orphan afterglows (afterglows which are not associated with observed prompt GRB emission). However, being off-axis, the expected flux is low, moreover, there is no information where to search and confusion with other transients is rather easy. So far there is no certain detection of orphan afterglows, however, the searches continue [122] and, recently, a claim of detection in the optical [138] has been published.

GW170817 is the first ever GRB seen off-axis, beyond any reasonable doubt. This conclusion is supported not only by the GW detection, but also by the low energy prompt emission, and by a peculiar light curve. The latter presents first a rising phase, typical of an off-axis observer, that with time, sees more and more the central energetic regions of the jet, as they enter the line of sight. Then a peak, representing the jet break, at around 170 days, and finally a decreasing slope. In this case, and in particular at early times, the assumption of a uniform jet is dangerous, the jet energy structure plays a crucial role before the jet break. Indeed, GW170817 early mild rising light curve was the first proof that jets have a structure. The assumption of the jet structure has to be done, before estimating the geometry (for example the jet opening angle) and energetics of the jet. Attention must be payed on how much this assumption influences these other parameters.

Another issue specific to the GW170817 afterglow light curve is that, at late times (after 500 days), there seems to be an excess in the X-ray and radio emission [225], which also strongly influence the analysis, possibly leading to biased results.

Binary NS mergers are also an important tool in cosmology. From the analysis of the gravitational waveform is possible to estimate the luminosity distance of the source, independently from any distance ladder. In the case of GW170817, the redshift of the host galaxy was measured, so, for the first time, it was possible to estimate the Hubble constant H_0 using GWs [3], this is the so called standard sirens method. This measure can be very useful in cosmology, because of the tension between the late and early time Universe H_0s. An independent measure can help in prefer one of the two. However, the error that we get from a solely GW analysis

is too wide, because of the degeneracy between the inclination of the system and the luminosity distance. An independent dataset is needed: the afterglow, and in particular, the study of the relativistic jet motion with time, thanks to the radio images from the Very Long Baseline Interferometry [93, 154].

In this thesis work, Chapter 1 provides an overview of the physical processes that interplay in a binary neutron star merger, from the GW emission, to the EM one. Chapter 2, instead, focuses on the method used to join the GW and EM messengers, through Bayesian statistic. Chapter 3 and Chapter 4 delve into the multi-messenger analysis of GW170817 and its results, showing its power and limitations. In these Chapters, in a gradual approach, the results of a GW only analysis, a GW and afterglow light curve joint analysis (Chapter 3), and a GW, jet afterglow light curve and relativistic jet motion analysis (Chapter 4) are presented. The level of precision on the parameters determination and their degeneracies are studied, depending on different assumptions and data sets included in the analysis. Finally, in Chapter 5 future perspectives on new binary NS events and the conclusions are given.

1

THE EMISSION FROM NEUTRON STAR BINARY MERGERS

Neutron stars (NSs) and Black Holes (BHs) are the most dense objects in the Universe. They can form binary systems that merge within the age of the Universe.

After a binary system of two NSs is formed, the two compact objects will lose energy in Gravitational Waves (GWs), causing the orbit to progressively shrink and the GW emission to increase with time, with its peak at the merger time, see Section 1.1. In the following few seconds after the merger, the disrupted matter from the NS is accreting in the form of a disk on the central remnant object. A small amount of fast-moving neutron-rich ejecta (see Fig. 1) emits an isotropic thermal emission, called kilonova, peaking in the infrared. A larger mass neutron-free wind along the polar axis produces kilonova emission peaking at optical wavelengths [137, 150]. This emission is not visible to edge-on (off-axis) observers because it is only visible within a range of angles and otherwise shielded by the high-opacity ejecta [212].

An enormous amount of energy, mainly from the accreting matter, is deposited in the polar regions near the compact remnant object, which launches an ultra-relativistic fireball. This outflow is collimated into a polar jet by the surrounding material and by magnetic fields. The emission from the jet, called Gamma-Ray Burst (GRB), is visible only for observers within the jet opening angle, due to Doppler beaming limiting the visibility region to $1/\gamma$, where γ is the *bulk* Lorentz factor of the jet treated as a whole, with typical value of $\gamma \simeq 100$.

The matter velocity in the jet is $\sim$ c. At 10^{12-13}cm from the star center, the jet reaches the photospheric radius, where light can escape for the first time [27]. At about this distance, the jet emits the prompt emission of the GRB, probably due to internal shocks in the jet, see Section 1.2.4. Other possible internal dissipation mechanisms, like magnetic reconnection, could be responsible for the prompt emission, however their nature is not yet clearly identified [28]. If, instead, the jet cannot escape the polar region, because of the presence of a significant amount of matter, it is "chocked".

The jet continues to speed away from the central engine, until it meets the surrounding circumburst material, with low typical densities of $\sim 10^{-4} - 1.0\text{cm}^{-3}$ (these limits include ~90% of the bursts [81]). This happens at the so called deceleration radius, 10^{16-17} cm [148]. At this point, the jet starts to decelerate and spread (see Fig. 1), γ decreases, the jet beaming angle grows, and synchrotron radiation is emitted across the entire EM spectrum. This emission is referred to as the afterglow, Section 1.2.5.

In this Chapter, the typical emission from these events is described, starting from GWs in Section 1.1, and GRBs in Section 1.2, focusing on the short ones. Then, the

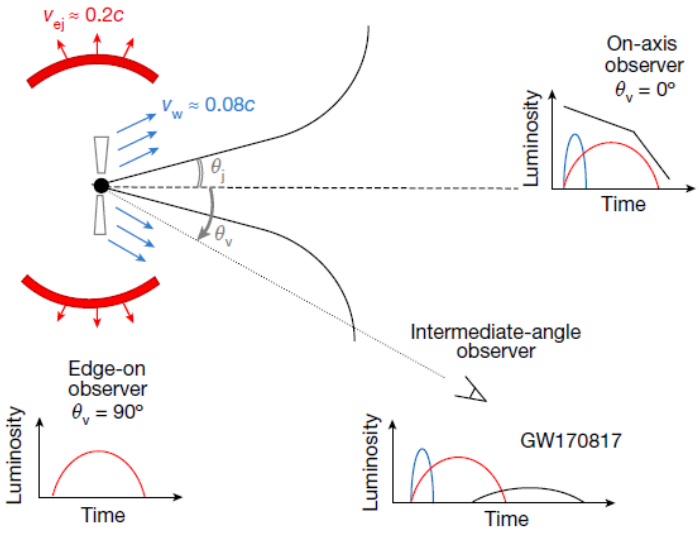

Figure 1: Schematic diagram of the geometry of GW170817 for an on-axis, an intermediate-angle and an edge-on observer. The neutron-rich matter that produces the kilonova in the infrared is represented in red, while the neutron-free matter which produces the kilonova in the optical is represented in lightblue. The relativistic jet is represented in black along the polar axis. The angle θ_j indicates the opening angle of the jet, while θ_v is the viewing angle of the observer. Figure from [227].

first ever detection of a binary NS merger, the so called GW170817, is described in Section 1.3.

1.1 GRAVITATIONAL WAVES

Almost a century after the prediction of the existence of GW by Einstein [70], the first signal from a binary BH was detected by the Laser Interferometer Gravitational Wave Observatory (LIGO [9]), GW150914 [9], in Fig.2. According to general relativity, the gravitational waves emitted by the merger of two compact objects in a quasicircular orbit are characterized by a chirplike time evolution, namely the more the orbit shrinks, the larger are the amplitude and the frequency of the wave, see Fig.2. The signal depends primarily on a combination of the component masses called the chirp mass [76] and on the mass ratio and spins of the components. In contrast to binary BH systems, the internal structure of the NS also impacts the waveform and needs to be included in the analysis for a proper description of the binary evolution.

1.1.1 *Gravitational waves detectors*

GWs are detected by measuring their effect on spacetime itself as the strain $h = \Delta L/L$ where ΔL is the fractional change of length L [2]. As an example, at a nearby distance of ~100 Mpc, the strain at Earth for a canonical binary NS merger is $\sim 10^{-21}$ [45], detection then requires the most sensitive ruler ever built. Experiments to detect gravitational waves began with J. Weber in the 1960's [241], using resonant-mass detector. The latter is made of a massive aluminum cylinder, few meters long and half a meter in diameter. The bar, held at room temperature, is

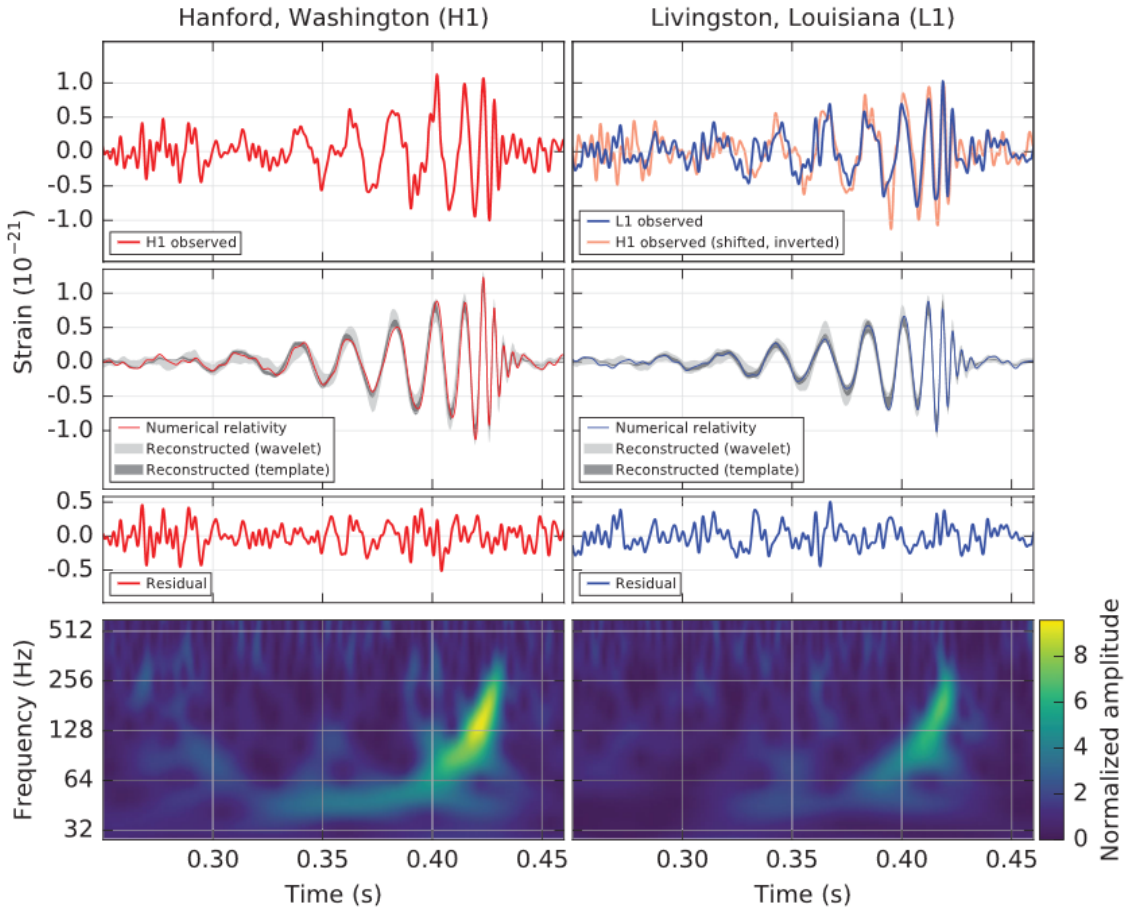

Figure 2: The gravitational-wave event GW150914 observed by the LIGO Hanford (H1, left column panels) and Livingston (L1, right column panels) detectors. Times are shown relative to September 14, 2015 at 09:50:45 UTC. For visualization, all time series are filtered with a 35–350 Hz bandpass filter. Top row, left: H1 strain. Top row, right: L1 strain. Second row: Solid lines show a numerical relativity waveform model for a system with parameters consistent with those recovered from GW150914. Shaded areas show 90% credible regions for two independent waveform reconstruction methods. Third row: Residuals after subtracting the numerical relativity waveform model from the detector strain. Bottom row: A time-frequency representation of the strain data, showing the signal frequency increasing over time. See more details in [9].

suspended in a vacuum chamber to isolate it from vibrations. A GW traveling perpendicular to the cylinder's axis will produce tidal forces that stretch and contract the length of the cylinder, inducing vibration at the first longitudinal mode of the bar. The main limitation on the sensitivity was due to the thermal noise, so that the following generation of detectors was made of bars at 4K. The international network of cryogenic resonant detectors reported just upper limits with sensitivities in the range of $10^{-20} - 10^{-21}$ cm over a length of ~ 1 m, in a frequency band of few hertz [20]. Interferometric detectors were first suggested in the early 1960's [89] and the 1970's [156]. As an improvement of such detectors, long baseline laser interferometers were proposed with arms of few kilometers. The suspended and isolated from vibrations mirrors permit to enlarge the detection bandwidth over a wide frequency range (from hundred to thousand hertz). Probing the space-time metric $\Delta L/L$ over kilometer distances, the detectors sensitivity and bandwidth was boosted to the respect of the resonant detectors. In early 2000's, a set of initial detectors was completed, creating a global network that included, for example, GEO 600 [14] in Germany, the Laser Interferometer Gravitational-Wave Observatory (LIGO) in the United States [2], and Virgo in Italy [12]. Combinations of these detectors made joint observations in the period 2002-2011, setting upper limits on a variety of gravitational-wave sources.

At present, a sensitive network of advanced detectors is composed by two Advanced LIGO detectors (Hanford, Livingston) [1] and Advanced Virgo [13]. LIGO and Virgo are Michelson Interferometers (invented in the 1880's [153]), they are L-shaped, have mirrors at the ends of the arms reflecting (hundreds of times) a laser beam in order to create an interference pattern on a photodetector. The latter senses the interference pattern, converting it into an electrical signal which can then be analyzed. LIGO's arms are 4 km long, while Virgo's are 3 km.

1.1.2 *Gravitational waves from binary systems*

In General Relativity GWs oscillate perpendicularly to the direction of propagation, travel at the speed of light and have only two independent polarization modes [244]. GR predicts that the induced strain $h(t)$ is perpendicular to the direction of propagation and is quadrupolar. This means that a wave, travelling along the z axis stretches, and then compresses, the space along the x axis, while compressing, and then stretching, the space on the y axis. This is the so called plus polarization $+$. For the other polarization, the stretch and compression occurs along axes rotated 45 deg relative to the x and y axes, the so called cross polarization $\times$, see Fig. 3.

Naming the strain amplitude from these modes h_+ and $h_\times$, respectively, the measured GW signal, $h(t)$, incident on a GW detector, can be written as a linear combination of the polarizations [112]

$$h(t) = F_+(\hat{w}, \hat{d})h_+(t) + F_\times(\hat{w}, \hat{d})h_\times(t), \tag{1}$$

where, $F_+, F_\times$ are the interferometer response to the two polarization modes, also called antenna pattern. Referring to Fig.4, they depend on $\hat{w} = (\hat{k}, \hat{e}_1, \hat{e}_2)$, where, $\hat{k}$ represents the GW propagation direction (that points toward Earth), while $\hat{e}_1, \hat{e}_2$ identify the wave front plane. Consequently, they also depend on ψ, the GW polarization angle in Fig. 4, right panel, which identifies the rotation of $\hat{e}_1, \hat{e}_2$ with respect to the the Equator [113]. Instead, $\hat{d} = (\hat{d}_a, \hat{d}_b, \hat{d}_c)$ represents the detec-

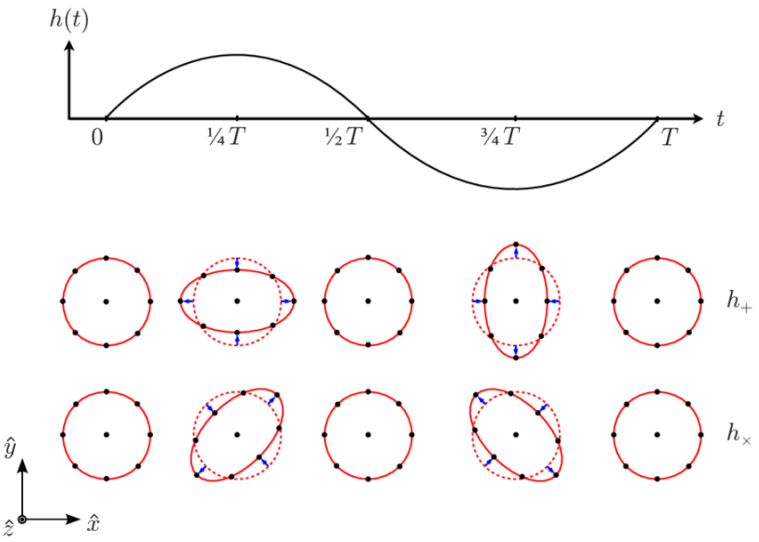

Figure 3: The effects of the + and × polarizations on a ring of particles, in a local inertial frame $(\hat{x}, \hat{y}, \hat{z})$, depending on the wave period fraction (top panel). The GW propagates along the $\hat{z}$ direction. Figure from [133].

tor geometry, the detector arms orientations are specified in terms of unit vectors $\hat{d}_a, \hat{d}_b$, the local vertical direction is along $\hat{d}_c$. I will not go into the details of these formulas, however, it is clear that the antenna patterns depends on the polarization angle and on the position in the sky of the source (needed to identify the vector $\hat{k}$) which is usually described by the polar θ and azimuthal ϕ angle (or the right ascension and declination). The position of the source θ, ϕ is determined from differences in signal arrival times at (at least) three widely separated detectors [73, 208, 242]. For this reason, the addition of KAGRA [19] and LIGO-India [229] will be fundamental.

Now we go into the details of the $h_{+,\times}$ formulations of eq.(1). Inspiraling compact binaries can be described, to lowest order, as two Newtonian point particles. In this case, the waveform generated by a source at luminosity distance d_L, corresponding to redshift z, is given by [58, 162]

$$h_+(t) = \frac{2(1+z)\mathcal{M}}{d_L}[\pi(1+z)\mathcal{M}f]^{2/3}(1+\cos^2(\theta_{JN}))\cos(2\Phi_N(t)), \tag{2}$$

$$h_\times(t) = -\frac{4(1+z)\mathcal{M}}{d_L}[\pi(1+z)\mathcal{M}f]^{2/3}\cos(\theta_{JN})\sin(2\Phi_N(t)), \tag{3}$$

$$\Phi_N(t) = \Phi_c - \left[\frac{t_c - t}{5(1+z)\mathcal{M}}\right]^{5/8}, f \equiv \frac{1}{\pi}\frac{d\Phi_N}{dt}, \tag{4}$$

f is the GW frequency, and

$$\mathcal{M} = \frac{(m_1 m_2)^{3/5}}{(m_1+m_2)^{1/5}}, \tag{5}$$

is the binary's chirp mass, which sets the rate at which f changes (units with $G = c = 1$ [162]). The angle θ_{JN} (θ_i in the left panel of Fig.4) describes the inclination of the binary's orbital plane to our line of sight: $\cos\theta_{JN} = \hat{J} \cdot \hat{N}$, we assume $\hat{J}$ to

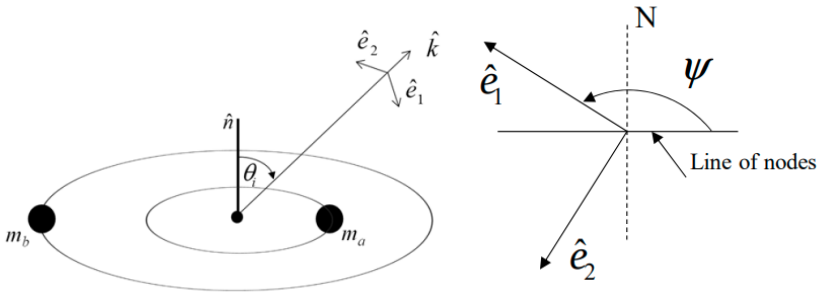

Figure 4: Left panel: A perspective view of the orbits for masses m_a and m_b, showing the definition of the inclination angle, θ_i, and unit vectors parallel to and transverse to the gravitational wave propagation direction $\hat{k}$. The unit vector $\hat{n}$ is perpendicular to the plane of the orbit and parallel to the system's orbital angular momentum. The gravitational wave unit vector $\hat{k}$ points from the binary center of mass to Earth. $\hat{e}_1$ lies in the $(\hat{n}, \hat{k})$ plane. $\hat{e}_2$ is perpendicular to that plane. Right panel: the definition of the gravitational wave polarization orientation angle ψ. $\hat{k}$ (not shown) points up and out of the page. The Line of nodes is the intersection of the wave front $(\hat{e}_1, \hat{e}_2)$ plane and Earth's equatorial plane. The dashed line is perpendicular to Earth's equatorial plane. N indicates Earth's North Pole. Figures from [113].

be alligned with the normal to the orbital plane, $\hat{n}$ in Fig.4, left panel, while $\hat{N}$ is parallel to $\hat{k}$. The parameters t_c and Φ_c are the time and orbital phase at the time of coalescence. Φ_N is the lowest order contribution to the orbital phase, typical of a Newtonian approximation. The post-Newtonian approximation, instead, provides a more accurate description of the gravitational radiation from inspiraling, stellar-mass binaries, where also, for example, spin and tidal effect corrections are included.

The phase, eq.(4), depends on the redshifted chirp mass $(1+z)\mathcal{M}$ [76]. Thus, measuring phase does not determine $\mathcal{M}$ or z independently, but only their product. Therefore, the strain, in eq.(1), depends on the redshifted chirp mass, the angles $(\theta, \phi, \theta_{JN}, \psi)$, and the luminosity distance d_L. By measuring the phase, the redshifted chirp mass is constrained sufficiently well that it decouples from the rest of the parameters (angles and luminosity distance). The latter, however, remain highly coupled and degenerate.

I will show in Section 1.3 and the following Chapters that the best way to break these degeneracies is to measure the event electromagnetically, like in the case of GW170817, this allows to fix the position in the sky and strongly constraint the inclination (and consequently the distance).

1.2 GAMMA RAY BURSTS

Gamma ray bursts are bright flashes of gamma–ray radiation, with variable duration from milliseconds to several hundreds of seconds. Most of their emission extends from several keV to tens of MeV, but also GeV emission has been discovered, see for example [147].

GRBs were discovered by chance in 1967 with the American Vela satellites [127], whose objective was to monitor the compliance of the Soviet Union to the nuclear test ban treaty. In the following years, thousands of events have been observed by several satellites. A big step forward was achieved with BATSE (Burst and

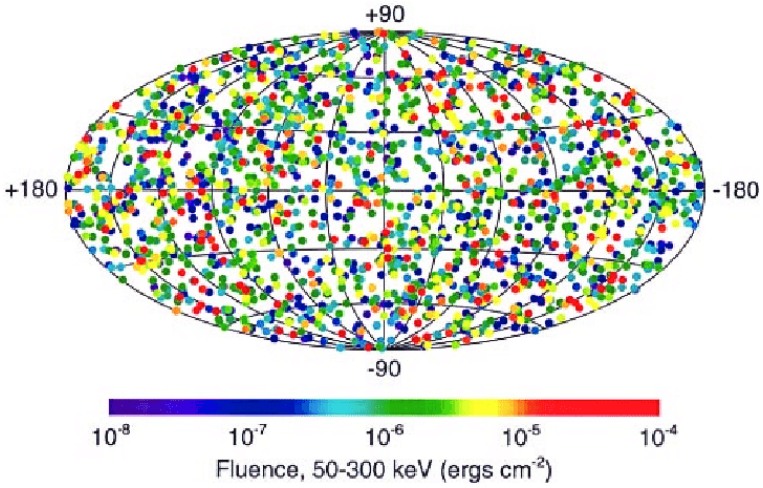

Figure 5: Distribution on the sky of 1825 GRBs observed by BATSE. The map shows burst locations (without indicating position uncertainties) in galactic coordinates. There are no preferred directions, either of galactic or extragalactic significance. Color code indicates total burst energy. Bursts are distributed isotropically, independent of their brightness, duration, spectrum, or any other characteristic. Figure from [111].

Transient Source experiment [78], operating between 1991 and 2000), that showed the isotropic distribution of the events in the sky [77], see Fig. 5. This suggested an extra-galactic origin, but a direct measurement of the distance of a single object was not available yet.

The distribution of the duration of GRBs observed by BATSE is bimodal, with a boundary at $\sim$ 2s, see Fig. 6 [129]. In the figure, T_{90} is the time interval over which 90% of the total background-subtracted counts are observed. The GRBs with $T_{90} > 2s$ are called long GRBs, while the ones with $T_{90} < 2s$ are the short GRBs.

The definitive step forward was done with BeppoSAX, the Italian satellite with Dutch participation [36], operating between 1996 and 2002. Thanks to this mission, the cosmological distance of GRBs was established, with the first GRB with a redshift estimation being GRB 970508 [176]. Moreover, the observed properties, like an energy release in gamma-rays up to $\sim 10^{54}$ erg (assuming isotropy) in a short time (tens of second), the non-thermal spectra, the short time variability (down to ms time scale), the photon energies > 1 MeV, were generally interpreted as a result of the formation of a fireball in relativistic expansion. This model, already developed before the BeppoSAX discoveries (e.g., [100, 106, 167]), had a prompt success: it explained spectral and temporal GRB properties (e.g., [243, 252]), through the conversion of the fireball kinetic energy into electromagnetic radiation. This conversion was assumed to occur through shocks between contiguous shells within the fireball for the prompt emission, or with the external medium for the afterglow emission (see, e.g.,[149, 168]). See Section 1.2.4 and 1.2.5.

The most important discovery by BeppoSAX is the establishing of the progenitor of long GRBs, namely a supernova. The location of the BeppoSAX GRB 980425 was found to be consistent with that of the type Ic supernova SN1998bw explosion [86]. Beside the location coincidence, the SN explosion was simultaneous, within one day, with GRB 980425, and, thence, the latter was the likely starting event.

While BeppoSax did observe short GRBs, it could not localize any of them, likely because of their limited emission in the soft X-rays. The *Neil Gehrels Swift* mission

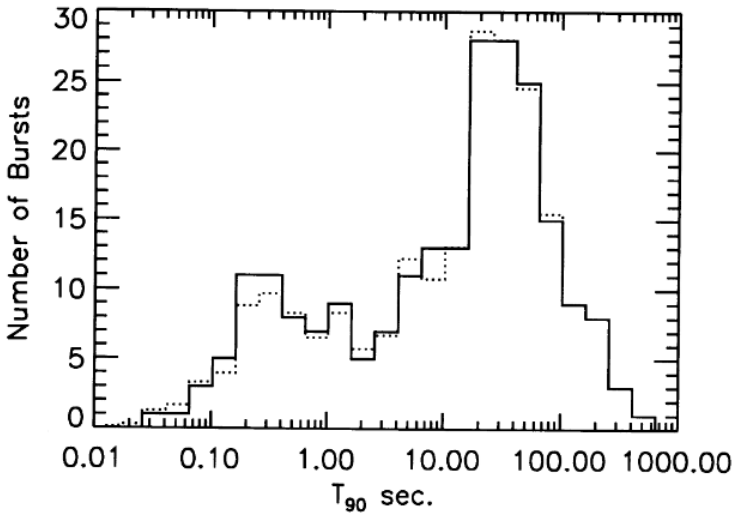

Figure 6: Distribution of the T_{90} for 222 GRBs in the BATSE catalog [129].

[24, 85, 87, 115, 234] launched in 2004, was instead primarily designed to chase GRBs and localize their rapidly fading afterglow. Indeed, *Swift* discovered the first short GRB afterglows in 2005. The lack of an associated supernova and the localization of some short GRBs to early-type galaxies confirmed the paradigm that collisions of two neutron stars form highly relativistic and collimated jets that power GRBs of short duration [69, 129, 190].

1.2.1 *Progenitors and host galaxies*

The long and short classes of GRBs are thought to have different origins: long GRBs are believed to be originated in core-collapse explosion of massive stars, while short GRBs are associated with merging of compact objects, both in the cases of binary NSs or NS-BH systems [69, 159]. The direct evidence confirming this theory is the emission of a supernova in the first case, and a kilonova in the second case.

In particular, long GRBs are formed through the so called Collapsar model [139, 248]. They arise from core-collapse explosion of a stripped-envelope massive star ([116] for a review), where matter flows towards a newly formed black hole or rapidly spinning, highly magnetized neutron star. Because of their progenitor short lifetime in the main sequence [117, 196], long gamma-ray bursts are found in star forming galaxies (as expected for young massive star progenitors) and in high density environments, as the massive star progenitor is expected to significantly enrich the surrounding environment with metals.

Short GRB progenitors, instead, originate from the evolution of massive stars in a primordial or "field" binary (a system born as binary in a star forming region) or by dynamical interactions and capture in globular clusters during their core collapse [79]. In primordial systems, the merging time is driven by the GW inspiral time, which is strongly dependent on the initial system separation [59]. The merger timescale distribution is broad, from tens of millions of years to much longer than a Hubble time [29, 44, 48]. Some systems are expected to drift away from the star-forming regions, before merging takes place, having experienced also a natal kick at the time of the formation of the compact object. For this reason, a fraction of the merging events should take place in the outskirts or even outside the galaxies,

in low density environments. Indeed, the offset with respect to the host galaxies, observed for the short GRBs, is usually larger with respect to long GRBs [80].

A low density circumburst environment is expected also for short GRBs of dynamical origin occurring in globular clusters. The two compact objects form separately and then become gravitationally bound. NSs and BHs will tend to gravitate toward the centre of the globular cluster, leading to higher chance of dynamical capture and an accelerated inspiral due to three-body interactions with other objects. Many binaries formed in globular clusters are ejected, because of three body interactions, and ultimately merge far from the cluster [26, 83].

As expected for young massive star progenitors, long GRBs are found to occur in star forming galaxies, as already mentioned above. Host galaxies of short GRBs are found to be significantly different instead. Short GRBs are associated to a mixed population of early and late-type host galaxies, indicating a wide range of stellar population ages. This, however, can be expected to be on average older with respect to the one associated to long GRBs [134].

There are some exceptions to this definition of short and long GRBs, with some mixed features or "hybrid" bursts. For example, GRB 211211A and GRB 230307A are long duration bursts (duration over 50s for both), which however were followed by a kilonova [135, 228]. GRB 060614, GRB 111005A and GRB 191019A are, again, long duration bursts (102 s, 26 s and 64 s duration respectively), but lack a supernova detection [88, 136, 152]. These seem to suggest that binary mergers can produce also long GRBs.

1.2.2 *The birth of the jet and its structure*

After the merger of the two compact objects, the jet is launced through the Blandford-Znajek mechanism [35]. Here, the rotational energy of a spinning BH is extracted in presence of a large-scale, poloidal magnetic field. The latter is sustained by an accretion disk, leaving a low density space in the polar regions. This mechanism is the same that produces other relativistic jets, for example in active galactic nuclei (AGN).

Once the jet is launched, there are two crucial phases [202]: the jet is within the dense ambient that surrounds the central engine, so the merger ejecta, and breaks-out from it; the jet encounter the external medium and subsequently decelerate. From the first phase, we have the emission of γ-rays, the so called prompt emission, from the second the afterglow, which is in the broad-band electromagnetic spectrum, from X-rays to radio wavelenghts, and it is the focus of this thesis.

The jet energy angular profile is often approximated to be uniform, the so called Top-Hat jet (see left panel in Fig.8). However, simulations of jets launched in realistic environments (see for example [101]) produce non-trivial lateral energy profiles, often containing an energetic core and power law tails or wings, see Fig. 7. Therefore, most GRB jets in nature are likely structured jets. The latter is a GRB jet model where the isotropic-equivalent energy of the blast wave is a function of the angle from the jet axis $E(\theta)$, see Fig. 8, right side. In this thesis we will see two different types of jet structures: the Gaussian and the power law jet, see Fig.7. The Gaussian structured jet has the energy that drops according to

$$E(\theta) = E_0 \exp(-\theta^2/2\theta_c^2), \tag{6}$$

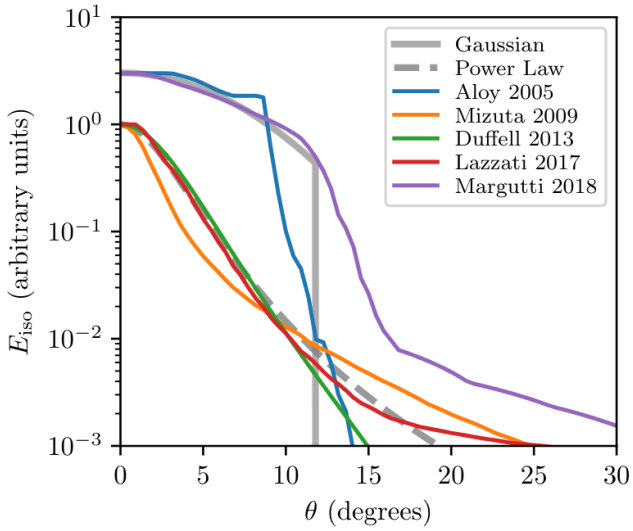

Figure 7: Lateral profiles of isotropic equivalent energy E_{iso} as a function of angle from the jet axis θ, individually rescaled to group similar profile shapes. The thick grey lines show fiducial profiles with simple analytic expressions (Gaussian and power law) while the thin colored lines show results from numerical simulations and analytic models chosen from the literature. See references and full description in [197].

up to a truncating angle θ_w. E_0, θ_c and θ_w are the on-axis isotropic equivalent kinetic energy of the blast wave, the jet opening angle and the jet total angular width, respectively. For the power law jet, instead, the energy is given by

$$E(\theta) = E_0(1 + (\theta^2/(b\theta_c^2))^{-b/2}, \tag{7}$$

where b is the power law index. The structure is determined by both the properties of the jet at launch and its interaction with the progenitor ambient medium. It is yet unclear if the jet is launched as uniform, and then becomes structured after the interaction with the ambient medium, or is launched as structured directly [200]. Moreover, Salafia et al. [201] introduce a distinction between what they call the *intrinsic* and the *apparent* structure of the jet. The *intrinsic* structure is intended as the energy emitted by different portions of the jet at different angular distances from the jet axis and it is due to the jet formation process itself or to the subsequent interaction of the jet with the merger ejecta. On the other hand, the *apparent* structure describes the energy received by observers that see the same jet under different viewing angles and depends on how relativistic beaming effects shape the emission from each part of the jet. The latter is the observed one, but from the former we can find out the actual jet energy budget.

The relativistic beaming effect plays a crucial role in the emission from the jet, with the majority of observable photon flux along a specific line of sight originating from emitting regions moving within an angle of $1/\gamma$ around that line of sight. In other words, there is no causal connection between regions at angular distances greater than $1/\gamma$. Consequently, an isotropic outflow is practically indistinguishable from one that radially expands within a collimation angle $\theta_c \geqslant 1/\gamma$ (the jet opening angle). Typically, the jet opening angle is determined by observing a steepening in the afterglow light curve, known as the jet break. This phenomenon occurs because the relativistic beaming angle $1/\gamma$ increases as the blastwave decelerates,

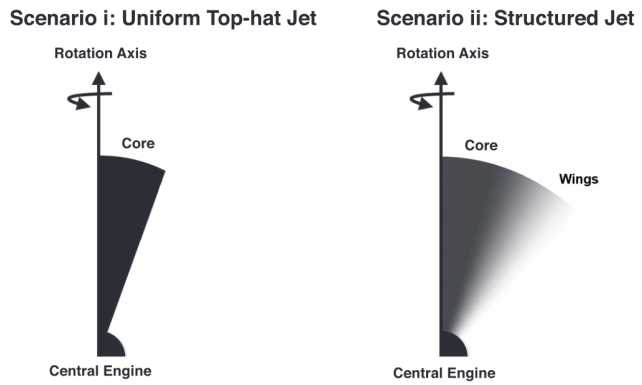

Figure 8: Two jet geometries, on the left a top-hat, with just a uniform core, on the right the structured jet, where there is a more energetic core and wings with decreasing energy on the sides. Figure adapted from [5].

reaching a point where it becomes comparable to the jet opening angle θ_c. From this juncture, the observer can see the entire jet. Once the causal contact starts, at the jet break, pressure waves will commence the lateral transfer of shock energy from the center to the outer regions of the jet. This mechanism gradually results in the dispersion of the energy profile of the jet [202].

Depending whether the observer viewing angle θ_v (the angle between the line of sight and the jet axis) is within or outside the jet core opening angle, the afterglow light curve of a structured jet changes. In the former case, the so called on-axis observer, the light curve is made of two power laws, separated by the jet break, see blue curve in Fig.9. Before the break, the flux is dominated by a small patch of emitting material (because of relativistic beaming) which is approximately uniform. After the break, the observer sees the whole jet, and the emission is dominated by the more energetic jet part, the core. Therefore, in both phases, the jet structure does not play a singificant role.

For off-axis observers (the line of sight is outside the jet opening angle), instead, during the early phase, the material from the energetic regions close to the jet axis progressively come into view [197]. The temporal evolution of the light curve depends both on the structure $E(\theta)$ and on θ_v. This results in a mildly decreasing or increasing light curve, see Fig. 9. This is followed by a jet break (which appear as a peak in the light curve for an intermediate θ_v, like the GW170817 case), after which the observer can be treated as on axis, as the whole jet is visible.

The afterglow light curve is mainly produced by syncrothron radiation, this will be explained in the following Section.

1.2.3 *Internal and External shocks and syncrothron radiation*

GRB jets are often discussed as an ultrarelativistically expanding fireball [174, 245, 250]. In particular, in the relativistic shocks that form in the ejecta, electrons are accelerated to relativistic energies and emit the observed emission via synchrotron radiation. The latter is non-thermal radiation emitted when relativistically charged particles are travelling in curved paths, so subjected to an acceleration perpendicular to their velocity [199].

The prompt emission of GRBs is thought to be produced by the internal shocks ($\gamma \sim 100$) [159, 168, 188]. These shocks arise in the relativistic flow produced by

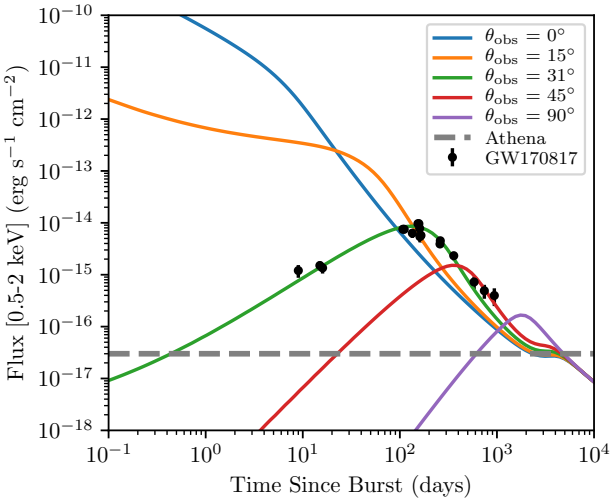

Figure 9: Light curves of a Gaussian 170817A-like jet at a distance of 41 Mpc at various viewing angles, parameters ($\theta_c = 5$ deg) and X-ray data taken from [224]. Figure from [178].

the source, when faster shells overtake slower ones, see Fig.10. These convert the kinetic energy to internal energy of accelerated particles, which in turn emit the observed gamma-rays. If the flow varies on a scale length L, see Fig.10, internal shocks would take place at $R_{int} \sim L\gamma^2$. Then, $L = c\Delta t$ can be inferred from the observed temporal variability, where $\Delta t \leqslant 1$ sec, indicating that these shocks take place at $\sim 10^{13}$ cm. The observed GRB duration corresponds to the time that the "inner engine" is active and the GRB time scales reflect the time scales of the "inner engine" [128]. In particular, the rapid temporal variability Δt of about 10 msec implies that the sources are compact (size of about 3000 km, $c\Delta t$). At such high energies, the photons can interact with other lower energy photons and produce electron-positron pairs ($\gamma' + \gamma' \rightarrow e^+ + e^-$, with γ' indicating the photons). If we estimate the optical depth for two photon pair production, assuming a typical fluence of 10^{-7} erg/cm^2 and the source size mentioned above, we find that it is very high, suggesting an optically thick source [175]. This, however, is in contrast with the observed non-thermal spectrum extending even above the pair production energy. This is the so called "Compactness problem". To solve it, relativistic effects come to our aid: if the emitting system is moving towards Earth at relativistic velocities, the observed photons are blue shifted and, therefore, their energy at the source frame is lower by a factor γ. Moreover, the implied size of a source moving towards us with Lorentz factor γ is $c\Delta t\gamma^2$, and not $c\Delta t$. With these corrections, the Lorentz factor needed for an optically thin source is ~ 100 [175].

The GRB prompt spectrum is usually characterized by a mathematical function invoking an exponentially-connected two-power-law function first proposed in a paper by the BATSE team [23]. The physical explanation for this function is not yet clear. However, as mentioned above, it is believed that the ultimate energy power source of a GRB comes from the synchrotron radiation of the electrons and the gravitational energy of the engine, released as the huge thermal energy in the fireball [253].

This thesis, however, will place particular emphasis on the afterglow emission and, for this reason, I will go into the details of the latter in the following text.

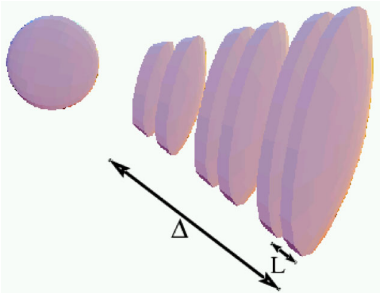

Figure 10: The internal shocks model. Faster shells collide with slower ones and produce the observed gamma rays. The variability time scale is $\Delta t = L/c$ while the total duration of the burst is Δ/c. From [175].

After the internal shock phase, the relativistic flow interacts with and is slowed down by the surrounding material [187], leading to external shocks that produce the afterglow. The external material may be the interstellar medium (in the case of short GRBs), or the pre-ejected stellar wind from the progenitor before the collapse (in the case of long GRBs). Focusing on short GRBs, we assume to have a constant density of the medium. Initially, before it starts to deceletate, there is a *coasting* phase, where the blast wave is at a constant Lorentz factor. Then external shocks become effective, at the so called deceleration radius, $\sim 10^{15} - 10^{16}$ cm [175, 204]. At this radius, the initial bulk Lorentz factor has decreased to approximately half its original value, as the fireball ejecta is decelerated by the swept-up external matter.

In this phase, the dynamic of the blast wave can be modeled rather well by the Blandford-McKee solution [34]. This model is a self-similar spherical solution describing an adiabatic ultra relativistic ($\gamma >> 1$) blast wave, approximated as a narrow shell, in which the shocked material is concentrated. The solution is determined completely from the explosion energy E and the circumburst number density n_0. The shock front fluid Lorentz factor γ is related to the explosion time t (in the observer frame) by [240]

$$\gamma(t) \propto \left(\frac{E}{\pi m_p n_0 c^5 t^3}\right)^{1/8}, \tag{8}$$

with m_p the proton mass and c the speed of light, while the shock radius $R(t)$ is given by

$$R(t) \propto \left(\frac{Et^5}{\pi m_p n_0 c}\right)^{1/8}. \tag{9}$$

While the majority of GRB observations occur during the just described relativistic phase, a considerable amount of time later, as the blast wave undergoes significant deceleration, it transitions from the ultra-relativistic regime to the Newtonian Sedov-Taylor solution [210, 221]. This phase, for example in the case of GW170817, is at $\sim$ 13000 days (see Chapter 4), which are about 30 years. In this case the shock radius, for a fixed adiabatic index 5/3 [66], is given by

$$R(t) \propto \left(\frac{Et^2}{m_p n_0}\right)^{1/5}. \tag{10}$$

In this classical approximation, the speed of light c does not appear and the shock front Lorentz factor is approximately one. An estimate for the turning point [175]

from the Blandford-McKee to the Sedov-Taylor solution, R_{NR}, can be made by equating the explosion energy to the total rest-mass energy that is swept up:

$$E = m_p n_0 c^2 \frac{4}{3}\pi R_{NR}^3, \tag{11}$$

this returns the approximate radius at which the original explosion energy in the blast wave is no longer dominant over its rest-mass energy, also called Sedov lenght, typical value is: $R_{NR} \sim 10^{18}$ cm [175, 239].

The afterglow emission is reasonably well described by synchrotron from accelerated electrons when a spherical relativistic shell collides with the external medium and creates a relativitic shock with Lorentz factor γ. In this case, we assume that the medium is uniform. Sari et al. [205] estimate the afterglow observed emission as a series of power law segments in time and in frequency:

$$F_\nu \propto t^{-\alpha}\nu^{-\beta}. \tag{12}$$

In the case of the spectrum, the power law segments are separated by three main break frequencies: the cooling frequency ν_c, the typical synchrotron frequency ν_m and the self absorption frequency ν_a. These are estimated through synchrotron theory, as will be shown below. In the case of the light curve, the power law segments are divided by break times. Across these break times and frequencies the exponents of these power laws change.

The synchrotron spectrum is produced by the interaction between the electrons e in the shock and the magnetic field B. For this reason, the main parameters used to model this emission are: the fraction ϵ_e of the shock energy that goes into the electrons; the fraction ϵ_B into the magnetic field; the density of the medium n_0 and the Lorentz factors of the blast wave and of the electrons. In the shock, the electrons, with Lorentz factor γ_e, are accelerated to a power law distribution of the type

$$N(\gamma_e)d\gamma_e \propto \gamma_e^{-p} d\gamma_e, \tag{13}$$

where $p > 2$ to keep the energy of the electrons finite. This is valid as long as γ_e is larger than a minimum Lorentz factor γ_m. The latter (in the ultra-relativistic case), assuming that a constant fraction ϵ_e of the shock energy goes into the electrons, is

$$\gamma_m = \epsilon_e \frac{p-2}{p-1}\frac{m_p}{m_e}\gamma \tag{14}$$

with m_e the mass of electrons. Assuming that the magnetic energy density behind the shock is a constant fraction of the shock energy, the magnetic field strenght is given by

$$B = (32\pi m_p \epsilon_B n_0)^{1/2}\gamma c. \tag{15}$$

The typical energy of synchrotron photons depends on the Lorentz factor γ_e of the relativistic electron under consideration and on the strength of the magnetic field B:

$$\nu(\gamma_e) = \gamma\gamma_e^2 \frac{q_e B}{2\pi m_e c} \tag{16}$$

where q_e is the electron's charge. The factor γ is needed to transform the frame of the shocked fluid to the observer frame. The synchrotron radiation power is

$$P(\gamma_e) = \frac{4}{3}\sigma_T c\gamma^2\gamma_e^2\frac{B}{8\pi} \tag{17}$$

with σ_T the Thompson scattering cross section. Also in this case, the factor γ^2 is needed to transform the frame of the shocked fluid to the observer frame.

The instantaneous synchrotron spectrum of a single relativistic electron with an initial energy $\gamma_e m_e c^2$ is approximately a power law with $F_\nu \propto \nu^{1/3}$ up to $\nu(\gamma_e)$ and an exponential decay above it. The peak power occurs at the synchrotron frequency $\nu(\gamma_e)$ and is independent on γ_e:

$$P_{\nu,max} \approx \frac{P(\gamma_e)}{\nu(\gamma_e)} = \frac{m_e\sigma_T c^2}{3q_e}\gamma B \tag{18}$$

The position of the peak, instead, depends on γ_e. If the electron is energetic it will cool rapidly until it will reach γ_c, the Lorentz factor of an electron that cools on a hydrodynamic time scale. This is estimated as $\gamma\gamma_c m_e c^2 = P(\gamma_e)t$, so

$$\gamma_c = \frac{6\pi m_e c}{\sigma_T\gamma B^2 t} = \frac{3m_e}{16\sigma_T\epsilon_B m_p c\gamma^3 n_0 t} \tag{19}$$

where t refers to the time in the observer frame.

To calculate the net spectrum from a power-law distribution of electrons, an integration over γ_e is needed. There are two different cases, depending on whether $\gamma_m > \gamma_c$, fast cooling, or $\gamma_m < \gamma_c$, slow cooling. Let the total number of swept-up electrons in the post-shock fluid be $N_e = 4\pi R^3 n_0/3$. When $\gamma_m > \gamma_c$, all the electrons cool down to roughly γ_c, and the spectral power at ν_c is approximately $N_e P_{\nu,max}$. We call this the case of fast cooling. The flux at the observer, F_ν, is given by

$$F_\nu = \begin{cases} (\nu/\nu_c)^{1/3} F_{\nu,max} & \nu < \nu_c \\ (\nu/\nu_c)^{-1/2} F_{\nu,max} & \nu_c < \nu < \nu_m \\ (\nu_m/\nu_c)^{-1/2}(\nu/\nu_m)^{-p/2} F_{\nu,max} & \nu > \nu_m \end{cases} \tag{20}$$

where $\nu_m \equiv \nu(\gamma_m)$ and $F_{\nu,max} \equiv N_e P_{\nu,max}/4\pi D^2$ is the observed peak flux at distance D from the source.

When $\gamma_m < \gamma_c$, only those electrons with $\gamma_e > \gamma_c$ can cool. We call this slow cooling, because the electrons with $\gamma_e \sim \gamma_m$, which form the bulk of the population, do not cool within a time t, and we have

$$F_\nu = \begin{cases} (\nu/\nu_m)^{1/3} F_{\nu,max} & \nu < \nu_m \\ (\nu/\nu_m)^{-(p-1)/2} F_{\nu,max} & \nu_m < \nu < \nu_c \\ (\nu_c/\nu_m)^{-(p-1)/2}(\nu/\nu_c)^{-p/2} F_{\nu,max} & \nu > \nu_c \end{cases} \tag{21}$$

The typical spectra corresponding to fast and slow cooling are shown in Fig.11a, b.

In addition to the various power-law regimes described above, synchrotron self-absorption influences the spectrum at low frequencies, where relativistic electrons can absorb the photons produced earlier by other electrons [175]. This causes a

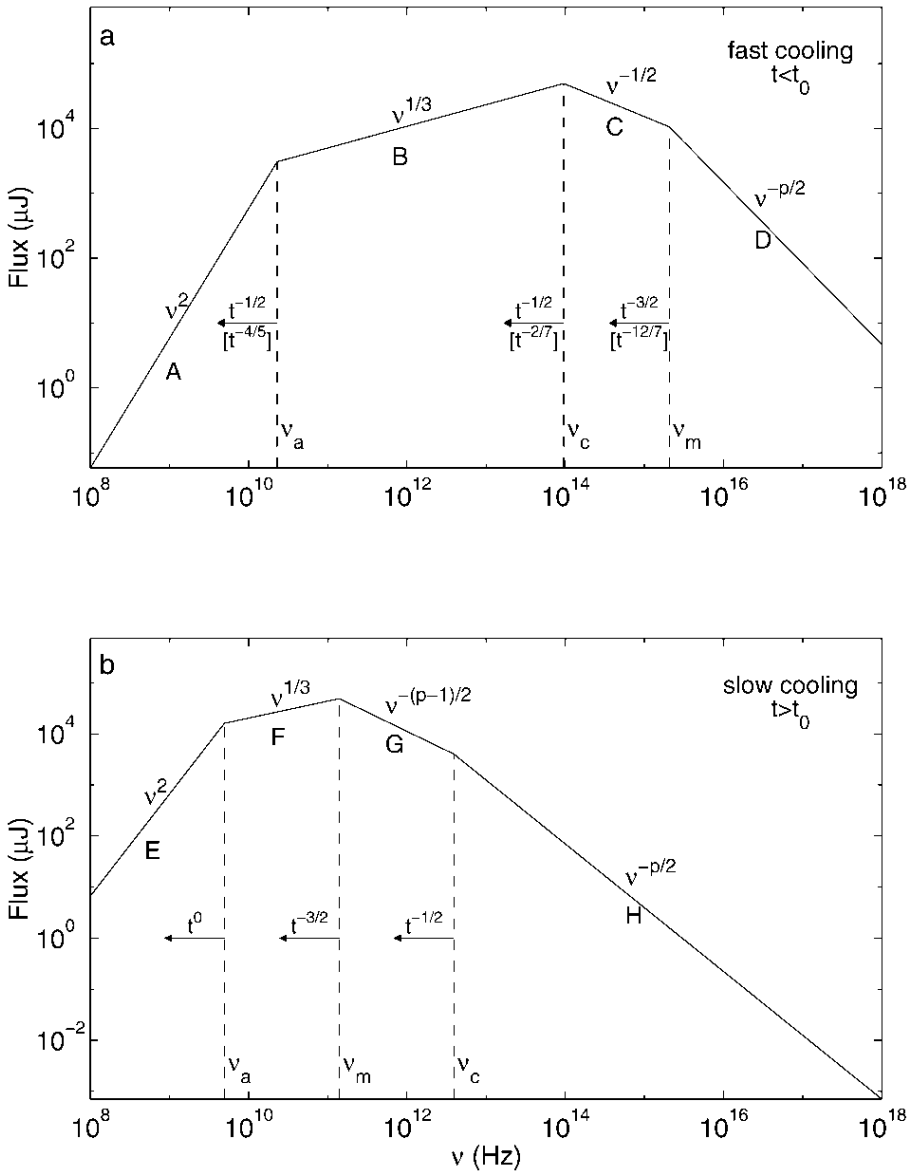

Figure 11: 1.—Synchrotron spectrum of a relativistic shock with a power-law electron distribution. (a) Fast cooling, which is expected at early times. The spectrum consists of four segments, identified as A, B, C, and D. Self-absorption is important below ν_a. The frequencies, ν_m, ν_c, and ν_a, decrease with time as indicated; the scalings above the arrows correspond to an adiabatic evolution, and the scalings below, in square brackets, correspond to a fully radiative evolution, which we are not taking into account in this thesis. (b) Slow cooling, which is expected at late times. The evolution is always adiabatic. The four segments are identified as E, F, G, and H. Figure from [205].

steep cutoff of the spectrum at low frequencies [125, 126, 240]. This regime is shown in Fig.11.

Another emission mechanism that could play a role is inverse Compton scattering (when $\epsilon_B > \epsilon_e$). In view of the high energies involved a photon is inverse Compton scattered only once. After a single scattering the photon's energy is so high that in the electron's rest frame it is above the Klein-Nishina energy, and the decrease in the Compton cross section in this energy range makes a second scattering unlikely [199, 232].

From the scalings for $\gamma(t)$, eq.(8), and $R(t)$, eq.(9), of the Blandford-McKee solution, we can estimate the variation with time, and their dependencies with respect to the shock physical quantities, of the characteristic frequencies [104, 205]. In particular, using eq.(16) and, respectively, eq.(19) and eq.(14), we get

$$\begin{aligned} \nu_c &= 2.7 \times 10^{12} \epsilon_B^{-3/2} E_{52}^{-1/2} n_0^{-1} t_d^{-1/2} \text{Hz} \\ \nu_m &= 5.7 \times 10^{14} \epsilon_B^{1/2} \epsilon_e^2 E_{52}^{1/2} t_d^{-3/2} \text{Hz} \end{aligned} \tag{22}$$

where $E_{52} = E/10^{52}$ ergs, n_0 in units of cm^{-3} and t_d is t in days, i.e. [104, 170, 205]. From eq.(18), instead, we get

$$F_{\nu,max} = 1.1 \times 10^5 \epsilon_B^{1/2} E_{52} n_0^{1/2} D_{28}^{-2} \mu\text{Jy}, \tag{23}$$

with $D_{28} = D/10^{28}$ cm. The ν_c decreases with time slower than ν_m. Therefore, at sufficiently early times, $\nu_c < \nu_m$, fast cooling, while at later times, $\nu_c > \nu_m$, slow cooling. The transition between the two occurs when $\nu_c = \nu_m$, at $210 \epsilon_B^2 \epsilon_e^2 E_{52} n_0$ days [205].

The instantaneous sprectra do not depend on the hydrodynamic evolution of the shock. The light curves at a given frequency, however, depend on the temporal evolution of various quantities, such as the break frequencies ν_m and ν_c and the peak flux $F_{\nu,max}$. These in turn depends on the variation of the physical quantities along the shock front, as seen above. See Section 1.2.5 for more details.

1.2.4 *Prompt emission*

The prompt emission for short GRBs lasts about 2 s, while the one of long GRBs lasts more than 2 s.

One of the main properties of short GRBs is that their prompt emission spectrum is harder than the one of long GRBs [129], see Fig.12a, however, this difference becomes less significant when the analysis is resticted to the first 1 or 2 s of the long GRBs prompt emission [90, 91].

The null spectral lag is another characteristic feature of short GRBs [163], see Fig.12b, the interpretation for this is still not clear, it could be related to curvature effects of shocked shells [59].

Another important indicator is the so called "Amati relation". The latter concerns the correlation between the redshift-corrected photon energy E_{peak}, at which the νF_ν spectrum peaks, and the total released energy during the burst E_{iso} in the hypothesis of isotropic emission. It was found with a set of BeppoSAX GRBs, whose redshift was determined with optical spectrometers [15]. Up to now, the robusteness of the Amati relation is confirmed by all long GRBs observations [16]. Instead, the majority of short GRBs are found to be at more than 3σ from the long

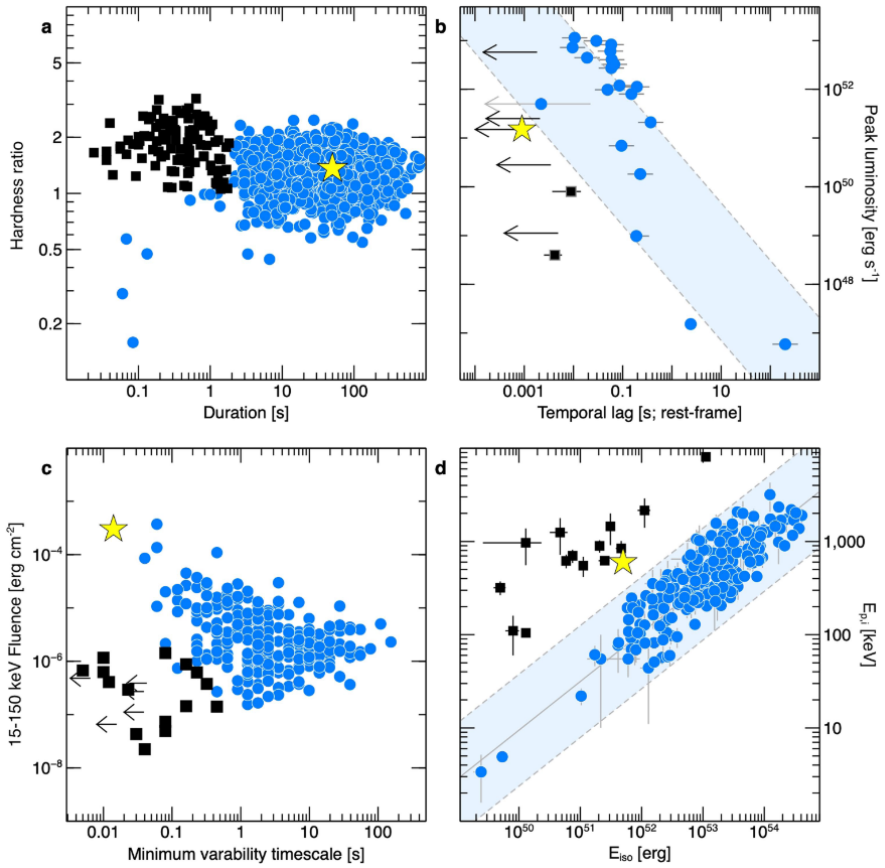

Figure 12: The traditional GRB classification, based on the duration/hardness ratio diagram (a), is not unambiguous. Additional classifiers, used to break the degeneracy, are the lag–luminosity relation (b), the variability timescale (c) and the Amati relation (d). Long GRBs (circles) and short GRBs (squares) occupy different regions of these plots. Dashed lines show the boundaries of the long GRB regions (shaded areas). GRB 211211A (star symbol) belongs to the class of long soft bursts (a), but its other high-energy properties are common among short GRBs. Error bars represent 1σ; upper limits (arrows) are 3σ. From [228].

GRBs $E_{peak} - E_{iso}$ correlation, and mainly in the left side, see Fig.12d. This could be suggesting the existence of the same correlation for short GRBs, but with a different normalization ([59] and references therein).

Moreover, in general the short-duration bursts have a variability time scale that is significantly shorter than long-duration bursts, see Fig.12c. Many link the rapid variability directly to the activity of the central engine [32, 98, 140].

Finally, a fraction of short GRBs have an extended gamma-ray emission, lasting $\sim$ 10s and sometimes rising with a delayed onset. The spectrum is softer with respect to the prompt one [131]. The GRBs with such emission could be produced by a different progenitor [132, 164] or the softer emission could be due to a newly-born magnetar [99, 151].

In Fig.12 the hybrid GRB 211211A is highlighted with a star symbol. This GRB, as mentioned above, has a long duration, but its other high-energy properties are common among short GRBs, suggesting a compact merger origin.

1.2.5 *Afterglow emission*

In both field or dynamical binaries, the low density medium gives rise to fainter afterglows, setting in at later times than those of long GRBs [171, 203]. This is also due to different energetics, the short GRB afterglow is fainter because they are less energetic than long GRBs [59]. The afterglow can be observed in a braod range of frequencies, from the radio to the X-rays.

The temporal behaviour of X-rays afterglows can be well described by a power law or a series of connected power laws, separated by break times [143, 183], see for example Fig. 13. In general, the majority can be well fitted using a single power law or a double power law with a jet break [71, 81], for afterglows best described by a single powerlaw, the temporal slope $-\alpha$, see eq.(12), is about -1 [71, 81]. Instead, for short GRBs with light curves best described by the broken powerlaw model, the second slope is found to be in the range [-1.5, -0.3]. In the X-ray light curve, there are some deviations from this standard afterglow model, like steep early decay, flares and plateaus. The former (at $t < 1000s$) is believed to be due to the prompt emission [46, 52, 130, 142, 165, 220]. The nature of the plateau phase is still debated, the accepted explanation is that it is resulting from a combination of the emission from the external forward shock and the energy injection coming from the central engine [254]. The late-times X-ray flares (or excess) are found also in long GRBs, they are likely due to the central engine, which could remain active and variable for long time, or to magnetic dissipation during the deceleration of the jet [30].

The spectral index, β in eq.(12), is found to be in the range 0.15 and 1.9 [71]. As an example, in the case of GW170817 (see Section 1.3), β is 0.58 ± 0.01 [226]. This measurement is quite solid, thanks to the extensive sampling of the spectrum from X-rays to radio over a very long time scale (years). For this event, ν_m is always below the radio band, while ν_c is above the X-ray band, therefore, the slope of the spectrum is given by $-(p-1)/2$, see also eq.21 and Fig.11, bottom panel. From this, also a high precision on p follows [145].

The median jet opening angle θ_c for short GRBs is about 6 deg [71, 81].

In the on-axis case, the afterglow light curves are not influenced by the structure of the jet. Using the spectral and temporal indices and the relations given by the synchrotron model, see Section 1.2.3, the three break frequencies of the synchrotron spectrum can be estimated and the burst physical properties, like the energy of the jet E_0 (isotropic-equivalent kinetic energy), the density of the circumburst environment, n_0. For the sample of short GRBs selected in [71, 81], n_0 is $0.7 \times 10^{-5} - 0.8 cm^{-3}$ and $E_0 \approx 3 \times 10^{49} - 9 \times 10^{53}$ erg. The off axis case, instead, is more complicated, the emission is still a broken power law, but with slopes and break times dependent on the viewing angle and on the jet structure.

1.3 GW170817

According to the accepted short GRBs origin, where collisions of two neutron stars form highly relativistic and collimated jets that power gamma-ray bursts, gravitational wave events from such mergers should be associated with GRBs. The majority of these bursts should be seen off-axis, that is, they should point away from Earth [191, 209].

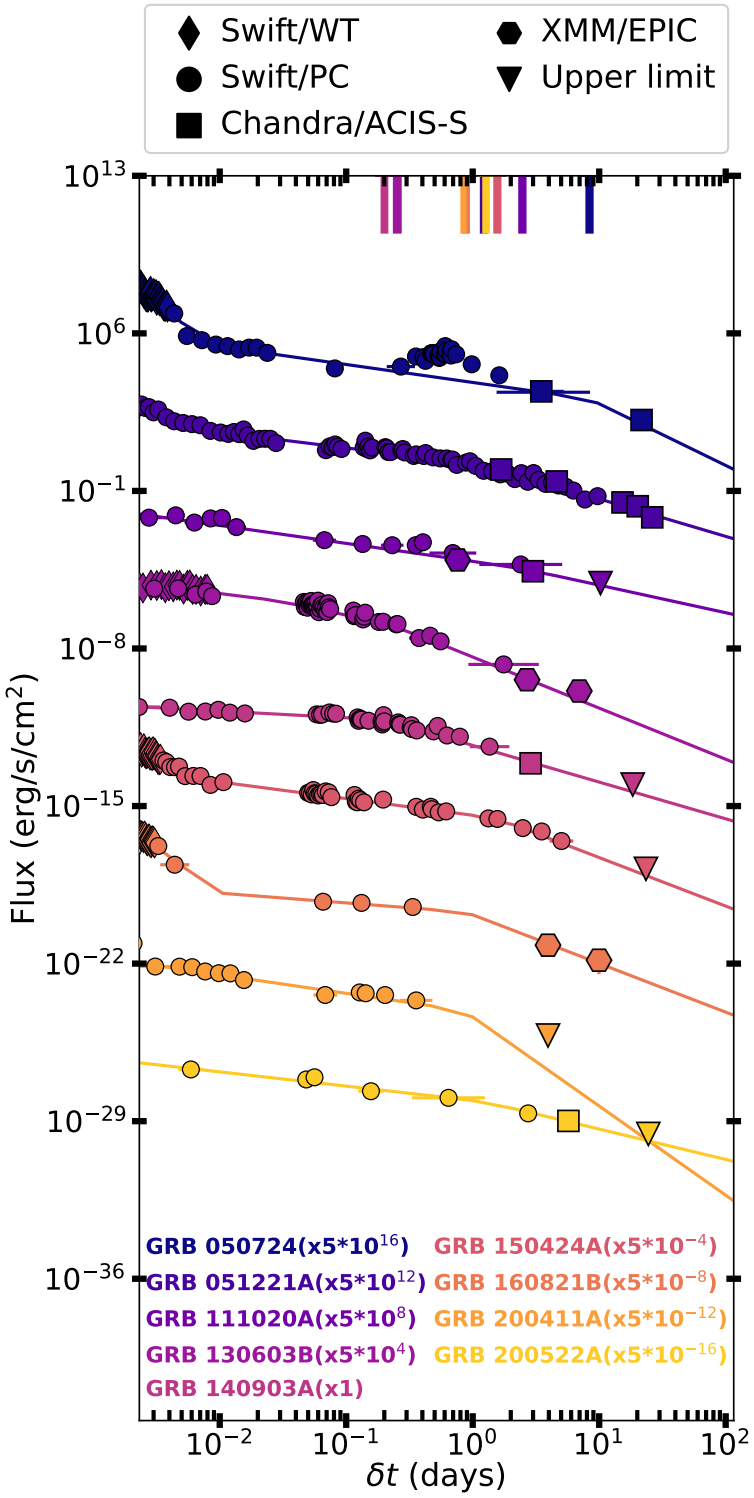

Figure 13: 0.3-10 keV unabsorbed X-ray flux light curves of short GRBs with detected jet breaks. All short GRBs are color-coded with their corresponding best-fit models (solid lines). Symbols indicate each set of observations obtained by different observatories or observing modes (top legend). Triangles indicate 3σ upper limits. Vertical lines from the top show the times of the jet breaks for each short GRB. Calculated uncertainties correspond to 1σ. From [71].

In GW170817, we first detect the kilonova emission in the optical and then, after some days, the afterglow in the X-ray and radio bands. This is because the observer, in this case, is viewing the system beyond the opening angle of the jet, θ_j in Fig. 1, and relativistic beaming weakens the emission in the observer direction [227]. The afterglow only becomes visible once the jet has spread and decelerated sufficiently that the beaming cone of the emission includes the observer. Therefore, an off-axis observer sees that the onset of the afterglow is delayed by several days or weeks. Indeed, on August 17, 2017, two Advanced LIGO detectors [1] and Advanced Virgo [13] observed the neutron star binary inspiral event GW170817 [4, 5], which was followed by GRB 170817A [96, 206]. GRB 170817A was detected by the Fermi Gamma Ray Telescope [96] and INTEGRAL [206] only 1.7 sec after the gravitational wave trigger, see Fig. 14. After that, observations targeted the localization region of the short GRB, and indeed, almost 11 hours later, the Swope team [57] identified another electromagnetic counterpart, the kilonova emission [72]. The source, in the optical, infrared and ultraviolet, called AT 2017gfo, is in the galaxy NGC 4993, at almost 40 Mpc distance. 9 days after the detection of the GW, on 26 August 2017, the Chandra X-ray Observatory detected the X-ray afterglow emission at the position of AT 2017gfo [227]. In September of the same year there was the detection of the radio afterglow by VLA (Very Large Array [109]) and ATCA (Australia Telescope Compact Array [226]).

In October 2017, March 2018 and April 2018 [93, 154] very long baseline interferometry observations were performed. Thanks to the high spatial resolution (~mas order), the source size was constrained to be smaller than 2.5 mas, and superluminal apparent motion was detected. These observations were fundamental to discern between two possible scenarios [109, 144]: a radially structured velocity profile of a nearly isotropic outflow (the "chocked" jet scenario) or an off-axis structured jet. Both models can explain the slow rise of the light curve and the late time peak. However, the very small size of the radio source and the superluminal motion, points to the structured jet, being the size of the isotropic outflow larger, and the velocity milder.

This event opened the way for multi-messenger astrophysics and confirmed the compact binary progenitor model for at least some sGRBs.

The afterglow light curve of GW170817 will be presented in Chapter 3. The observations in the X-ray and radio frequencies present a mild early rising phase, which was fundamental to asses the inclination and geometry of the jet. It is typical of a structured jet, indeed both a Gaussian and a power law structure fit well the broad band light curves. On the contrary, the uniform Top-Hat jet is characterized by a steeper slope and a decline starting closer to the merger time. The rising slope also points to an off-axis jet [68]. The rising phase give information not only on the viewing angle, but also to the jet opening angles. In particular, in the Gaussian jet case, the early phase slope depends on the ratio of these two angles, leading to a degeneracy. In Chapter 3 we will see that this degeneracy can be broken including an independent data set, which are GWs. This can be done because also GW encodes information on the viewing angle or inclination of the system.

After the rising phase, we see the peak of the emission, the jet break, at around 170 days, followed by a decreasing phase. At present, GW1708017 is being monitored in the radio (ATCA and VLA [21, 22]) and X-ray (*Chandra*) bands, but its emission is very near, if not below, the sensitivity of the available instruments.

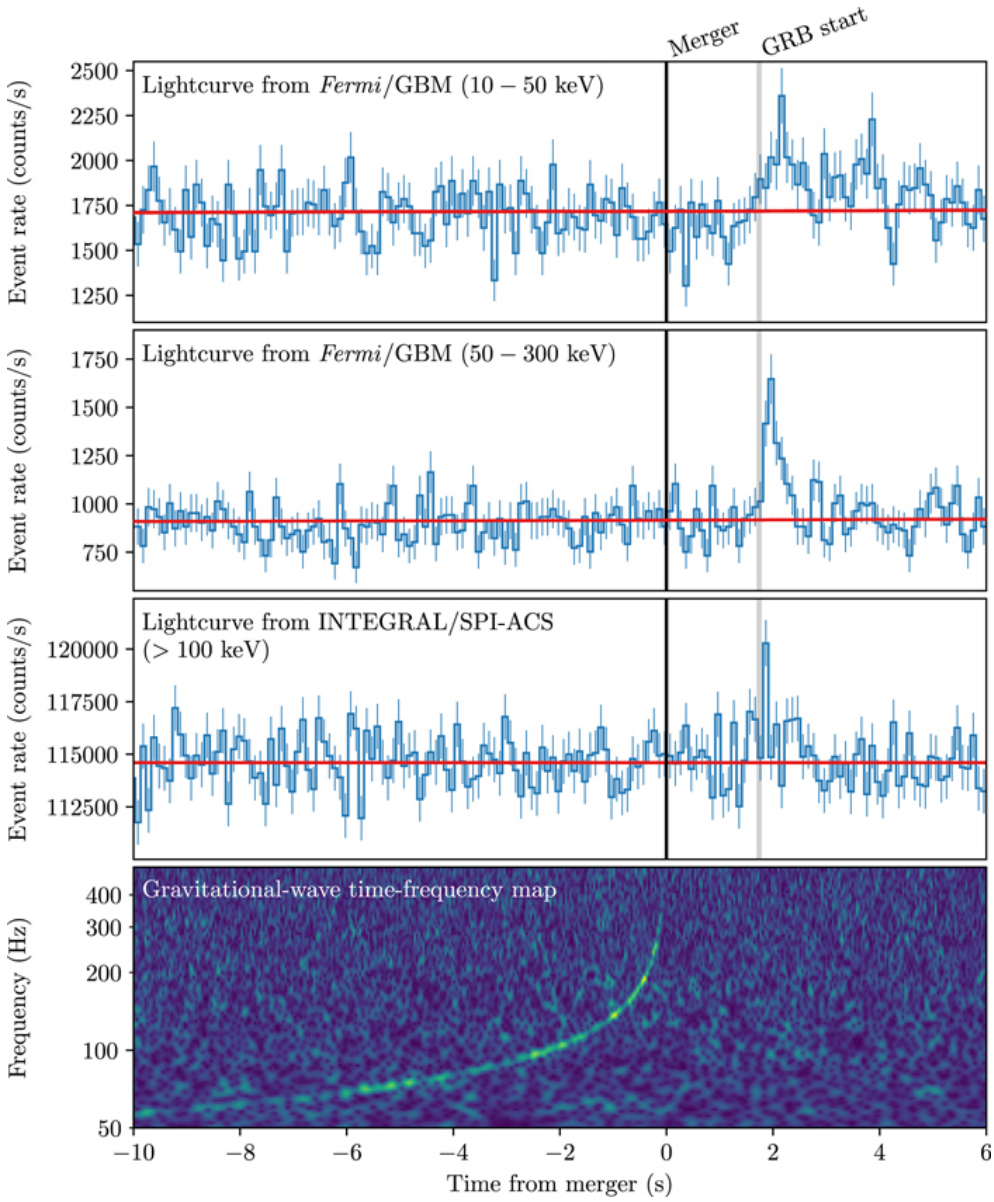

Figure 14: Joint, multi-messenger detection of GW170817 and GRB 170817A. Top: the summed GBM lightcurve for sodium iodide (NaI) detectors 1, 2, and 5 for GRB 170817A between 10 and 50 keV, matching the 100 ms time bins of the SPI-ACS data. The background estimate is overlaid in red. Second: the same as the top panel but in the 50–300 keV energy range. Third: the SPI-ACS lightcurve with the energy range starting approximately at 100 keV and with a high energy limit of least 80 MeV. Bottom: the time-frequency map of GW170817 was obtained by coherently combining LIGO-Hanford and LIGO-Livingston data. All times here are referenced to the GW170817 trigger time. From [5].

Another shared parameter between the afterglow and the GW is the luminosity distance. For this reason, GW are a useful tool also in cosmology, as the distance is estimated only through the fit of the waveform and through General Relativity, with no standard candles involved. This provides an independent estimation of the Hubble constant H_0, which can help in resolving the tension between the late and early time Universe estimation of H_0. The main problem of this method is the strong degeneracy that there is in the GW analysis between the inclination and the luminosity distance. In Chapter 4 we focus on this issue, showing that this degeneracy can be broken including the EM (afterglow) constraints on the viewing angle.

2

JOINING THE GRAVITATIONAL AND ELECTROMAGNETIC DOMAINS

Regarding probability, there are two main lines of thought: the bayesian and the frequentist approaches. Both have their own strengths and weaknesses, and they are often used in different circumstances to help determine the probability of events.

The basis of the bayesian approach is Bayes theorem, which describes the probability of an event occurrence based on previous knowledge of the conditions associated with this event. The parameter is taken as a random variable, meaning there is a probability that the event will occur. Frequentist inference, instead, assumes that events are based on frequencies, and the parameter is not a random variable but a fixed quantity. The predictions on the underlying truths of the experiment are made using only data from the current experiment.

Frequentist statistics estimates the desired confidence percentage (usually 95%) in which some parameter is placed. In contrast, Bayesian analysis answers the following question: "What is the probability of the hypothesis given the measured data?". In addition, frequentist statistics accepts or rejects the null hypotheses, but Bayesian statistics estimates the ratio of probabilities of two different hypotheses. This ratio is known as the Bayes factor [124]. The Bayes factor quantifies the support for one hypothesis over another, regardless of whether these hypotheses are correct.

The main difference between the two approaches is the prior, a concept that is not present in the frequentist approach. Bayesian approach encodes past knowledge of similar experiments into a statistical distribution, known as prior. This prior is combined with current experiment data to make a conclusion on the test. However, there is no well-defined method for choosing a prior. The consequence is that different people can use different priors for the same experiment and thus obtain different posteriors and make different conclusions (see the following Chapters).

Let us focus on the Bayesian approach, which is used throughout this thesis. All observed and unobserved parameters are given a probability distribution. The typical workflow consists of three main steps: modelling the available knowledge about a given parameter before data collection in a statistical distribution, called *prior distribution*; determining the *likelihood function* using the information about the parameter available in the observed data; combining the prior distribution and the likelihood function usign Bayes theorem in the form of the *posterior distribution*. The posterior $p(\vec{\theta}|d, M)$ of a set of parameters $\vec{\theta}$ for a given model M conditioned on some data $\vec{d}$ can be written into a form commonly known as Bayes theorem:

$$p(\vec{\theta}|\vec{d}, M) = \frac{\mathcal{L}(\vec{d}|\vec{\theta}, M)\pi(\vec{\theta}|M)}{\mathcal{Z}_{\vec{\theta}}}, \tag{24}$$

where $\mathcal{L}(\vec{d}|\vec{\theta}, M)$ is the likelihood of the data given the parameters of our model, $\pi(\vec{\theta}|M)$ is the prior for the parameters, and

$$\mathcal{Z}_{\vec{\theta}} = \int_{\Omega_{\vec{\theta}}} \mathcal{L}(\vec{d}|\vec{\theta}, M)\pi(\vec{\theta}, M)\,d\vec{\theta} \tag{25}$$

is the evidence (i.e. marginal likelihood) for the data given our model, where the integral is taken over the entire domain $\Omega_{\vec{\theta}}$ of $\vec{\theta}$ (i.e. over all possible parameter combinations). Throughout the rest of this thesis the subscript M will be dropped for the sake of simplicity, and because we are not comparing different models.

In this thesis, the posterior distributions are estimated using the PYTHON package DYNESTY [219], which is based on the Nested Sampling algorithm [215, 216].

2.0.1 *Joint fit of two datasets*

Suppose that we have two independent datasets $\vec{d}_1$ and $\vec{d}_2$ described by the model M. The set of parameters $\vec{\theta}$ for M is given by parameters exclusive to $\vec{d}_1$, parameters exclusive to $\vec{d}_2$ and a shared parameter between the two datasets: $\vec{\vartheta} = \{\vec{\theta}_1, \vec{\theta}_2, \theta_0\}$. The fit of the two datasets will have a joint likelihood given by the product of the two likelihoods associated to each dataset

$$\mathcal{L}_{1,2}(\vec{d}_1, \vec{d}_2|\vec{\theta}, M) = \mathcal{L}_1(\vec{d}_1|\vec{\theta}, M) \times \mathcal{L}_2(\vec{d}_2|\vec{\theta}, M), \tag{26}$$

here, for notation simplicity, we will drop M, so

$$\mathcal{L}_{1,2}(\vec{d}_1, \vec{d}_2|\vec{\theta}) = \mathcal{L}_1(\vec{d}_1|\vec{\theta}) \times \mathcal{L}_2(\vec{d}_2|\vec{\theta}), \tag{27}$$

The posterior distribution will be proportional to

$$p(\vec{\theta}|\vec{d}_1, \vec{d}_2) \propto \mathcal{L}_{1,2}(\vec{d}_1, \vec{d}_2|\vec{\theta})\pi(\vec{\theta}) \tag{28}$$

where we omit the evidence, which can be treated as a normalization factor. If we marginalize for all the parameters except the shared one, θ_0, we get

$$p(\theta_0|\vec{d}_1, \vec{d}_2) \propto \mathcal{L}_{1,2}(\vec{d}_1, \vec{d}_2|\theta_0)\pi(\theta_0), \tag{29}$$

where we assume that the prior is separable between the shared parameter, the ones describing only $\vec{d}_1$ and only $\vec{d}_2$: $\pi(\vec{\theta}) = \pi(\theta_0, \vec{\theta_1}, \vec{\theta_2}) = \pi(\theta_0)\pi(\vec{\theta_1})\pi(\vec{\theta_2})$.

Another possibility is to fit one dataset, for example $\vec{d}_1$, and use the resulting marginalized posterior probability of the shared parameter θ_0 as prior in the fit of the other dataset, $\vec{d}_2$. This is the case of the EM fit with a GW-informed prior. From the fit of the first dataset $\vec{d}_1$ we get a marginalized posterior distribution

$$p(\theta_0|\vec{d}_1) \propto \mathcal{L}_1(\vec{d}_1|\theta_0)\pi(\theta_0). \tag{30}$$

where we assume that the prior on the shared parameter is the same as Eq. (29). For the fit of $\vec{d}_2$ we use Eq.(30) as prior on θ_0. The posterior distribution resulting from the fit of $\vec{d}_2$ will be

$$p(\theta_0|\vec{d}_2) \propto \mathcal{L}_2(\vec{d}_2|\theta_0)\pi_2(\theta_0), \tag{31}$$

which, since $\pi_2(\theta_0) = p(\theta_0|\vec{d}_1)$, becomes

$$p(\theta_0|\vec{d}_2) \propto \mathcal{L}_2(\vec{d}_2|\theta_0)\mathcal{L}_1(\vec{d}_1|\theta_0)\pi(\theta_0), \tag{32}$$

This posterior is the same as the one found with a simultaneous fit, Eq.(29). So we can say that when there is one parameter in common, independently on the likelihood function, fitting the two datasets jointly or using the posterior distribution of the shared parameter as prior on that same parameter is equivalent.

In the case of two (or more) shared parameters between two different datasets, the joint fit will give a posterior distribution written in the same way as Eq.(28), where the likelihood will be given by Eq.(27). Making explicit the shared parameters, which we will call $\vec{\theta_s} = \{\theta_a, \theta_b\}$, and marginalizing for $\vec{\theta_1}$ and $\vec{\theta_2}$, we get

$$\mathcal{L}_{1,2}(\vec{d}_1, \vec{d}_2|\vec{\theta_s}) = \mathcal{L}_1(\vec{d}_1|\vec{\theta_s}) \times \mathcal{L}_2(\vec{d}_2|\vec{\theta_s}), \tag{33}$$

and the posterior will be

$$p(\vec{\theta_s}|\vec{d}_1, \vec{d}_2) \propto \mathcal{L}_{1,2}(\vec{d}_1, \vec{d}_2|\vec{\theta_s})\pi(\vec{\theta_s}). \tag{34}$$

In the case of the two separate fits, the posterior distribution for the two shared parameters from the fit of $\vec{d}_1$ will be

$$p(\vec{\theta_s}|\vec{d}_1) \propto \mathcal{L}_1(\vec{d}_1|\vec{\theta_s})\pi(\vec{\theta_s}) \tag{35}$$

The posterior of the fit $\vec{d}_2$ with the prior distribution as in Eq.(35) will be

$$p(\vec{\theta_s}|\vec{d}_2) \propto \mathcal{L}_2(\vec{d}_2|\vec{\theta_s})\pi_2(\vec{\theta_s}) \tag{36}$$

replacing $\pi_2(\vec{\theta_s})$ with its marginalized posterior distributions from the fit of dataset $\vec{d}_1$ we get

$$p(\vec{\theta_s}|\vec{d}_2) \propto \mathcal{L}_2(\vec{d}_2|\vec{\theta_s})\mathcal{L}_1(\vec{d}_1|\vec{\theta_s})\pi(\vec{\theta_s}) \tag{37}$$

which is still identical to the joint posterior in Eq.(34). However, in this case, we cannot assume the prior is separable between the individual shared parameters:

$$\pi(\vec{\theta_s}) = \pi(\theta_a, \theta_b) \neq \pi(\theta_a)\pi(\theta_b), \tag{38}$$

because this requires the parameters to be independent, which is no longer the case after they have been fit to the first dataset. The new prior

$$\pi(\vec{\theta_s}) = \int d\vec{\theta}_1 p(\vec{\theta_s}, \vec{\theta}_1|\vec{d}_2) \tag{39}$$

is the posterior from the fit of $\vec{d}_1$ marginalized over only the parameters exclusive to $\vec{d}_1$. This will, in general, be multidimensional and contain all the covariances between the parameters in $\vec{\theta_s}$.

2.1 NESTED SAMPLING ALGORITHM

Nested sampling is a method for estimating the Bayesian evidence first developed by John Skilling [215]. The basic idea is to approximate the evidence by integrating the prior in nested "shells" of constant likelihood. Unlike Markov Chain Monte Carlo (MCMC) methods, Nested Sampling simultaneously estimates both the evidence and the posterior. It allows samples to be allocated adaptively during the course of a run to better sample areas of parameter space to maximize a chosen

objective function. This allows a particular Nested Sampling algorithm to adapt to the shape of the posterior in real time, improving both accuracy and efficiency.

Let us assume a continuous prior so that, for example, $V = \int \pi(\vec{\theta}) d\vec{\theta}$ can easily be associated with a volume. Lets consider that we want to compute the evidence over a d-dimensional continuous parameter space. The first step is to sample randomly from the prior N live points and evaluate the likelihood function at each point, as shown in Fig.15. The live point with the lowest likelihood L_1 (the worst fit, red cross in the Figure) is removed and becomes the first dead point. This reduces the volume by a factor of approximately $\delta V = 1/N$, since each point represents $1/N$ of the total volume. A new, independent live point is sampled randomly from the prior (blue dot in the Figure), but it is required that its likelihood exceeds the likelihood of the previous discarded point L_1. Any region with likelihoods below L_1 is not considered any further, and we have again N live points within a volume. We repeat these steps, which continuously increases the likelihood threshold and shrinks the volume, up to a stopping criterion. The progression by constant shrinkage factors reduces the remaining volume exponentially. After i iterations the remaining volume is exponentially small, $V_i = (1 - 1/N)^i$, with a high likelihood threshold selecting live points close to the best-fit parameter peak(s), i.e., the likelihood of the remaining points is flat (see bottom panel of Fig.15). Further contributions to $\mathcal{Z}$ are thus negligible and the integration can be stopped. The algorithm has converged, in the sense that iterating further would not significantly alter the result.

Removing a point at iteration i reduced the volume $V_i = (1 - 1/N)^i$ by $\Delta V_i = V_i - V_{i-1} = (1 - 1/N)^i \times 1/N$. This can be envisioned as a shell of prior volume being peeled off. Accordingly, each dead point is assigned the unnormalised weight $\Delta V_i \times L_i$, and the integral $\mathcal{Z}$ is simply: $\mathcal{Z} \sim \sum_i \Delta V_i \times L_i$, with an error estimate available. The weighted dead points are approximate samples from the posterior and the remaining live points at termination can also be included, with their likelihoods multiplied by the remaining volume distributed equally among them, V_i/N.

2.1.1 *Theoretical explanation*

Nested Sampling, unlike MCMC methods which attempt to estimate directly the posterior, attempts to estimate the evidence $\mathcal{Z}$

$$\mathcal{Z} = \int_{\Omega_{\vec{\theta}}} p(\vec{\theta}) d\vec{\theta} \tag{40}$$

As this integral is over the entire multi-dimensional domain of $\vec{\theta}$, it is usually very challenging to estimate.

Nested Sampling approaches this problem by refactoring this integral into one over the prior volume X of the enclosed parameter space

$$\mathcal{Z} = \int_0^1 \mathcal{L}(X) dX \tag{41}$$

where $\mathcal{L}(X)$ defines an iso-likelihood contour defining the edge of the volume X, while the prior volume

$$X(\lambda) = \int_{\Omega_{\vec{\theta}}: \mathcal{L}(\vec{\theta}) \geqslant \lambda} \pi(\vec{\theta}) d\vec{\theta} \tag{42}$$

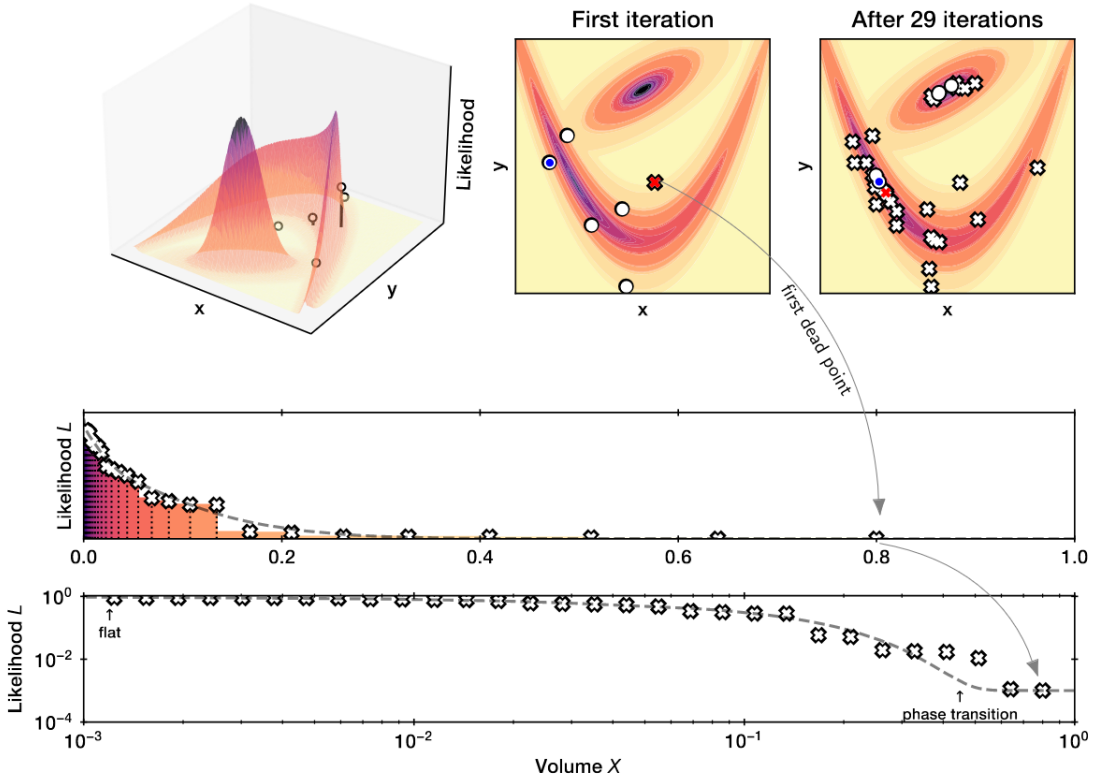

Figure 15: Top left: A complicated likelihood function is defined over a two-dimensional parameter space. Nested sampling begins by evaluating N = 5 random points. Top center: Each live point (circle) defines a likelihood contour. The lowest likelihood point (red cross) becomes a dead point. It is replaced by a new, live point (blue circle), sampled randomly from the prior but above the contour defined by the dead point. Top right: After a few iterations, the live points concentrate in a small volume at the likelihood peak. Bottom panels (top is linear, bottom is logarithmic): For each iteration, a dead point is placed with its likelihood and the prior volume estimated by geometric shrinkage. The prior volume of the sequence shrinks exponentially from right to left. Vertical bars represent the likelihood shell removed, and are coloured consistent with the contours shown in the other panels. The bar area is the posterior weight, and the sum of the bars gives the marginal likelihood Z. In the bottom log-log plot, the phase transition is marked, which corresponds to the transition from the wide, shallow yellow regions to the high and steep orange regions in the upper panels. From [41].

is the fraction of the (multi-dimensional) prior function where the likelihood is above the threshold λ, $\mathcal{L}(\vec{\theta}) \geqslant \lambda$. Since the prior is normalized, this gives $X(\lambda = 0) = 1$ and $X(\lambda = \inf) = 0$, which define the bounds of integration for equation (41) [219].

2.1.2 *Numerical procedure*

The nested sampling procedure (drawing N live points from the prior and at each iteration, remove the live point with the lowest likelihood, replacing it with a new one sampled from the prior subject to a likelihood constraint) allows us to estimate the prior volume of the previous live point (a dead point) as:

$$\ln X \approx -\frac{i \pm \sqrt{i}}{N}. \tag{43}$$

Once the sampling terminates, the remaining set of live points are distributed uniformly within the final prior volume and added to the list of samples.

The evidence integral, eq.(41), can be numerically approximated using a set of N dead points via

$$\mathcal{Z} = \sum_{1}^{N} f(\mathcal{L}_i) f(\Delta X_i) \equiv \sum_{1}^{N} w_i \tag{44}$$

where w_i is each point's estimated weight. For example, for a simple linear integration scheme using rectangles, we can take $f(\mathcal{L}_i) = \mathcal{L}_i$ and $f(\Delta X_i) = X_{i-1} - X_i$.

We can subsequently estimate posteriors from the same N dead points by assigning each sample its associated importance weight

$$p(\vec{\theta}) = p(X_i) \equiv p_i = \frac{w_i}{\sum_{i=1}^{N} = \frac{w_i}{\mathcal{Z}}} \tag{45}$$

The sampling can stop when the majority of the parameter space has been explored, meaning that our set of dead points gives us an integral that encompasses the vast majority of the posterior. Therefore, the stopping criterion is

$$\Delta \ln \mathcal{Z}_i \equiv \ln(\mathcal{Z}_i + \Delta\mathcal{Z}_i) - \ln(\mathcal{Z}_i) < \epsilon \tag{46}$$

where $\Delta\mathcal{Z}_i$ is the estimated remaining evidence we have yet to integrate over and ϵ determines the tolerance, which is usually fixed at 0.01 [41, 219]. The remaining evidence is unknown, but we can give it an upper bound of $\mathcal{L}_i^{max} X_i$, where $\mathcal{L}_i^{max}$ is the maximum likelihood across the entire domain $\Omega_{\vec{\theta}}$ and X_i is the prior volume at the current iteration. This is equivalent to treating the remaining likelihood included in the current sample as a flat function with value $\mathcal{L}_i^{max}$. Both these parameters are not known exactly, but they can be approximated as maximum value of the likelihood among the live points at iteration i and the estimated (remaining) prior volume respectively. Usually this approximation works well, but there could be cases where the sampling termites early, this can happen if there is an extremely narrow likelihood peak within the remaining prior volume that has not yet been discovered by the live points.

2.1.3 *Dynamic nested samping*

In the nested sampling algorithm the number of live points remains constant throughout an entire run. Instead, in the dynamic nested sampling [219] the live points are allocated dynamically such that at a given iteration i we can have a variable number N_i of effective live points. Since the change in prior volume at a given iteration goes as $1/N_i$, allowing to vary gives us the ability to control the effective resolution as a function of prior volume. This means we could sample preferentially in and/or near the bulk of the posterior mass.

2.1.4 *Nested samping and MCMC chains*

Nested sampling and Monte Carlo Markov Chains (MCMC) are two different tools, each with its own features, and one is not better than the other. One of the useful features of nested sampling is that, as we already pointed out at the beginning of the Chapter, it can estimate both the evidence and the posterior, while MCMC methods estimate only the latter. Moreover, generally nested sampling can better sample multi-modal distributions, with respect to many MCMC methods. The nested sampling stopping criteria are solid and based on the evidence estimation, while the MCMC ones seem arbitrary, based on the sample sizes. In the MCMC methods, unlike nested sampling, the preliminary steps, during which the chain moves from its unrepresentative initial value to the modal region of the posterior, the "burn-in" phase, are usually discarded.

However, because most Nested Sampling implementations rely on sampling from uniform distributions, applying them to general distributions requires knowing the appropriate prior transform T (see Section 2.3). While these are straightforward to define when the prior can be decomposed into separable, independent components, they can be more difficult to derive when the prior involves conditional and/or jointly distributed parameters. Also, because in nested sampling the evidence depends on the amount of prior volume that needs to be integrated over, the overall expected runtime is sensitive to the relative size of the prior.

2.2 LIKELIHOOD FUNCTION

The likelihood function $\mathcal{L}(\vec{d}|\vec{\theta}, M)$ describe a hypersurface whose peak represents the combination of model parameter values that maximize the probability of drawing the sample obtained.

The procedure for obtaining the maximum likelihood is, for computational convenience, done using the natural logarithm of the likelihood. Let θ be a parameter (unknown value), let $\vec{d} = x_1, ..., x_n$ be a set of data, independent and identically distributed. What is the most likely value that θ could be, given the data that we have observed? The higher the likelihood, the more likely that parameter is.

The likelihood function can be written as the joint probability density function (PDF) of our random sample

$$\mathcal{L}(x_1, ..., x_n|\vec{\theta}, M) = f(x_1, ..., x_n|\theta) = f(x_1|\theta)...f(x_n|\theta) = \prod_{i=1}^{n} f(x_i|\theta) \tag{47}$$

To find the value of θ which maximize the likelihood, or the logarithm of the likelihood, the derivative is done, but the shape of the data PDF must be known. Usually we assume that the data have a normal distribution with a standard deviation σ_i, while μ is the mean value predicted by the model, so the PDF of one data point will be

$$f(x_i|\theta) = \frac{1}{\sqrt{2\pi\sigma_i^2}} \exp\left[\frac{-(x_i - \mu(\theta))^2}{2\sigma_i^2}\right] \tag{48}$$

and the total PDF will be

$$f(x_i, ..., x_n|\theta) = \prod_{i=1}^{n} f(x_i|\theta) = \frac{1}{(\sqrt{2\pi\sigma_i^2})^n} \exp\left[\frac{-(x_i - \mu(\theta))^2}{2\sigma_i^2}\right] =$$

$$= \frac{1}{(2\pi\sigma_i^2)^{n/2}} \exp\left[\left(\sum_{i=1}^{n} -(x_i - \mu(\theta))^2\right)/2\sigma_i^2\right] \tag{49}$$

Taking the natural logarithm we have

$$l(x_1, ..., x_n|\theta) = \sum_{i=1}^{n} \frac{-(x_i - \mu(\theta))^2}{2\sigma_i^2} - \frac{n}{2}\log(2\pi\sigma_i^2). \tag{50}$$

From here, the first and second derivatives can be done in order to find the maximum of l and the best values for the parameters θ. It is to be noted that maximize l corresponds to minimize the first part of eq.(50), this method is the sum of the square residuals, namely the minimization of the χ^2 in the frequentist approach.

2.2.1 *Likelihood with non-detections*

If in the dataset non detections (upper limits) are present, then the likelihood shape will change, this is because they give just a threshold under which the detection could be present. The PDF in this case can be written as in eq.(48), replacing detections with upper limits [65, 207]

$$f(x_j|\theta) = \frac{1}{\sqrt{2\pi\sigma^2}} \int_{-\inf}^{x_j} \exp\left[\frac{-(x - \mu(\theta))^2}{2\sigma^2}\right] dx \tag{51}$$

where x_j is the $1-\sigma$ upper limit of the observation. The logarithm of the likelihood of detections and non detections can be written as

$$l_i + l_j = \sum_{i=1}^{n} \frac{-(x_i - \mu(\theta))^2}{2\sigma_i^2} - \frac{n}{2}\log(2\pi\sigma_i^2) + \sum_j \log \frac{1}{\sqrt{2\pi\sigma_j^2}} \int_{-\inf}^{x_j} \exp\left[\frac{-(x - \mu(\theta))^2}{2\sigma_j^2}\right] dx \tag{52}$$

For computational convenience the integral can be recast in terms of the error function

$$erf(x) = \frac{2}{\sqrt{\pi}} \int_0^x e^{-t^2} dt \tag{53}$$

so that

$$l_i + l_j = \sum_{i=1}^{n} \frac{-(x_i - \mu(\theta))^2}{2\sigma_i^2} - \frac{n}{2}\log(2\pi\sigma_i^2) + \sum_j \log\left[\frac{1}{2}\left(1 + erf(\frac{x_j - \mu(\theta)}{\sqrt{2}\sigma_j})\right)\right] \tag{54}$$

The last equation reduces to eq.(50) when there are no upper limits in the dataset.

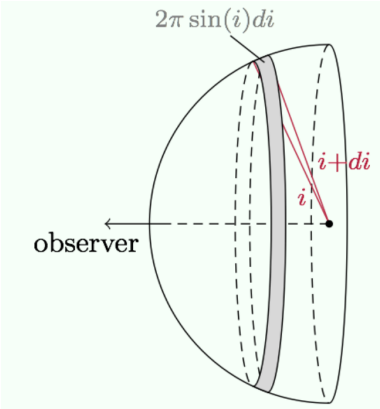

Figure 16: Sketch that explains the prior choice on the viewing angle. In the figure $i = \theta_v$.

2.3 PRIOR PROBABILITIES

The prior distribution models the a priori knowledge that we have on a parameter. The latter can be an informative distribution, like the Normal, but also a uniform or isotropic one in a certain range.

For example, in the case of the analysis of a NS merger, both in the GW and in the GRB afterglow modeling, the viewing angle is a fit parameter. We do not have a very restrictive a prior knowledge about it, except for the fact that small viewing angles are harder to detect, with respect to larger values. This can be modelled using a sine prior function. If a vector is equally likely to be oriented toward any part of the sphere, the relative likelihood that it falls within some small range $d\theta_v$ of a specific inclination angle θ_v is proportional to the area on the unit sphere covered by that range of angles ($2\pi \sin(\theta_v) d\theta_v$, see Fig. 16):

$$f(\theta_v) \propto \begin{cases} 0 & \theta_v < 0 \\ \sin(\theta_v) & 0 \leqslant \theta_v \leqslant \pi/2 \\ 0 & \theta_v > \pi/2 \end{cases} \tag{55}$$

This probability density function (PDF) has to be normalized so that $\int_{-\inf}^{+\inf} f(\theta_v) d\theta_v = 1$. Sometimes, a uniform distribution is preferred for the viewing angle, so, without loosing the above knowledge, a uniform in $\cos(\theta_v)$ prior distribution is used. This directly comes from eq.(55), through a change of variable

$$f(\theta_v) d\theta_v = f(\theta_v(y)) |\frac{d\theta_v}{dy}| dy = g(y) dy, \tag{56}$$

where y is the new variable and $g(y)$ is the new PDF. We want $g(y)$ to be uniform (flat), so we can use $|d\theta_v/dy| \propto 1/f(\theta_v(y))$. The variable change $y = \cos(\theta_v)$, or $\theta_v = \arccos(y)$, satisfies the above equation and gives a constant $g(y)$:

$$g(\theta_v) \propto \begin{cases} 0 & \cos(\theta_v) < 0 \\ 1 & 0 \leqslant \cos(\theta_v) \leqslant 1 \\ 0 & \cos(\theta_v) > 1 \end{cases} \tag{57}$$

2.3.1 *Nested sampling prior transform function*

In Nested Sampling, the samples are generated from the prior function π subject to a likelihood constraint λ (Section 2.1.1): at a given iteration i, the samples $\vec{\theta}_{i+1}$ from the prior $\pi(\vec{\theta})$ are generated until $\mathcal{L}(\vec{\theta}_{i+1}) \geqslant \mathcal{L}(\vec{\theta}_i)$.

Sampling from an arbitrary prior distribution in some cases is difficult, since the density can vary drastically from place to place. For this reason, in nested sampling the prior is chosen as standard uniform (i.e. flat from 0 to 1) in all dimensions. In this way the density interior to λ is constant and X behaves more like a typical volume V. In order to transform a general prior function to a standard uniform one we can use the appropriate "prior transform" function T, which maps a set of parameters with a uniform prior over the d-dimensional unit cube to the parameters of interest. For independent parameters, this would be the inverse cumulative distribution function (CDF) associated with each parameter.

3

FROM ASTROPHYSICS

Following the detection of GW170817, several multi-messenger studies combined GW and EM data. This integration enhances our comprehension of the physics behind binary neutron star merger events and helps overcome degeneracies encountered when analyzing EM and GW data independently.

Many of these studies pertains to the neutron star equation of state. Bayesian methods are implemented to combine GW170817 and the associated kilonova AT2017gfo, in order to provide improved estimates of source parameters such as the mass ratio and the neutron star tidal deformability [e.g., 40, 47, 55, 56, 62, 114, 160, 181, 182, 184, 185]. This is accomplished by leveraging the fact that, across a broad spectrum of neutron star equation of state models, the dynamical ejecta mass is predominantly determined by the spin and mass ratio of the two neutron stars [e.g., 120, 211], which can be constrained along with the neutron star tidal deformability with GW data from the inspiral stage of neutron star mergers [e.g., 186], while kilonova emission models in the EM domain place constraints on the ejecta mass [e.g., 31, 123, 233].

Other studies, like the one presented in this Chapter, focuses on the system geometry, which includes the viewing angle and the angular structure of the jet. There have been numerous attempts to estimate the system geometry of GW170817 based on model fitting of the EM afterglow light curve, since the early discovery papers of the afterglow in the X-ray and radio bands [109, 227, and references therein]. The viewing angles and jet opening angles found in different studies are often inconsistent with each other, see a compilation of some of the most recent results in Fig.17.

In order to study the geometry, energetics and microphysics of the jet, an assumption on the jet type has to be made. In the case of GW170817, a jet Gaussian structure is often assumed. In this case, the rising light curve phase can only constrain the ratio between viewing angle and jet opening angle [197]. This leads to an intrinsic degeneracy between these parameters: a proper scaling of the two leads to the same light curve, with some slight changes in the decreasing slope. Breaking this degeneracy requires further information (see also [158] for additional discussion).

One way of improving the precision of the viewing angle measurement is to break the viewing angle–jet opening angle degeneracy. An interesting option is to join information from GW and EM counterparts, either by jointly fitting the two datasets or by including GW information in the EM analysis as a constraint on the common parameters, either a priori or a posteriori. Wang and Giannios [236] use a Bayesian approach to fit the observed GW170817 afterglow emission with a simulated jet profile that predicts the afterglow light curve. They impose a GW-informed prior on the luminosity distance and the observing angle. The latter can be tightly constrained and the distance uncertainty is in turn also greatly

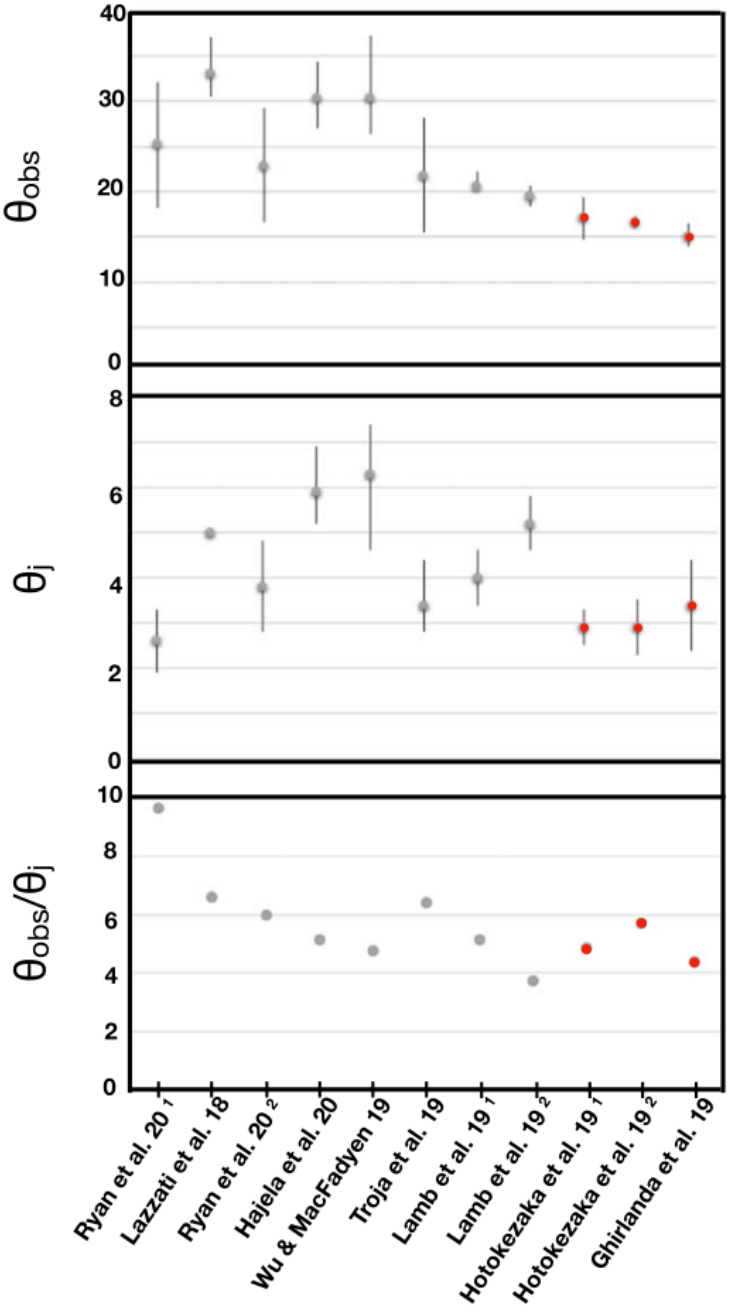

Figure 17: Results of recent modeling of the geometry of GW170817. Top: viewing angles. Middle: jet opening angles. Bottom: their ratios. Error bars are from the original papers. Error bars are not shown on the ratio θ_{obs}/θ_j as the quoted errors in the original papers are most likely correlated. While values for θ_{obs} or θ_j vary strongly, the scatter in θ_{obs}/θ_j is small with almost all values are around 5-6. The last three models (marked in red [93, 121]) use the VLBI information. Some papers give two values and those are marked by superscripts. Figure and description from [158].

reduced. This results in a tight constraint on the observing angle $\theta_v = 22 \pm 1$ deg. Troja et al. [223, 224] and Troja et al. [225, 226] study the broadband afterglow of GW170817 with a Bayesian fit, imposing a GW-informed prior [3] on the viewing angle and fixing the luminosity distance. The viewing angle goes from almost 20 deg (2018) to almost 30 deg (2021), because of the relative excess of the late-time X-ray observations. Guidorzi et al. [105] use a Bayesian analysis and reanalyze the LIGO-Virgo posteriors incorporating the viewing angle constraints obtained from the X-ray and radio afterglow modeling, finding an off-axis angle of 25–50 deg.

In my thesis work, I introduce a novel approach by simultaneously fitting, through Bayesian analysis, both GW and EM data for the GW170817 event. This method incorporates gravitational waveforms from binary coalescences for the GW signal [18, 217], and structured jet models [197] for the EM data. In particular, in this Chapter we assume a Gaussian structure, the analysis is then complemented with the power law structure in the next Chapter. Within this Chapter, I demonstrate the application of the simultaneous fit approach to the GW170817 dataset and the EM data obtained from its afterglow counterpart. I compare the outcomes with those obtained through the conventional practice of employing disjoint priors in the two domains. The central focus is on the system's geometry, particularly addressing the degeneracy issue between the viewing angle and the opening angle of the jet. The objective is to compare the EM fit with a GW-informed prior and an EM+GW fit. Additionally, I highlight that the methodologies implemented in this study yield improvements over traditional disjoint analyses.

In Section 3.3 the results are presented, discussing future perspectives for O4, the upcoming GW observing run, in Section 3.4. In Section 3.5 I provide a concluding summary. Throughout this Chapter, the redshift value is fixed to $z = 0.0098$ and the luminosity distance is set to $d_L = 41$ Mpc [3]. For the purpose of assessing H_0, instead, the luminosity distance is left as free parameter, see the next Chapter.

I note that, within the framework of the same messenger, another option to break the viewing angle–jet opening angle degeneracy is to join the GW170817 afterglow light curve with independent measurements, such as the observations that measure the superluminal motion of the centroid in radio and optical images [93, 154, 155], or the late time observations of the light curve transition to the sub-relativistic phase [197]. We will also explore this in the following Chapter.

In general, the best approach to study an event is, indeed, to include all the available information about that event, so, in case of GW170817, the GW, the afterglow light curve, the jet centroid motion and the kilonova. However, even analyses including only some of these are useful, especially to quantify possible systematics, that will count as reference for future events. In the case of GW170817, the afterglow light curve and the centroid motion tend to give contrasting results, as it will be shown in this thesis, mainly because of the late time data points in the light curve, which seem to be showing a flux excess. Therefore, the use of the complete available information is even more important.

3.1 MODELLING OF GW AND EM SIGNALS

This section details the models and data used for this Chapter. The luminosity distance is fixed in the EM fits to analyse the data in the EM standard fashion. For consistency, the cosmology for the GW fits is fixed too: this allows to safely

compare results from EM and GW fits, as well as from a simultaneous fit of the EM and GW data.

3.1.1 *The afterglow light curve*

For GW170817, the afterglow light curve deviates notably from the conventional on-axis uniform "top-hat" jet often used in the analysis of GRB afterglows due to a combination of a moderate viewing angle and angular structure in the jet. Nonetheless, the use of this model is justified when the observer is on axis, as the lateral structure of the jet has minimal influence on the emission in such instances [197], see also Section 1.2.2.

The slow rising and then (after the peak time) declining afterglow light curve of GRB 170817A are indeed consistent with emission from a structured jet. The light curve is modelled using AFTERGLOWPY [197]. This PYTHON package can compute the observer frame flux of synchrotron radiation from the forward shock of the relativistic blast wave in a constant density medium. It uses semi-analytic approximations of the jet dynamical evolution and synchrotron emission, taking into account jet spreading and jet angular structure. In the latest version [198], it includes also the modelling of the non-relativistic late-time phase. It does not include synchrotron self-absorption, which, in the case of GW170817, does not influence the spectrum.

In this Chapter, a Gaussian structure is assumed for the jet, see eq.(6). E_0, θ_c and θ_w are treated as free parameters and they represent the on-axis isotropic equivalent kinetic energy of the blast wave, the jet opening angle and the jet total angular width, respectively. We assume that the electrons are shock-accelerated and emit synchrotron radiation, their energy distribution is a power law with slope $-p$, the fraction of their post-shock internal energy is ϵ_e, while the fraction of post-shock internal energy in the magnetic field is denoted by ϵ_B (see also Section 1.2.3). Furthermore, the circumburst medium number density n_0 and the viewing angle θ_v, between the jet axis and the line of sight, are free parameters as well. This yields a total of 8 free parameters, given that the luminosity distance and the redshift are fixed. The fraction of accelerated electrons (also called participation fraction) χ_N is fixed to 1.0 as well.

The prior probability distributions are uniform for θ_w in [0, 90] deg, θ_c in [0, 90] deg, and p in [2, 3]; log-uniform for E_0 in $[10^{49}, 10^{56}]$, ϵ_e in $[10^{-5}, 10^{0}]$, ϵ_B in $[10^{-5}, 10^{0}]$, and n_0 in $[10^{-7}, 10^{2}]$, see also Table 5. These ranges reflect the population of short GRB properties [71, 81]. We use two prior distributions for the viewing angle θ_v: an isotropic one, which has a sinusoidal shape from 0 to 90 deg, and a GW-informed one, which is the posterior distribution retrieved from fitting the GW data alone (see Section 3.1.2).

3.1.2 *Gravitational-waves*

I use the Bayesian inference library for GW astronomy BILBY [18, 217] and the dynamic nested sampling package DYNESTY [219] to process the GW data. To model GWs from binary neutron star mergers, the `IMRPhenomPv2_NRTidal` waveform model [61, 63, 64, 110] is chosen. The parameters used by this model are the two component masses m_1 and m_2, for which the common convention $m_1 \geqslant m_2$ is

followed, the components of the dimensionless spin angular momenta of the two neutron stars, $\mathbf{a}_1$ and $\mathbf{a}_2$, which constitute six additional parameters, and the tidal deformability parameter of each star, Λ_1 and Λ_2, for a total of 10 parameters. The tidal deformability parameter Λ quantifies how an extended object responds to the $\ell = 2$ component of an external tidal field; it is related to the mass m and radius R of the object by $\Lambda = (2/3)k_2[(c^2/G)(R/m)]^5$, where k_2 is the dimensionless $\ell = 2$ Love number [e.g., 235, 249].

In addition to the gravitational waveform physical parameters listed above, known as intrinsic parameters as they shape the *emitted* waveform, the *observed* GW signal is determined also by seven extrinsic parameters. These are the right ascension and declination of the source (i.e., its sky position), the luminosity distance of the source, the inclination angle θ_{JN} between the total angular momentum $\mathbf{J}$ of the binary and the line of sight $\mathbf{N}$ from the source to the observer (i.e., $\cos\theta_{JN} = \hat{J} \cdot \hat{N}$), the polarization angle, and the phase and time of coalescence. The total number of parameters is therefore 17.

In this work, the sky-position of the source is fixed to the one of AT 2017gfo [6] both when processing GW170817 and when considering future GW170817-like events. Similarly, the luminosity distance is assumed to be known. In the case of GW170817, we set this to 41 Mpc, while for the simulated future events we set it to 136.5 Mpc, which corresponds to a reduction of the afterglow flux of about one order of magnitude, and to 70 Mpc, which corresponds to a reduction of a factor 3. Finally, there is a marginalization over the phase of coalescences, thus reducing the number of free GW parameters to 13. The priors for the intrinsic and extrinsic GW parameters are uniform for the chirp mass $\mathcal{M}$ in [1.18, 1.21], the mass ratio q in [0.125, 1], the dimensionless spin magnitudes a_1 and a_2 in [0, 0.05], the opening angle of the cone of precession about the system angular momentum ϕ_{JL} and the azimuthal angle separating the spin vectors $\phi_{1,2}$ in [0, 360] deg with periodic boundary, the tidal deformability parameter Λ_1 and Λ_2 in [0, 5000]; sinusoidal for the tilt angles between the spins and the orbital angular momentum θ_1, θ_2 in [0, 180] deg [194], see also Table 5.

3.2 GW170817 DATA SET

I use the afterglow X-ray emission of GW170817 from *Chandra* and *XMM*, already introduced in Troja et al. [225], and represented in Fig. 18 with red circles. The most recent Chandra data point at 1734 days from the merger is also included in the analysis [166]. For the optical light curve, the works of reference are Troja et al. [227] and Fong et al. [82], see the orange diamonds in Fig. 18. Finally, for the radio dataset I refer to Makhathini et al. [141]; in Fig. 18 only the VLA detections at 3 GHz are shown for the sake of good order, but included in the fit are all frequencies from 0.7 to 15 GHz for VLA, ATCA, uGMRT, eMERLIN, MeerKAT.

In all bands, the flux densities are used in the analysis, including X-rays. However, an additional information is provided at each time: the spectral shape. In the case of GW170817, the synchrotron spectrum is, at all times, in the slow cooling phase, as already mentioned in Section 1.2.5, but, in general, it could change during the emission and, in that case, the flux integrated over the observing band should be preferred in the analysis.

The GW data of GW170817 are publicly available at the GW Open Science Center[1][11]. In this work, the cleaned version of the strain data, where the glitch discussed in Abbott et al. [4] has been removed, are used.

3.2.1 *Joint gravitational-wave and afterglow data analysis*

In the joint analysis there is a total of 21 parameters. However, given that the GRB jet develops around **J**, the inclination angle θ_{JN} and the viewing angle θ_v are essentially the same quantity, and thus a common parameter of the GW and EM domains. When **J** points towards the observer, $\theta_{JN} < 90$ deg and $\theta_v = \theta_{JN}$, while when **J** points away from the observer, $\theta_{JN} > 90$ deg and $\theta_v = 180 - \theta_{JN}$ deg. In summary,

$$\theta_v = 90\mathrm{deg} - |\theta_{JN} - 90\mathrm{deg}| \,. \tag{58}$$

In order to fit and analyse the EM and GW data, I use bayesian statistic, the complete method is already introduced in Chapter 2. The EM and GW likelihoods are both Normal distributions. The GW likelihood function is defined in, e.g., Finn [75], Romano and Cornish [193], and Romero-Shaw et al. [194]; in this likelihood, both the data and the model are expressed in the frequency domain. The EM likelihood function is proportional to $\mathcal{L}_{EM}(d_{EM}|\vec{\vartheta}) \propto \exp(-\chi^2/2)$, where χ^2 is evaluated from comparing the flux estimated from the model with a set of parameters $\vec{\vartheta}$ with the entire broadband set of data d_{EM}.

In this work, I fit both the EM data using a GW-informed prior on the viewing angle, and I fit the EM and GW datasets together. These two fits are mathematically the same, see Section 2.0.1. However, differences in the posteriors can arise if, in the case of the two separate fits (EM fit with a θ_v GW-informed prior), the prior on the common parameter in the EM fit does not accurately reproduce the θ_{JN} posterior of the GW fit, statistical noise deriving from the sampling aside.

In Fig. 19 two possible priors for the viewing angle are plotted: a Normal distribution with $\mu = 29.0$ deg and $\sigma = 3.5$ deg (estimated from the GW posterior distribution) and the θ_{JN} posterior from the GW fit, transformed into θ_v according to Eq. (58). The main differences lay in the tails of the distributions and propagate in the posteriors. The results of this analysis, in particular the posteriors of θ_c and θ_v (see Section 3.3), carried out using the Normal distribution as GW-informed prior on θ_v, are in Fig. 20, left panel. They are compared with the results of the joint fit of the EM and GW datasets, in the right panel. While until 99.8% probability the contours are similar, at 99.98% there is a clear difference.

In Table 1 these differences are quantified. The first column represents the percentiles of each distribution. In the second column the differences between the θ_v Normal distribution and the GW posterior are written in percentages and refer to the GW posterior distribution, meaning that, for example, when the percentage is negative, the Normal distribution at that percentile predicts a larger angle with respect to the GW posterior distribution. In the third column, the results of the EM fit with the Normal GW-informed prior are compared to the posterior from the EM+GW fit, in this case the percentages refer to the EM+GW fit. In the fourth column the results of the EM fit with the GW posterior as GW-informed prior and the posterior from the EM+GW fit are compared, also in this case the percentages

1 www.gw-openscience.org

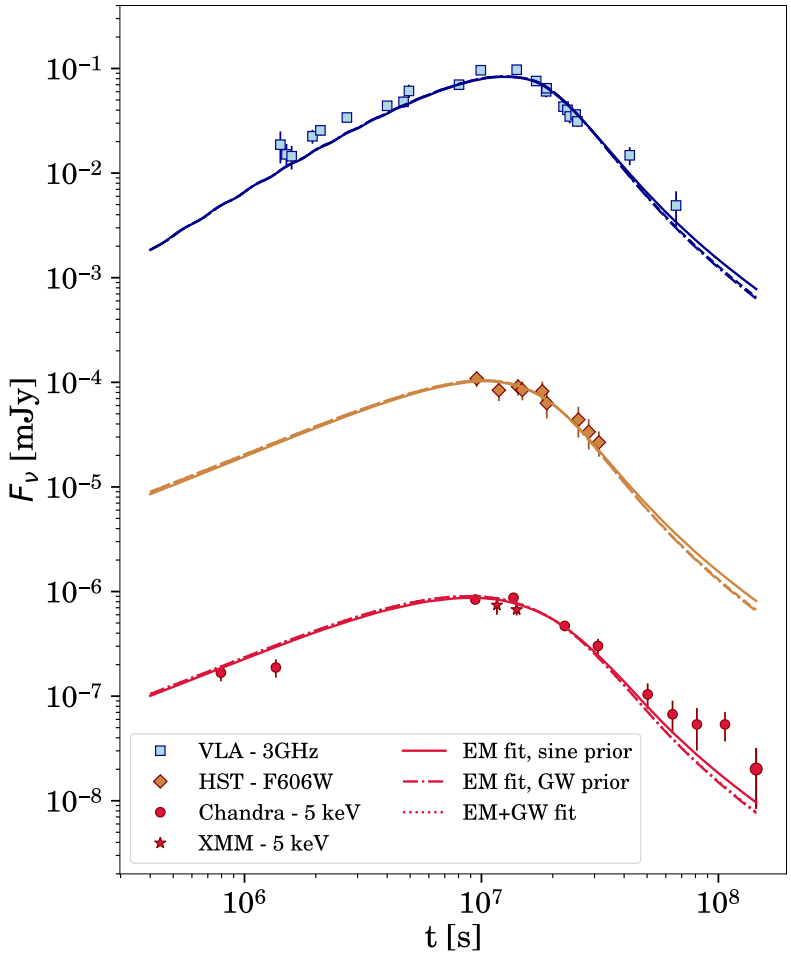

Figure 18: Broad-band afterglow of GW170817: data and fits. From bottom to top, red points refer to the X-ray observations by *Chandra* and *XMM* at 5 keV, orange diamonds to observations by *HST*, F606W filter, in the optical band, and blue squares to observations in the radio band from VLA at 3 GHz. The lines represent fits of the afterglow data: continuous lines are obtained with a prior uniform in the cosine of θ_v (sine prior), dot-dashed lines with a GW-informed prior, and dotted lines with a simultaneous fit of EM and GW data. The last two models are indistinguishable. For sake of simplicity, the fit for the radio band is plotted only for the observations at 3 GHz, but it is not limited to this single frequency.

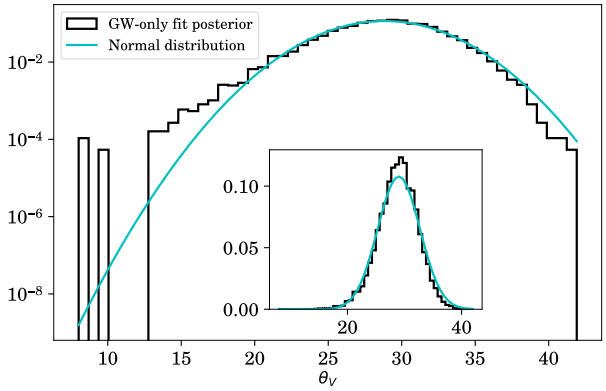

Figure 19: Comparison between the posterior distribution of the viewing angle for the GW-only fit (in black) and the Normal distribution with mean and standard deviation from the GW-posterior distribution ($\mu = 29.0$ deg and $\sigma = 3.5$ deg), in cyan. In the subplot the same distributions are represented, but with a linear vertical axis.

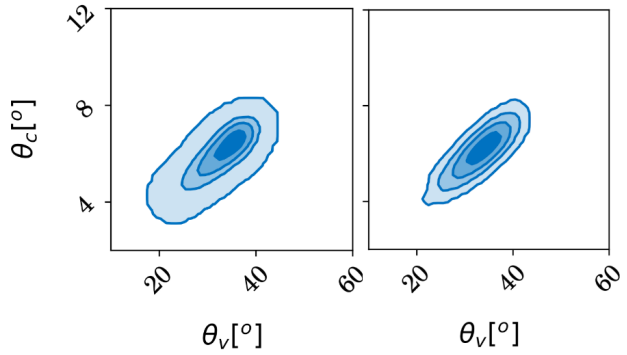

Figure 20: Posterior distributions of the jet opening angle θ_c and the viewing angle θ_v for an EM fit with a GW Normal prior (on the left) and the joint fit (on the right). The contour lines represent the 68.2%, 95.4%, 99.8% and 99.98% probabilities.

refer to the EM+GW fit. This combination is the one used in Section 3.3 and 3.4. This last column, following the mathematical reasoning, should be 0, but it is not because of the statistical noise deriving from the sampling.

From this Table, if we focus on the prior comparison, we can see that the differences between the Normal distribution and the actual GW posterior for θ_{JN} do not go over 8%. At high percentiles the Normal distribution overestimates the actual posterior, while at small percentiles there is an underestimation, except at 0.1-0.01, as is clear also from Figure 19. These differences reflect into the posteriors (third column). In particular, the posterior distribution from the EM fit with the Normal GW-informed prior in the majority of cases predicts larger angles with respect to the EM+GW fit. Instead it is the contrary for the EM fit using as prior the actual GW posterior, but the percentage differences are smaller, especially in the tails of the distribution.

Table 1: In this Table, in the second column, the differences between the θ_v Gaussian prior used in the EM fit with GW-informed prior and the posterior distribution on θ_v of the GW fit are reported, *(GW posterior - Normal distribution)/GW posterior*; in the third column the difference between the θ_v posterior distribution from the EM fit with GW-informed prior and the θ_v posterior of the EM+GW joint fit, *(EM+GW posterior - EM posterior)/EM+GW posterior*; in the fourth column the differences between the posterior from the EM fit with the GW posterior as prior on the inclination and the θ_v posterior of the EM+GW fit, *(EM+GW posterior - EM posterior)/EM+GW posterior*. The latter configuration is used in Sections 3.3 and 3.4. These quantities are represented as function of the percentiles of each distribution (first column).

Percentile [%]	Difference in Prior [%]	Difference in Posterior [%]	Main analysis [%]
0.01	-7.9	9.2	4.2
0.1	-4.2	-6.4	-4.0
2.3	3.0	-2.0	1.2
15.9	3.1	-2.4	1.6
50	1.0	-2.4	2.1
84.1	-1.5	-1.0	2.0
97.7	-3.4	2.0	1.5
99.9	-5.3	6.4	3.0
99.99	-4.1	6.1	2.1

3.3 RESULTS FOR GW170817

In this section, I present the outcomes of three fitting scenarios: the GW-only fit, the afterglow-only fit, and the joint fit. The joint fit improve the determination of the viewing angle compared to an EM-only fit. The EM fits are executed utilizing DYNESTY, while the GW and EM+GW fits BILBY and DYNESTY. Specifically, the dynamic nested sampling method with 2000 livepoints and multiple bounding ellipsoids as a bounding strategy is employed for GW and EM+GW analyses. The generation of corner plots in this study is done using CORNER [84].

3.3.1 *GRB 170817A afterglow and GW170817 analyses*

The results of the GW-only fit are reported in the first column of Table 2. As is commonly the case, I do not quote the individual mass components but the chirp mass, eq. (5), which is the best measured parameter for systems displaying a long inspiral [33, 58, 76, 180], and the mass ratio $q = m_2/m_1 \leqslant 1$. The 6 dimensionless spin degrees of freedom are reported as follows: a_1 and a_2 are the dimensionless spin magnitudes, θ_1 and θ_2 are the tilt angles between the spins and the orbital angular momentum, $\phi_{1,2}$ is the azimuthal angle separating the spin vectors, and ϕ_{JL} is the opening angle of the cone of precession about the system angular momentum. The time of coalescence is not present in this and other tables, as this is of little interest in the context of our study. These results are in agreement with previous works [7, 194]. The error on the inclination angle θ_{JN} is about 5 times smaller with

Table 2: Fit results for GW170817. We report the medians and the 16th-84th percentiles. The angles are quoted in degrees. θ_v and θ_{JN} are related by Eq. (58) and treated as a single parameter.

Parameter	GW-only	EM-only (sine prior)	EM-only (GW-informed prior)	EM+GW
$\log_{10} E_0$		$50.67^{+0.06}_{-0.05}$	$50.75^{+0.07}_{-0.06}$	$50.73^{+0.07}_{-0.06}$
θ_c [deg]		$7.0^{+0.4}_{-0.5}$	$6.1^{+0.3}_{-0.4}$	$6.2^{+0.4}_{-0.5}$
θ_w [deg]		54^{+21}_{-20}	49^{+22}_{-19}	51^{+22}_{-20}
$\log_{10} n_0$		$-3.2^{+0.2}_{-0.2}$	$-3.6^{+0.1}_{-0.2}$	$-3.5^{+0.2}_{-0.2}$
p		$2.14^{+0.01}_{-0.01}$	$2.14^{+0.01}_{-0.01}$	$2.14^{+0.01}_{-0.01}$
$\log_{10} \epsilon_e$		$-0.02^{+0.02}_{-0.03}$	$-0.09^{+0.05}_{-0.05}$	$-0.07^{+0.04}_{-0.06}$
$\log_{10} \epsilon_B$		$-1.8^{+0.1}_{-0.1}$	$-1.6^{+0.2}_{-0.2}$	$-1.7^{+0.2}_{-0.2}$
θ_v [deg]		38^{+2}_{-2}	33^{+2}_{-2}	34^{+2}_{-2}
θ_{JN} [deg]	151^{+3}_{-3}			146^{+2}_{-2}
$\mathcal{M}$	$1.1975^{+0.0001}_{-0.0001}$			$1.1975^{+0.0001}_{-0.0001}$
q	$0.88^{+0.08}_{-0.10}$			$0.88^{+0.08}_{-0.09}$
a_1	$0.02^{+0.02}_{-0.01}$			$0.02^{+0.02}_{-0.01}$
a_2	$0.02^{+0.02}_{-0.01}$			$0.02^{+0.02}_{-0.02}$
θ_1 [deg]	82^{+34}_{-35}			80^{+33}_{-33}
θ_2 [deg]	83^{+36}_{-36}			83^{+36}_{-34}
$\phi_{1,2}$ [deg]	182^{+122}_{-129}			177^{+115}_{-115}
ϕ_{JL} [deg]	179^{+123}_{-123}			177^{+120}_{-121}
ψ [deg]	89^{+61}_{-62}			84^{60}_{-54}
Λ_1	269^{+346}_{-190}			278^{+376}_{-192}
Λ_2	425^{+525}_{-295}			421^{+528}_{-287}

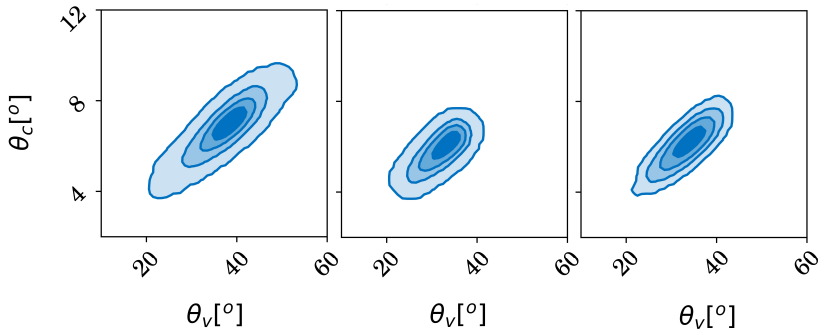

Figure 21: 2D distribution of the viewing angle and jet opening angle. From left to right, the result from the afterglow-only fit with a sine prior on θ_v, afterglow-only fit with GW-informed prior, and the EM+GW fit. The contours represent the 68.2%, 95.4%, 99.8% and 99.98% probabilities.

respect to Romero-Shaw et al. [194], who report $\theta_{JN} = 145^{+17}_{-18}$ deg (68% credible interval). The 90% credible interval of this analysis, for θ_{JN} is 151^{+6}_{-5} deg, which is about 4 times smaller with respect to Abbott et al. [7], that report 146^{+25}_{-27} deg. This simply stems from the fact that, in the analysis presented here, the prior on the luminosity distance is collapsed in one point, which is correlated to θ_{JN}, by fixing it to a single value. Indeed, repeating the GW fit leaving the luminosity distance free with a uniform-in-volume prior (see the works cited above) gives an inclination angle of $\theta_{JN} = 145^{+16}_{-18}$ deg (68% credible interval) and $\theta_{JN} = 145^{+25}_{-27}$ deg (90% credible interval). These results are very much in agreement with Abbott et al. [7] and Romero-Shaw et al. [194].

The broad-band afterglow of GW170817 is fitted assuming a Gaussian structure for the jet and using two different priors on the viewing angle: an isotropic prior uniform in the cosine of θ_v from 0 to 90 deg (referred to as "sine prior") and the θ_{JN} posterior distribution of the GW-only analysis (referred to as "GW-informed prior"), where θ_{JN} is transformed in θ_v via Eq. (58). The results of the analysis of the afterglow data with two distinct priors are summarized in the second and third column of Table 2. The values of the parameters concerning the geometry, the energetics, and the microphysics are in agreement within 1σ across the two fits. The slope of the electron energy distribution p is very well constrained and is identical in all fits, this is due to the very well sampled spectral shape, as we already mention in Seciton 1.2.5. The viewing angle goes from a median value of 38 deg for the sine prior to 33 deg for the GW-informed prior. These results are in agreement with Troja et al. [225], who used the same dataset of this work, except for the most recent Chandra data point. Despite the decrease in the viewing angle with the GW-informed prior, θ_v is still in tension with the analysis of the centroid motion in the radio observations Ghirlanda et al. [93] and Mooley et al. [154], that predict a $\theta_v \sim 20$ deg. This discrepancy is due to the flattening of the late time observations in the X-rays, which is driving the viewing angle toward higher values (see the following Chapter for an extensive discussion). As pointed out in Troja et al. [225], the addition of an extra-component in the flux producing the late

time observations could resolve this discrepancy, because it would allow the jet to be narrower and closer to the line of sight [21, 108, 225].

3.3.2 *Joint analysis*

The parameter medians and 16th-84th percentiles of the joint EM+GW fit are collected in the last column of Table 2. In Fig. 21 the marginalised, 2D posterior probability distribution are reported for the jet opening angle θ_c and the viewing angle θ_v in the three cases these parameters are measured within our setups: namely, from left to right, the EM-only fit with sine prior, the EM-only fit with GW-informed prior, and the joint EM+GW fit. While there is a degeneracy in the EM-only fit, including the GW information (either as a prior or as an additional independent dataset) still leaves the degeneracy, but reduce the dispersion. This happens because the EM dataset alone already constrains very well the two angles, especially thanks to the late time detections in the X-rays. The EM fit with the GW informed prior and the EM+GW joint fit are equivalent, as proven in Section 2.0.1. The advantage of performing an EM+GW joint fit is the back-reaction of the GRB analysis on the GW parameters, in this case though the GW parameters remain almost the same. This is because the inclination of the binary is degenerate with the luminosity distance, which is, however, fixed in this work. We will explore the case of a free luminosity distance analysis in the next Chapter.

We obtain an inclination of $\theta_{JN} = 146^{+2}_{-2}$ deg (68% credible interval), which translates into a viewing angle $\theta_v = 34^{+2}_{-2}$ deg. These values are consistent with the ones retrieved with the EM-only fit when using the GW-informed prior. The error on the common parameter, θ_N, from the joint EM+GW fit is 1.5 times smaller than for the GW-only fit.

3.4 GW170817-LIKE EVENT IN O4

As GW170817 was a nearby and rare event, in this section the analyses presented above are repeated in the scenarios of a GW170817-like source located at 136.5 Mpc and at 70 Mpc (redshift $z = 0.03$ and $z = 0.016$), observed in the LIGO-Virgo-KAGRA Fourth Observing Run (O4). The increase in distance has the effect of reducing by roughly an order of magnitude and a factor of three the flux of the afterglow respectively. These distances were within the originally predicted horizons of LIGO and Virgo for O4 (which, however, are not the real ones, once O4 started[2]). The number of binary neutron stars mergers expected in O4 is of the order of 10 ($\leqslant 10$ in Abbott et al. [8] and Abbott et al. [10] or $34^{+78}_{-25}\mathrm{yr}^{-1}$ in Petrov et al. [173]). I simulated 10^5 events, assuming that all binaries produce a successful jet, producing light curves with the same energetics and microphysics parameters as GW170817 (see Table 2, last column), distributed uniformly in volume up to 190 Mpc and with jet axes isotropically distributed. 25% of events reach peak fluxes above the *Chandra* sensitivity, concluding that the X-ray afterglow of $\leqslant 3$ GW170817-like binary neutron stars mergers could be detected during O4. This rate is in agreement with Colombo et al. [54], Patricelli et al. [172], Petrov et al. [173], Wang and Giannios [236], and Wang et al. [238]. I note that, in this Section,

2 https://dcc.ligo.org/LIGO-G2002127/public

a GW170817-like event is presented, meaning that all physical parameters are assumed to be the same as GW170817. This, in reality, is very unlikely, as a different source means also different physical parameters, including different inclinations (for example, a smaller inclination would result in a stronger flux), therefore, the presented estimates are subject to large uncertainty.

3.4.1 *Building the dataset*

In the EM sector, I rescaled the afterglow of GW170817 for the luminosity distance of 136.5 Mpc (or 70 Mpc). In the case of 136.5 Mpc, for example, this reduces the flux of about one order of magnitude, as seen by comparing Figs. 22 and 18. The observing strategy adopted is minimal and conservative: starting from 9 days, which is the first detection in the X-rays of GW170817, we have an observation every 4 weeks until the peak. After that, equally spaced (in log space) observations are placed in the following time decade. The details for each band are as follows.

- Radio — Only the (rescaled) VLA observations at 3 GHz are considered. We assign an error of 2μJy, which is the root-mean-square error estimated for more than 3 hr of observations [218].
- Optical — For the *HST* optical observations, and, in particular, their uncertainties, I studied the contributions of source, background, readnoise and noise from the dark current [60]. The *HST* readnoise and the dark current are negligible with respect to the source and sky contributions. The source weights 10–20% of the error, so the error is dominated by the sky (background). Only the source part of the error, then I estimated the error contribution of the sky assuming an exposure time of 5 ks, and sum in quadrature the two components to have the final error on the optical fluxes.
- X-ray — I used the software XSPEC[3] [17] to generate the X-ray observations taking into account the *Chandra* response and background[4].

Finally, in order to make this result valid for real observations, I checked the sensitivity of the instruments. The Chandra sensitivity for 100 ks exposure is about 2.7×10^{-8} mJy (3σ at 5 keV). For VLA, we use a 3σ sensitivity of 6μJy (see above). For HST, I assume a 3σ limiting magnitude of about 30 ABmag, which could be reached stacking different images together. For this reason an exposure time of 5 ks is chosen when treating the errors. Figure 22 depicts the final EM dataset for the putative, GW170817-like O4 event at 136.5 Mpc. The sensitivity of each instrument is represented by a horizontal line. In this case, all three instruments can detect only the peak of the afterglow. The data points below the sensitivities are kept in the analysis, as they will play a major role in constraining the jet opening angle and the viewing angle. There is no data point at 9 days in the optical band because at that time the kilonova dominates the emission.

In the GW sector, I use BILBY to produce a GW signal from a source with the same features as GW170817, but located at 136.5 Mpc (70 Mpc), and inject it in the nominal O4 noise curves[5] for the LIGO-Livingston, LIGO-Hanford and Virgo

3 Xspec Home Page
4 *Chandra* X-ray Observatory
5 https://dcc.ligo.org/LIGO-T2000012/public

detectors. The KAGRA detector is not included in this analysis, since a binary neutron star at ~ 140(70) Mpc would be beyond its expected sensitivity range. This simulated event has a network signal-to-noise ratio of 26.3 (50), as opposed to the GW170817 network signal-to-noise ratio of 32.4. It is to be noted that, even if the 70 Mpc event is further than GW1708717, the signal-to-noise is larger thanks to the improved sensitivity of the interferometers.

In order to validate this GW+EM injection setup, I simulate an event similar to GW170817 with the O2 interferometers noise curves. The injected GW signal has the same parameters of GW170817, including the luminosity distance (see Table 2, first column). The EM dataset is composed of the same detection times and flux errors of the GW170817 broad-band afterglow, but we adopt the flux predicted by the model (and not the real, detected, one). Jointly fitting this simulated EM+GW dataset leads to the same results of the real GW170817, so the injection set up can be safely used for the following analysis of the other events.

3.4.2 *Results for a distance of 136.5 Mpc*

The EM and GW datasets described above are fitted using BILBY and DYNESTY (dynamic nested sampling method with 2000 livepoints and multiple bounding ellipsoids). For this event, in the contour plots we will see only the results from the EM-only and the EM+GW joint fit, being the EM fit with GW-informed prior equal to the latter, as already demonstrated for GW170817 (Section 3.3). The results are reported in Table 3, Fig. 22, and Fig. 23. The table lists 68% credible intervals for the parameters involved in the GW-only, EM-only, and joint fit. Fig. 22 shows the 68% uncertainty regions of the fits to the afterglow data; this involves three analyses (afterglow-only fit with sine-prior for θ_v, afterglow-only fit with GW-informed-prior for θ_v, and the joint EM+GW fit) performed over three EM bands (radio, optical, and X-ray). Finally, Fig. 23 displays the contour plots of the marginalized 2D posterior density distributions for θ_v and θ_c obtained for the analyses involving the EM dataset and the EM+GW fit.

The GW-only fit retrieves posteriors (second column in Table 3) consistent with the injected values (first column in Table 3). The signal-to-noise ratio of our putative event is not very different from that of GW170817, it is less than the GW170817 signal-to-noise ratio by a factor of ~ 1.2, so also the posteriors are very similar to the case of GW170817 discussed in the previous sections, with the exception of the tidal parameters, where the errors are reduced by a factor of about 2. This is due to the fact that in this case we are not dealing with real data, and are therefore not subject to a specific noise realization, believed to be at the origin of the bimodal distribution for the tidal deformability in the case of GW170817 (see the discussion and Fig. 11 of [7]). In this case, following Eq. (58), the posterior distribution for θ_{JN} translates into a viewing angle of 30^{+6}_{-6} deg (68% credible interval around the median).

Overall, we find that the uncertainties on the EM parameters are larger with respect to the analysis of the afterglow of GW170817 (see Table 2). This is due to the fact that the (simulated) decrease in EM flux drives several detections below the sensitivity of the instruments. However, the $<3\sigma$ data points help to constrain the EM parameters, especially the jet opening angle. From Table 3 it is clear that in the EM case both angles are unconstrained, while including the GW domain

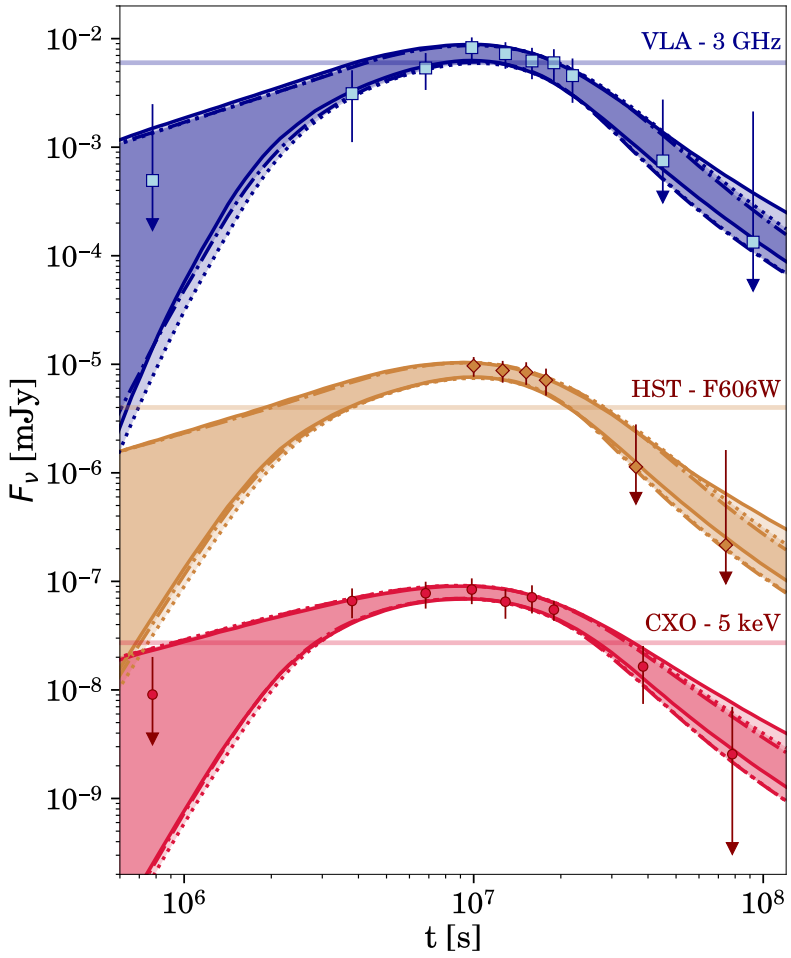

Figure 22: Broad-band afterglow of a GW170817-like event at 136.5 Mpc: rescaled data and fits. From bottom to top, red dots are X-ray observations by Chandra at 5 keV, orange diamonds are the observations by HST, F606W filter, in the optical band, and blue squares are VLA observations 3 GHz. The arrows indicate that the 1σ error reaches 0 flux. The shaded regions and solid, dot-dashed, and dotted lines represent the 68% uncertainty regions of the models envelope from the EM-only (sine prior), EM-only (GW prior), and EM+GW fits of the afterglow, respectively. Note that the EM with GW prior and EM+GW fits have almost identical uncertainty regions. The horizontal shaded lines represent the sensitivity of *Chandra* (red, 2.7×10^{-8}mJy, 3σ), *HST* (orange, 4×10^{-6}mJy, 3σ) and VLA (blue, 6×10^{-3}mJy, 3σ).

Table 3: Fit results for a GW170817-like event at 136.5 Mpc. We report the medians and the 16th-84th percentiles. The angles are quoted in degrees. θ_v and θ_{JN} are related by Eq. (58) and treated as a single parameter. In the first column there are the values injected in the GW signal.

Parameter	Injection	GW-only	EM-only (sine prior)	EM-only (GW-informed prior)	EM+GW
$\log_{10} E_0$			$51.6^{+1.0}_{-0.7}$	$52.0^{+1.2}_{-1.0}$	$52.1^{+1.1}_{-1.0}$
θ_c [deg]			11^{+13}_{-4}	7^{+13}_{-1}	7^{+15}_{-2}
θ_w [deg]			39^{+28}_{-20}	36^{+31}_{-20}	29^{+34}_{-14}
$\log_{10} n_0$			$-1.0^{+1.0}_{-1.4}$	$-2.0^{+1.2}_{-1.0}$	$-2.0^{+1.1}_{-1.1}$
p			$2.12^{+0.03}_{-0.04}$	$2.12^{+0.04}_{-0.04}$	$2.12^{+0.04}_{-0.04}$
$\log_{10} \epsilon_e$			$-0.9^{+0.6}_{-0.9}$	$-1.2^{+0.9}_{-1.2}$	$-1.2^{+0.9}_{-1.2}$
$\log_{10} \epsilon_B$			$-3.7^{+1.0}_{-0.8}$	$-3.3^{+1.2}_{-1.1}$	$-3.4^{+1.3}_{-1.1}$
θ_v [deg]			50^{+19}_{-16}	36^{+3}_{-3}	36^{+3}_{-3}
θ_{JN} [deg]	151	150^{+6}_{-6}			144^{+3}_{-3}
$\mathcal{M}$	1.1975	$1.1975^{+0.0001}_{-0.0001}$			$1.1975^{+0.0001}_{-0.0001}$
q	0.88	$0.89^{+0.07}_{-0.09}$			$0.89^{+0.07}_{-0.09}$
a_1	0.02	$0.02^{+0.02}_{-0.01}$			$0.02^{+0.02}_{-0.01}$
a_2	0.02	$0.02^{+0.02}_{-0.01}$			$0.02^{+0.02}_{-0.02}$
θ_1 [deg]	82	80^{+37}_{-33}			78^{+34}_{-34}
θ_2 [deg]	83	83^{+35}_{-35}			83^{+34}_{-34}
$\phi_{1,2}$ [deg]	182	179^{+123}_{-123}			169^{+124}_{-111}
ϕ_{JL} [deg]	179	179^{+118}_{-119}			182^{+114}_{-123}
ψ [deg]	89	89^{+56}_{-65}			88^{+56}_{-63}
Λ_1	260	148^{+182}_{-107}			148^{+191}_{-106}
Λ_2	430	221^{+279}_{-155}			223^{+261}_{-157}

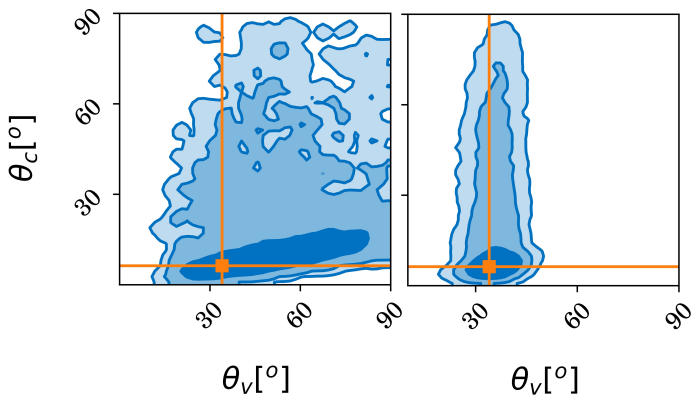

Figure 23: 2D distribution of the viewing angle and jet opening angle for a GW170817-like event located at 136.5 Mpc. On the left, the result from the afterglow-only fit with a sine prior on θ_v, on the right the EM+GW fit. The contours represent the 68.2%, 95.4% and 99.8% probabilities. The orange squares represents the values used to simulate the observations (see Table 2, last column) for θ_c and θ_v.

helps constraining the viewing angle, but not the jet opening angle. To show the relevance of the <3σ data points I excluded them from the analysis, leading to medians and 16th-84th percentiles: $\theta_v = 64^{+21}_{-17}$ deg and $\theta_c = 45^{+27}_{-25}$ deg in the case of an EM-only fit; $\theta_v = 36^{+3}_{-3}$ deg and $\theta_c = 35^{+31}_{-26}$ deg in the EM+GW case. The absence of these data points mainly affects the jet opening angle, which in the EM+GW (EM) case has an 84th percentile of 66deg (72deg), these values are 3 times larger than the ones written in Table 3 and estimated including the <3σ data points in the analysis.

In Table 3, for the EM fit with a sine prior, the viewing angle is 50^{+19}_{-16} deg, which is compatible within 1σ with the injected value from GW170817. The credible interval, however, is still larger than the one for GW170817, indicating that an afterglow-only analysis of an event of this kind would not provide a stringent measurement of the viewing angle. Also the jet opening angle of 7^{+15}_{-2} deg is in agreement with the GW170817 result, but the uncertainty is large. The situation improves when we use the θ_{JN} posterior distribution from the GW-only analysis, transformed into θ_v, as the GW-informed prior for the EM fit. In this case, we find a viewing angle of 36^{+3}_{-3} deg, which is in agreement with the GW170817 results presented in Sec. 3.3. This improvement follows directly from the use of a more informative prior θ_v. Despite this improvement in the measure of θ_v, the jet opening angle uncertainty is still large because the rising part of the afterglow is characterized only by <3σ data points. Also in this case, all the parameters regarding the microphysics and the energetics of the jet are in agreement with the respective GW170817 values within 2σ.

The case of the EM+GW joint analysis is very similar to the afterglow-only analysis with the GW-informed prior, as expected. The uncertainty on the viewing angle at 1σ, 36 ± 3 deg ($^{+6}_{-5}$ deg, 90% credible interval) is about 6 times smaller when compared to the EM-only analysis with sine prior, 50^{+19}_{-16} deg ($^{+30}_{-24}$, deg 90% credible interval), and 2 times smaller than the GW-only analysis 150 ± 6 deg (±7 deg, 90% credible interval).

In this scenario, θ_c at the 2σ level remains unconstrained by the EM data (see Fig. 23), for the reasons discussed previously. The large errors in θ_c of all three analyses translate into the large shaded regions in Fig. 22, which represent the 68% uncertainty regions. The latter concentrate in the rise of the afterglow, furthermore, the EM analysis with sine prior (light shaded region) yields to higher flux values at late times, due to the large viewing angle.

For this event, at 2σ there are cases where $\theta_v < \theta_c$ (see for example Fig. 23), however, those same cases have also $\theta_w < \theta_c$. This means that the jet ends at θ_w and the angle relevant to discriminate between the on-axis or off-axis case is θ_w. When this is true, the jet is a top hat, which does not have wings, but just a uniform core ending at θ_w. In these cases, the jet is still off-axis if $\theta_v > \theta_w$, but the structure changed. The parameter estimation returns a top hat geometry ($\theta_w < \theta_c$) with a 23% posterior probability for the EM+GW fit, a 45% posterior probability for the EM fit with GW-informed prior and a 43% posterior probability for the EM-only fit.

In order to discern between the on-axis and off-axis cases in the samples, we define a new parameter, θ_J, the total width of the jet, that assumes the minimum value between θ_w and θ_c. The 2D posterior distribution of θ_J and θ_v is represented in Fig. 24, where the red dashed line represents the $\theta_J = \theta_v$ line. It is clear that the

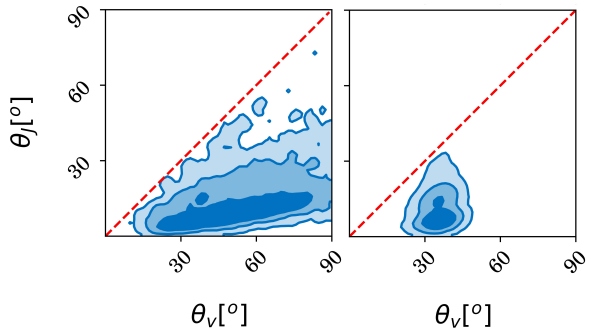

Figure 24: 2D distribution of the viewing angle and θ_J, the jet width, for a GW170817-like event located at 136.5 Mpc. On the left, the result from the afterglow-only fit with a sine prior on θ_v, on the right the EM+GW fit. The contours represent the 68.2%, 95.4% and 99.8% probabilities. The red dashed line represents the $\theta_J = \theta_v$ line.

fit predicts an off-axis observer, with a reduced scatter in the viewing angle when introducing the GW domain. The medians and 16th-84th percentiles for θ_J are: in the case of the EM-only fit $\theta_J = 11^{+7}_{-4}$ deg, in the case of the EM fit with GW-informed prior $\theta_J = 7^{+6}_{-1}$ deg and in the EM+GW case $\theta_J = 7^{+6}_{-2}$ deg.

This analysis shows that, in the case of a large distance event, the data are consistent within 1σ with a Gaussian geometry, but we cannot completely rule out a top hat geometry.

3.4.3 *Results for a distance of 70 Mpc*

In order to study how the degeneracy between the jet opening angle and the viewing angle changes with distance, I also simulate another GW170817-like event, located at the intermediate distance of 70 Mpc ($z \sim 0.016$). This increase in distance reduces by roughly a factor of three the flux of the afterglow. The EM and GW datasets are generated as explained in Section 3.4.1. For this event, in the radio band the first and the last two data points, in the optical and X-ray the last data point are below the sensitivities, the light curve is represented in Fig. 25. It is clear that the rising phase at 70 Mpc is better measured than at 136.5 Mpc.

Notwithstanding the larger distance, the GW event has an improved signal-to-noise ratio by a 1.5 factor with respect to GW170817 thanks to the improved interferometer performances predicted in O4. This explains the smaller errors in θ_{JN}, $\mathcal{M}$ and q (see Table 4). The considerations done in Section 3.4.2 about the tidal parameters are valid also in this case. The results of the fitting are listed in Table 4.

All the EM parameters are in agreement with GW170817 within 2σ. The reduced uncertainty on the parameters with respect to the 136.5 Mpc event translates into narrower 68% uncertainty regions, represented in Fig. 25. The $\theta_v - \theta_c$ posterior distribution is shown in Fig. 26, second row. It is clear that the jet opening angle and the viewing angle are better constrained than the large distance event in all fits, and $\theta_v > \theta_c$ always, as in the case of GW170817. However, there is still a strong degeneracy in the EM-only fit, which is completely broken including the GW domain (leading also to slightly smaller EM+GW shaded regions in Fig. 25 with respect to the EM-only fit). This is not happening for GW170817 because the

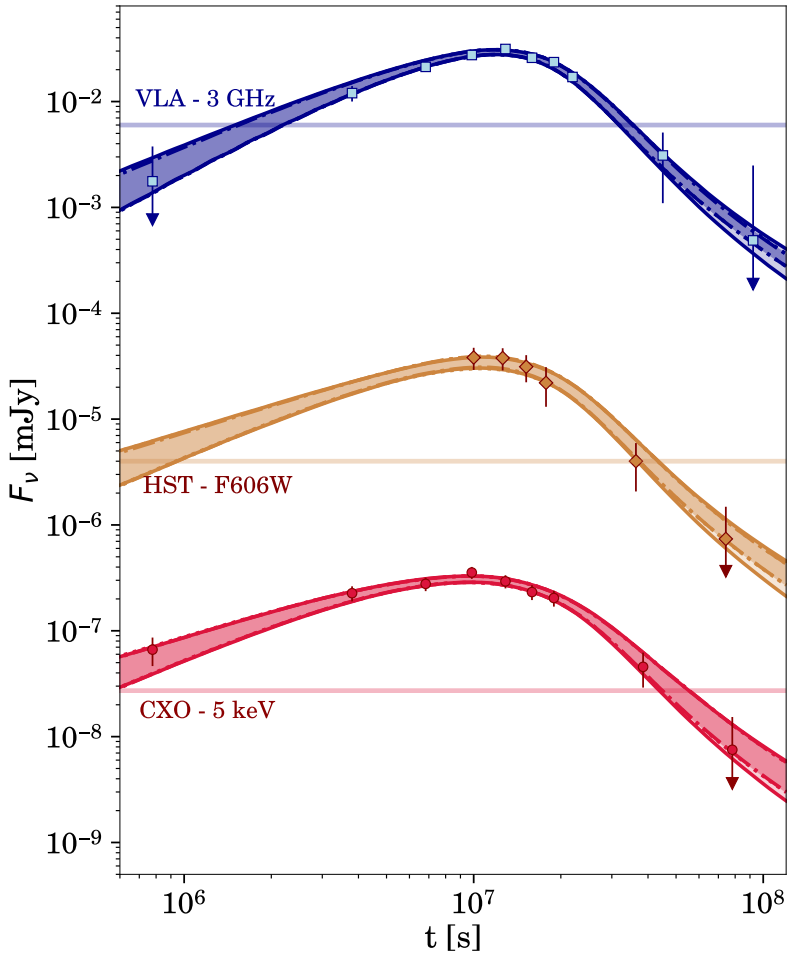

Figure 25: Broad-band afterglow of the GW170817-like event at 70 Mpc: rescaled data and fits. From bottom to top, red dots are X-ray observations by Chandra at 5 keV, orange diamonds are the observations by HST, F606W filter, in the optical band, and blue squares are VLA observations 3 GHz. The arrows indicate that the 1σ error reaches 0 flux. The horizontal shaded lines represent the sensitivity of *Chandra* (red, 2.7×10^{-8}mJy, 3σ), *HST* (orange, 4×10^{-6}mJy, 3σ) and VLA (blue, 6×10^{-3}mJy, 3σ). The shaded regions and solid, dot-dashed, and dotted lines represent the 68% uncertainty regions of the models envelope from the EM-only (sine prior), EM-only (GW prior), and EM+GW fits of the afterglow, respectively. Note that the EM with GW prior and EM+GW fits have identical uncertainty regions.

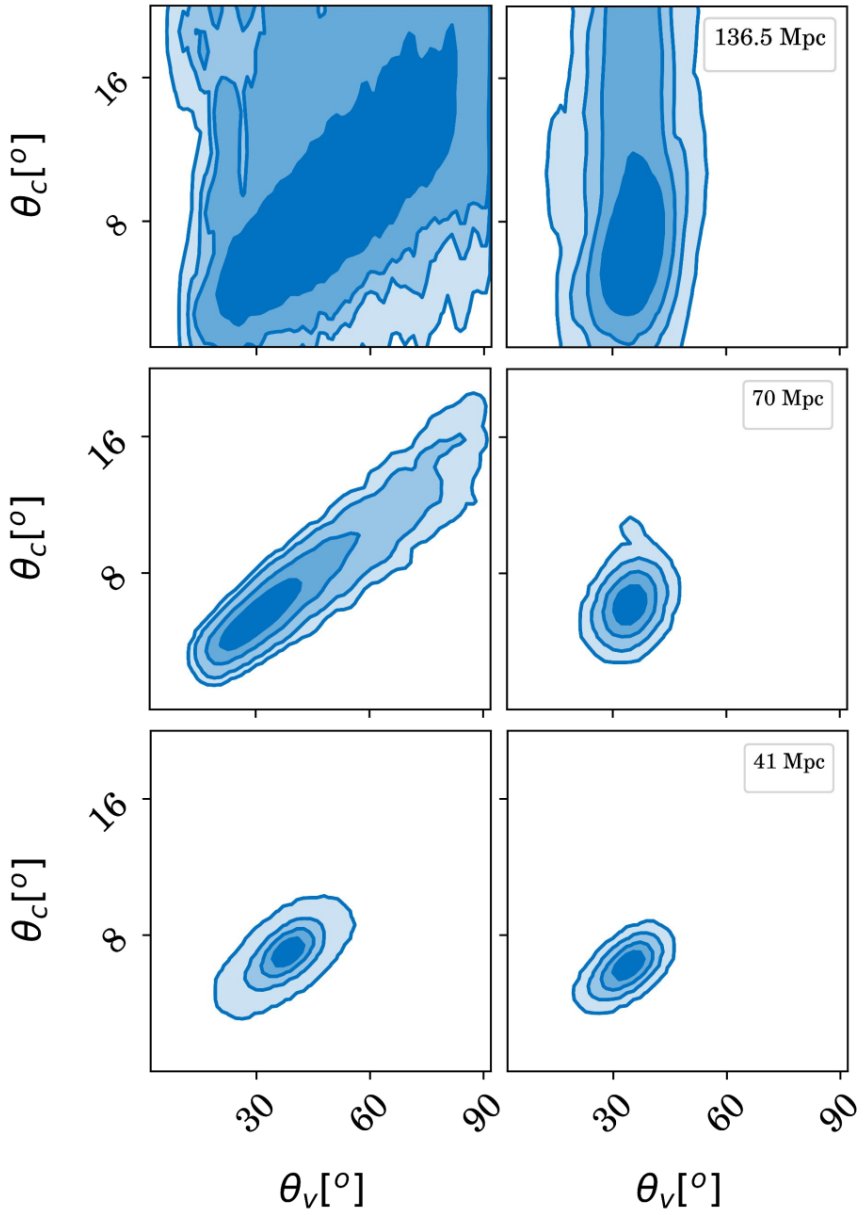

Figure 26: 2D posterior distributions of the EM-only fit (first column) and the joint EM+GW fit (second column). In the first row the event at 136.5 Mpc is represented, in the second row the simulated event at 70 Mpc and in the third row the GW170817 event. The contour lines represent the 68.2%, 95.4%, 99.8% and 99.98% probabilities. The posteriors shown in the first row are the same as Fig. 23, with a different scale for θ_c. It is to be noted that the event at 41 Mpc (GW170817) occurred in the second observing run (O2), while the other events are simulated using the O4 noise curves of the LIGO and Virgo interferometers.

Table 4: Fit results for a GW170817-like event at 70 Mpc. We report the medians and the 16th-84th percentiles. The angles are quoted in degrees. θ_v and θ_{JN} are related by Eq. (58) and treated as a single parameter. In the first column there are the values injected in the GW signal.

Parameter	Injection	GW-only	EM-only (sine prior)	EM-only (GW-informed prior)	EM+GW
$\log_{10} E_0$			$51.1^{+1.4}_{-0.3}$	$51.0^{+1.2}_{-0.2}$	$51.0^{+1.0}_{-0.2}$
θ_c [deg]			6^{+2}_{-1}	$6.1^{+0.6}_{-0.6}$	$6.0^{+0.6}_{-0.6}$
θ_w [deg]			53^{+21}_{-22}	54^{+21}_{-21}	52^{+22}_{-22}
$\log_{10} n_0$			$-3.2^{+1.5}_{-0.8}$	$-3.3^{+1.2}_{-0.2}$	$-3.2^{+1.0}_{-0.3}$
p			$2.14^{+0.03}_{-0.03}$	$2.14^{+0.02}_{-0.03}$	$2.14^{+0.02}_{-0.03}$
$\log_{10} \epsilon_e$			$-0.2^{+0.2}_{-1.3}$	$-0.2^{+0.1}_{-1.1}$	$-0.2^{+0.1}_{-0.8}$
$\log_{10} \epsilon_B$			$-2.1^{+0.6}_{-1.5}$	$-2.0^{+0.4}_{-1.2}$	$-2.1^{+0.4}_{-1.1}$
θ_v [deg]			32^{+9}_{-7}	34^{+2}_{-2}	35^{+2}_{-2}
θ_{JN} [deg]	151	150^{+2}_{-2}			145^{+2}_{-2}
$\mathcal{M}$	1.1975	$1.19747^{+0.00004}_{-0.00003}$			$1.19747^{+0.0004}_{-0.0003}$
q	0.88	$0.89^{+0.07}_{-0.08}$			$0.89^{+0.07}_{-0.08}$
a_1	0.02	$0.02^{+0.02}_{-0.01}$			$0.02^{+0.02}_{-0.01}$
a_2	0.02	$0.02^{+0.02}_{-0.01}$			$0.02^{+0.02}_{-0.02}$
θ_1 [deg]	82	83^{+32}_{-33}			82^{+33}_{-33}
θ_2 [deg]	83	84^{+35}_{-35}			84^{+34}_{-35}
$\phi_{1,2}$ [deg]	182	179^{+124}_{-124}			179^{+124}_{-122}
ϕ_{JL} [deg]	179	180^{+122}_{-126}			182^{+120}_{-123}
ψ [deg]	89	87^{+54}_{-64}			88^{+55}_{-63}
Λ_1	260	161^{+158}_{-110}			162^{+151}_{-109}
Λ_2	430	236^{+224}_{-163}			237^{+213}_{-159}

presence of the correlation at 41 Mpc in the EM+GW fit is due to the small errors on the angles from the EM modelling, that do not leave much margin of improvement. At this distance, the jet opening angle is very well constrained, with an about 10% error in the EM+GW case, with respect to the large distance event (more than 100% error).

3.5 SUMMARY AND FINAL REMARKS

In this Chapter, Bayesian analysis is used to analyze both the GW and EM afterglow data for the multi-messenger event GW170817. The same methodology is extended to two GW170817-like events situated at greater distances and occurring during the O4 observing run. The luminosity distance is held constant, adhering to the standard practice in afterglow property analysis, and the jet is assumed to exhibit a Gaussian structure. This study aims to discern whether a joint fit of EM and GW data offers improvements compared to fitting these datasets independently or using informed priors. Additionally, we explore the equivalence between a joint

fit and an EM fit with a GW-informed prior, provided that the genuine posterior from the GW analysis is utilized as the prior for the EM analysis. Conversely, using an approximation of the GW posterior as a prior may introduce disparities in the resulting posteriors.

The GW and EM domains share a common parameter, namely the inclination angle θ_{JN} (from the GW) and the viewing angle θ_v (from the EM side), which are related by Eq. (58). In the EM model used to process the data, the jet opening angle θ_c and θ_v are correlated: it is shown that a joint analysis of the two messengers can ease or break this degeneracy and provide more accurate measurements of θ_v than those obtained analysing the GW or the EM data alone.

A comprehensive summary of the results for the measurement of θ_v in the extreme cases of GW170817 and of the large distance event at 136.5 Mpc is shown in Fig. 27, where, for both scenarios, the prior on θ_v is compated to the posterior on the same quantity obtained by: 1) processing only the GW data (and applying Eq. (58) to convert the θ_{JN} measurement), 2) processing only the EM data when assuming a uniform prior on the cosine of θ_v ("sine prior"), 3) processing separately the GW and the EM data, using the θ_{JN} posterior distribution as prior on θ_v, and 4) processing both datasets simultaneously.

We see that in the GW only analyses (first prior-posterior pair from the left in each panel), from a sine prior we get a clean, peaked posterior distribution for the viewing angle. In the case of the analysis based on EM data alone (second prior-posterior pair from the left), GW170817 yields a peaked distribution with long tails due to the θ_c–θ_v degeneracy. These grow as the distance to the source increases, as shown by the GW170817 simulated event for O4 discussed in the previous section, for which the posterior mildly differs from the prior. Likewise, the value of the jet opening angle θ_c at 136.5 Mpc has a large scatter and it is recovered as 11^{+13}_{-4} deg. The degrading of the measurement of θ_v and θ_c with source distance is mainly due to the fact that the rise of the afterglow drops below the sensitivity of all instruments: this part is what places the most stringent constraints on the ratio of the two angles.

The situation improves when the EM data is processed with a prior on θ_v that is informed by the GW measurement of θ_{JN}. This is the case of the third prior-posterior pair from the left in both panels, where the prior is the posterior of the first case. This GW-informed prior acts on the θ_c–θ_v degeneracy: it reduces the tails in the posterior for θ_v and shifts the median to a lower value. However, when the source is moved further out (bottom panel), the EM data is not informative and simply allows us to recover the prior. The results for the EM data with two distinct priors tell us that the prior choice can be crucial, particularly when the afterglow data is not sampled extensively enough throughout the rise, peak, and decay.

Finally, the case of the EM+GW joint fit with a sine prior on the viewing angle gives a conclusive result on this parameter, in agreement with the EM analysis with the GW-informed prior (as expected). Regarding GW170817, it drives the median to a lower value than the EM-only fit (mostly, as already said above, by "cutting" the tails of the θ_v posterior) and it reduces the width of the distribution by a factor $\sim$ 1.5 with respect to the GW-only fit. For the GW170817-like event located at 136.5 Mpc and occurring in O4, these trends are confirmed. Both in the EM with GW-informed prior and in the EM+GW analysis, all fits prefer an off-axis observer, but the jet opening angle measurement retains a large scatter, due to the

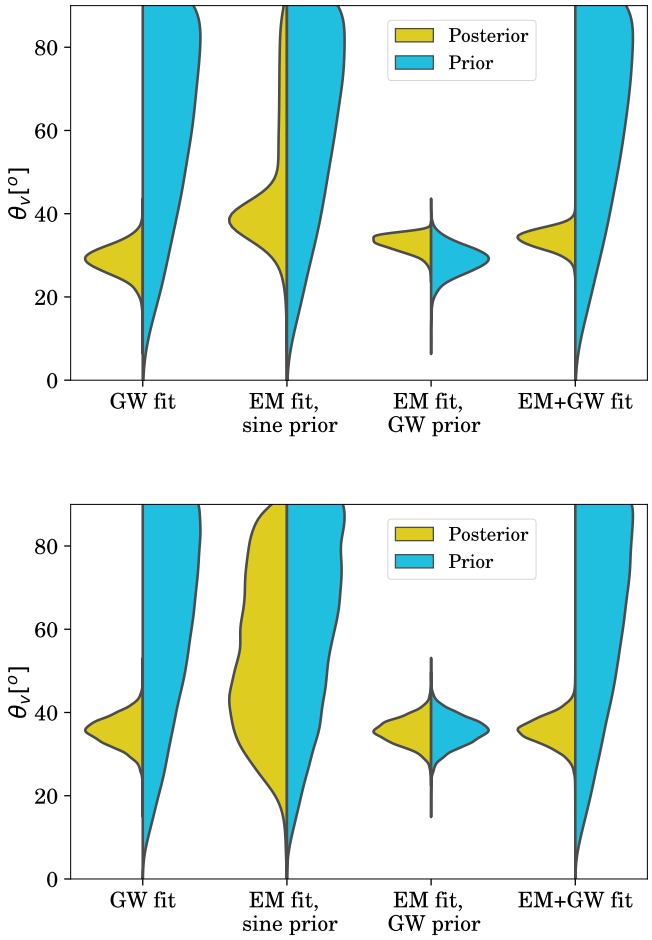

Figure 27: Prior (cyan) and posterior (yellow) distributions of the viewing angle θ_v for the analyses carried out on GW170817 data (top panel) and a simulated GW170817-like event in O4 (bottom panel). In both panels, the cyan distributions represent a distribution uniform in the cosine of the angle with the exception of the third case from the left, where the prior distribution corresponds to the posterior from the GW analysis (represented in yellow in the first case from the left).

fact that the data points in the rising part of the afterglow are below the sensitivity of the instruments. As mentioned previously, data from this stage of the afterglow strongly constrains the ratio θ_v/θ_c. For the same reason, for this large distance event, it is hard to derive a conclusive information on the geometry of the jet, as, the values of the jet opening angle and the wing truncation angle θ_w are consistent at 1σ with a Gaussian geometry, and above that with a Gaussian geometry with $\theta_w < \theta_c$, which corresponds to a top hat geometry. However, both in the EM-only fit and the EM and GW fits, the jet total width is constrained to be lower than the viewing angle, thus pointing to an off-axis jet.

A summary of the study on the degeneracy between the jet opening angle θ_c and the viewing angle θ_v for different distances is represented in Fig. 26. Here the 2D posterior distributions for the distant event at 136.5 Mpc, the intermediate distance event at 70 Mpc and GW170817 are represented in the first, second and third row respectively (note that GW170817 occurred in O2, while the other events are simulated with the O4 interferometers sensitivities). In the EM fit (first column) the further is the event, the worse is the degeneracy, leaving at 136.5 Mpc the two angles unconstrained above 1σ. Including the GW domain (second column) acts only on θ_v, so at large distance θ_c is still unconstrained above 1σ for the reasons we already pointed out. At 70 Mpc the EM dataset can constrain better these angles, but there is still a strong degeneracy, which is broken by the GW domain. At 41 Mpc the angles are already very well constrained, thanks to the well sampled light curve, especially at late times in the X-rays, so the GW domain ease the degeneracy, but does not break it.

In O4 (which will run up to early 2025), we anticipate detecting binary neutron star mergers up to a distance of approximately 200 Mpc [173]. This chapter illustrates that, particularly at substantial distances, the capabilities of current electromagnetic (EM) instruments may prove insufficient to resolve the degeneracy between the jet opening angle and the viewing angle. Consequently, the incorporation of GW data becomes indispensable.

To effectively observe the rising and declining slopes of the afterglow, especially at significant distances, instruments with heightened sensitivities are required. Examples include *Athena* in the X-rays [178] or SKA in the radio band (Square Kilometer Array [39]), which can offer improved characterization of event properties, extending the EM observational horizon to greater distances and larger viewing angles. This enhancement is crucial for breaking degeneracies and gaining a more comprehensive understanding of the events, particularly as we explore binary neutron star mergers at higher distances.

4

TO COSMOLOGY

Binary NS mergers are interesting events not only from an astrophysical point of view, but also for cosmology. In fact, the luminosity distance of a GW source can be estimated simply from fitting the waveform, relying only on the general theory of relativity, and this estimation does not depend on cosmic distance ladders. For this reason, a GW event (its luminosity distance) can be used to determine the Hubble constant H_0, the current expansion rate of the Universe, provided that the redshift of that source is known thanks to an EM counterpart, for example a kilonova [74, 222]. This is the so-called standard sirens method [119, 162]. Even when a unique counterpart cannot be identified, the redshifts of all the potential host candidates can be incorporated in the analysis, when the localization volume is sufficiently small. This is not as constraining as the first scenario, but it is still informative, once many detections are available. In this case, more than 50 binary neutron stars are needed to reach a 6% H_0 measurement [50]. The same holds also for GWs emitted by binary black holes, even if the localization volumes are usually much larger than for binary neutron stars. In this case ~ 500 events are needed to reach a precision $< 7\%$ on H_0 [37, 51].

This independent estimation of H_0, one of the key parameters of the currently adopted standard model of cosmology ΛCDM, can play a fundamental role in this field. Indeed, great effort has been put into its estimation, because of the discrepancy in the H_0 values estimated from the early and late-time Universe. The ΛCDM model calibrated with data from the *Planck* mission, that is, from early-Universe physics, predicts the Hubble constant to 1% precision: 67.4 ± 0.5 km/s/Mpc [179] (medians and 68% credible intervals). However, if H_0 is measured locally ($z < 1$), so in the late-time Universe, such as the SHoES measurements (Supernovae H_0 for the Equation of State, [192]) and HoliCOW (H_0 lenses in COSMOGRAIL's Wellspring, [247]), a larger values of H_0 is favoured: 74.0 ± 1.4 km/s/Mpc and 73.3 ± 1.8 km/s/Mpc, respectively. Thus, the early-Universe data seem to be consistently predicting a low value of H_0, while the late-time Universe data a higher one, leading to a more than 3σ discrepancy [see for an extensive discussion 231].

The standard sirens method offers a powerful way of solving this discrepancy. However, its main problem is the degeneracy between the luminosity distance and inclination estimated from GWs (see also Section 1.1.2). They are measured from the amplitude of the two GW polarizations. At small inclinations, the cross and plus polarizations have nearly the same amplitude, but the larger the inclination, the more they decrease and start to differ [230]. This means that the GW signal is strongest at small inclinations (face-on or face-off), but, in these cases, we cannot measure distance and inclination separately. Therefore, associated EM observations can lead to a tighter measurement of H_0 by providing additional constraints on the inclination.

The first measurement of H_0 using GWs was obtained with GW170817, by combining the distance from the GW signal and the recession velocity of the host galaxy NGC 4993, resulting in H_0 of 74^{+16}_{-8} km/s/Mpc [3]. The EM information on the inclination derived from the afterglow and the relativistic jet motion of GW170817 allow us to improve the Hubble constant measurement for the reason stated above [see also 43, for a review]. The common practice is to use the GW analysis results (posterior) for inclination and luminosity distance, and apply these as *a priori* information on the inclination obtained by fitting the EM data sets (or the other way around). This, as we saw in the previous Chapters, can be done using Bayesian analysis. The results retrieved in this way run from low values such as $H_0 = 66.2^{+4.4}_{-4.2}$ km/s/Mpc, from Dietrich et al. [62], who fit the kilonova emission and the jet centroid motion, and $H_0 = 69.5 \pm 4$ km/s/Mpc, from [236], who use the afterglow emission, to high values such as $H_0 = 75.5^{+11.6}_{-9.6}$ km/s/Mpc, by Guidorzi et al. [105], who fit the afterglow up to 40 days from the merger. Wang et al. [237] estimate $H_0 = 71.80^{+4.15}_{-4.07}$ km/s/Mpc, modelling the jet with hydrodynamic simulations, including also a sub-relativistic kilonova outflow. Palmese et al. [169] use the same model as Wang et al. [237], fitting the afterglow, but including *a priori* information on the Lorentz factor from the jet centroid motion. They find $H_0 = 75.46^{+5.34}_{-5.39}$ km/s/Mpc. Hotokezaka et al. [121] fit the afterglow and the jet centroid motion, finding $H_0 = 68.9^{+4.7}_{-4.6}$ km/s/Mpc. In general, the smaller is the viewing angle, the higher is the luminosity distance (because of their degeneracy), the lower is H_0.

At present, the aforementioned EM-informed H_0 measurements are a factor 2 more precise than the first standard-siren measurement for GW170817 that fitted GW data only [3]. For this reason, this method is very compelling. However, including a new data set (the EM one) in the GW analysis, brings with it also its potential systematics, that should be carefully addressed, to avoid a biased estimation of H_0. An open issue, as outlined in [158], is the sensitivity of EM-derived parameters, as the inclination, on the assumed jet structure. A related problem is the presence of deviations from the assumed model due to a possible flux excess at late times in the GW170817 afterglow light curve. In this Chapter, these issues are discussed. In particular, I estimate the Hubble constant exploiting the GW, the broad-band afterglow and the centroid motion of the relativistic jet of the GW170817 event. I compare these results with the ones obtained fitting only afterglow light curve and GW data. Moreover, is tested the sensitivity of the results on the jet structure and on the possible presence of an excess at late times in the afterglow light curve.

In Section 4.1 I introduce the jet centroid motion data set, briefly summarizing the method of the analysis in Section 4.2. In Section 4.3 I show the results both for the energetics, microphysics and geometry of the event, and for the Hubble constant. Finally in Section 4.4 I summarize the conclusions for this Chapter.

4.1 DATA

For this analysis, I use three GW170817 data sets and analyze them simultaneously. These are the broad-band afterglow emission, the centroid position of the jet as a function of time, and the GW strain timeseries.

Regarding the afterglow emission, the radio, optical and X-ray light curve is already presented in Chapter 3. In the case of GW170817, also the observations of the

motion of the jet are available. The latter are taken at 75, 206, 230 days in the radio band using VLBI (Very Long Baseline Interferometry) [93, 154], and at 8 days in the optical, using HST [155]. For this kind of observations, high precision astrometry is fundamental, as the motion of the jet is of the order of the milliarcsecond below 100 Mpc [198]. The positions of the jet (the centroid of the emission in the image) and their uncertainties are represented in the bottom panel of Fig. 28, as reported in Ghirlanda et al. [93], Mooley et al. [154], and Mooley, Anderson, and Lu [155], the jet moves with time in the direction of positive RAs. For the optical data point (at negative RAs) in the errors are included (added in quadrature) the two systematic uncertainty contributions to take into account the different reference frame of the optical and radio images [as in 155]. Also upper limits on the size of the source are available in [93, 154] (10 mas and 2.5 mas respectively), but are not included in the fit, as, from a preliminary analysis, the size of the source from the modelling is well below them in any case.

The GW data are already introduced in Chapter 3.

4.2 JOINT ANALYSIS OF ELECTROMAGNETIC AND GRAVITATIONAL-WAVE DATA

The method used in this Chapter is the same as the previous one, a joint fit through Bayesian analysis. However, in this case, also the luminosity distance is a free fit parameter. The shared parameters are now the viewing angle and the luminosity distance. We will see the results of three fits, one including only GWs, one folding GWs and the afterglow light curve (GW+AG), and one including also the jet centroid motion data set (GW+AG+C). The GW and EM models are already explained in the previous Chapter, so, in this Section, I will focus mainly on the centroid modelling.

4.2.1 *Electromagnetic and gravitational-wave models*

Also in this case, the broad-band afterglow light curve is modelled using the PYTHON package AFTERGLOWPY [197]. The observer frame flux of synchrotron radiation is estimated for various jet geometries. In this work I use a Gaussian structured jet model, see eq.(6), but also a power law jet model, see eq.(7). In the latter case, all the parameters are fitted, including the power law index b (with a uniform prior in [1, 12]). The electrons are shock-accelerated and emit synchrotron radiation, for the complete set of fit parameters see Section 3.1.1. The viewing angle θ_v, between the jet axis and the line of sight, and the luminosity distance d_L are free parameters.

The latest version of AFTERGLOWPY [67, 198] allows to model also the jet centroid motion, estimating the afterglow image centroid position and sizes. The imaging plane is perpendicular to the line of sight of the observer, and the centroid position and sizes are computed as an intensity-weighted quantity. The outputs of the model that are used in this work are the centroid position in the sky (RA and Dec) and the flux expected at each particular time. At 8 days, in the optical, only the kilonova emission is visible, and not the afterglow. For this reason, we place a 5σ upper limit for the optical flux of 4×10^{-5} mJy. The parameters are the same as above, with an extra three parameters: RA_0, Dec_0, which represent the jet origin

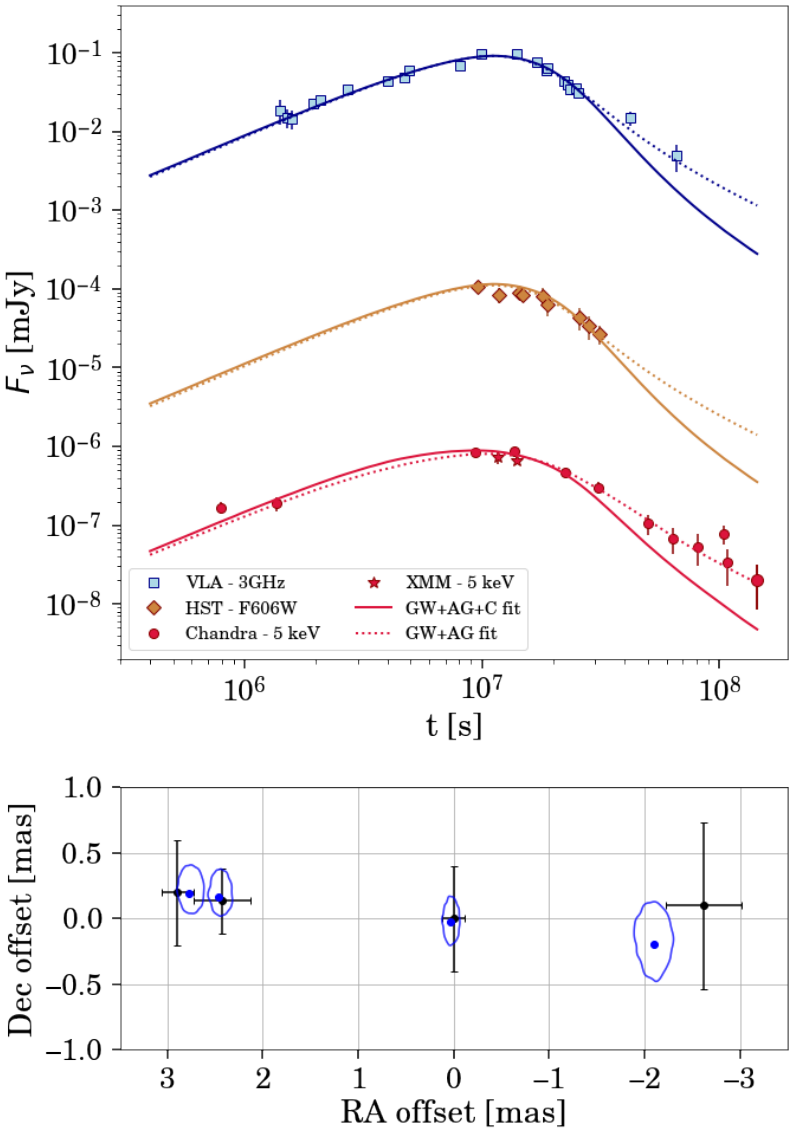

Figure 28: Top panel. Broad-band afterglow of GW170817: data and fits. From bottom to top, red points refer to the X-ray observations by *Chandra* and *XMM* at 5 keV, orange ones to observations by *HST*, F606W filter, in the optical band, and blue ones to observations in the radio band from VLA (Very Large Array) at 3 GHz. The continuous and dotted lines represent the fit of the GW, broad-band afterglow, and centroid motion (GW+AG+C) data and of the GW and afterglow (GW+AG) data, respectively. For sake of simplicity, the fit for the radio band is plotted only for the observations at 3 GHz, but it is not limited to this single frequency. Bottom panel. Centroid motion of the relativistic jet from HST and VLBI images at 8 (negative RAs), 75, 206 and 230 days [93, 154]. The blue dots represents the positions predicted by the model, the blue contours represent the 68% probability region.

Table 5: Prior probability distributions for the shared, the EM and GW fitted parameters.

Parameter	Prior functional form	Bounds
d_L [Mpc]	$\propto d_L^2$	[1, 75]
θ_v [deg]	$\sin(\theta_v)$	[0, 90]
$\log_{10} E_0/\mathrm{erg}$	Uniform	[49, 56]
θ_c [deg]	Uniform	[0, 90]
θ_W [deg]	Uniform	[0, 90]
$\log_{10} n_0$	Uniform	[-7, 2]
p	Uniform	[2, 3]
$\log_{10} \epsilon_e$	Uniform	[-5, 0]
$\log_{10} \epsilon_B$	Uniform	[-5, 0]
b	Uniform	[1, 12]
RA_0 [mas]	Uniform	[-10, 10]
Dec_0 [mas]	Uniform	[-10, 10]
PA [deg]	Uniform	[0, 360)
$\mathcal{M}[M_\odot]$	Uniform	[1.18, 1.21]
q	Uniform	[0.125, 1]
a_1	Uniform	[0, 0.05]
a_2	Uniform	[0, 0.05]
θ_1 [deg]	$\sin(\theta_1)$	[0, 180]
θ_2 [deg]	$\sin(\theta_2)$	[0, 180]
$\phi_{1,2}$ [deg]	Uniform	[0, 360]
ϕ_{JL} [deg]	Uniform	[0, 360]
ψ [deg]	Uniform	[0, 180]
Λ_1	Uniform	[0, 5000]
Λ_2	Uniform	[0, 5000]

in the sky image, and the position angle PA, which is the orientation of the jet direction in the image.

The prior probability distributions are reported in Table 5. The prior for the viewing angle θ_v is isotropic, meaning a sinusoidal distribution from $0\mathrm{deg}$ to $90\mathrm{deg}$. For the luminosity distance, we use a uniform-in-volume prior ($\propto d_L^2$) from 1 to 75 Mpc, which distributes mergers uniformly throughout a Euclidean universe.

The GW model is already introduced in the previous Chapter, I note here that the sky-position (RA and Dec) of the source is still fixed to the one of AT 2017gfo [6]. The GW RA and Dec correspond to the RA_0, Dec_0 parameters of the centroid motion model, however, the precision on RA and Dec from the GW data does not reach the mas level, as instead do RA_0 and Dec_0, so the analysis does not benefit from promoting the RA and Dec of the GW and the EM models to common, free parameters. The total number of parameters, including the luminosity distance d_L is 23, when addressing the GW and EM domains.

The priors for the intrinsic and extrinsic GW parameters are set as in Romero-Shaw et al. [194] (same as the previous Chapter), in the case of the "Low Spin" analysis, see Table 5.

4.2.2 *Joint fit*

The EM and GW likelihoods are both Normal distributions, as already introduced in Section 3.2.1. We will call the fit with joint afterglow light curve and GW as GW+AG, while the one joining all three datasets (GW strain, afterglow light curve and centroid motion) as GW+AG+C. In the case of the fit of the GW+AG+C, we assume the afterglow and the centroid motion data sets to be independent, being taken with different telescopes and at different times. The centroid data set includes the positions (RA and Dec) at each time and their respective fluxes, we take the data point at 8 days as the position of the merger. We assume the likelihood function to be a multivariate Normal distribution, where the expected centroid positions and fluxes from the model are compared with the four offset positions (RA and Dec) and the corresponding flux measurements. Moreover, we assume the covariance matrix to be diagonal (see [198] for more details). We place the centre of the centroid motion reference system at the positions corresponding to the observations at 75 days, as in Ghirlanda et al. [93], Mooley et al. [154], and Mooley, Anderson, and Lu [155].

4.2.3 *Hubble constant estimation*

At small redshifts, as in the GW170817 case, the luminosity distance does not depend on the cosmological model, so the Hubble constant can estimated from

$$v_H = H_0 \cdot d_L \,, \tag{59}$$

where v_H is the local "Hubble flow" velocity, in this case at the position of GW170817, and d_L is the luminosity distance to the source. I follow the same procedure as Abbott et al. [3], assuming a Normal distribution for $v_H = 3017 \pm 166$ km/s.

4.3 RESULTS AND DISCUSSION

The jet profile is assumed to be Gaussian throughout this Chapter, with the exception of Sec. 4.3.2, where a power law profile is assumed in order to test the sensitivity of the results on the jet model.

Table 6: Fit results for GW170817 for a Gaussian (GJ) and a power law jet (PLJ). I report the medians and the 16th-84th percentiles. In the second column I report the results for the GW-only fit, in the third and fifth columns the results of the fit of the broad-band afterglow and the GW, in the fourth and sixth columns the results of the joint fit of broad-band afterglow, centroid motion and GW. The two last columns provide the results of the GW+AG+C fit with a constant component of the type $F_{\nu,c} = 10^c$ modelling the late time emission.

Parameter	GW-only	GW+AG	GW+AG+C	GW+AG	GW+AG+C	GW+AG	GW+AG+C
		GJ	GJ	PLJ	PLJ	GJ + Constant	GJ + Constant
$\log_{10} E_0$		$52.31^{+0.82}_{-0.80}$	$54.50^{+0.28}_{-0.33}$	$52.12^{+0.78}_{-0.85}$	$54.0^{+0.30}_{-0.32}$	$52.81^{+0.90}_{-0.86}$	$54.81^{+0.30}_{-0.35}$
θ_c [deg]		$7.73^{+0.86}_{-0.80}$	$2.85^{+0.24}_{-0.20}$	$5.57^{+0.69}_{-0.62}$	$2.18^{+0.20}_{-0.16}$	$5.37^{+0.97}_{-0.87}$	$2.64^{+0.20}_{-0.18}$
θ_W [deg]		57^{+19}_{-19}	52^{+23}_{-23}	58^{+18}_{-18}	50^{+23}_{-25}	52^{+22}_{-21}	52^{+23}_{-23}
$\log_{10} n_0$		$-0.68^{+0.80}_{-0.80}$	$-1.93^{+0.34}_{-0.39}$	$-0.37^{+0.77}_{-0.84}$	$-2.40^{+0.40}_{-0.35}$	$-1.39^{+0.89}_{-0.89}$	$-1.86^{+0.35}_{-0.39}$
p		$2.11^{+0.01}_{-0.01}$	$2.11^{+0.01}_{-0.01}$	$2.12^{+0.01}_{-0.01}$	$2.12^{+0.01}_{-0.01}$	$2.12^{+0.01}_{-0.01}$	$2.12^{+0.01}_{-0.01}$
$\log_{10} \epsilon_e$		$-1.65^{+0.71}_{-0.73}$	$-3.45^{+0.28}_{-0.24}$	$-1.34^{+0.74}_{-0.69}$	$-2.72^{+0.30}_{-0.25}$	$-1.89^{+0.76}_{-0.79}$	$-3.64^{+0.30}_{-0.24}$
$\log_{10} \epsilon_B$		$-3.78^{+0.80}_{-0.80}$	$-3.89^{+0.34}_{-0.29}$	$-3.83^{+0.82}_{-0.77}$	$-3.43^{+0.35}_{-0.28}$	$-3.63^{+0.85}_{-0.88}$	$-4.06^{+0.37}_{-0.32}$
b				$7.5^{+1.6}_{-1.1}$	$10.8^{+0.7}_{-1.0}$		
c_{radio}						$-2.99^{+0.23}_{-0.20}$	$-2.88^{+0.24}_{-0.26}$
c_{optical}						$-5.25^{+0.23}_{-0.22}$	$-5.24^{+0.24}_{-0.23}$
$c_{\text{X-rays}}$						$-7.48^{+0.05}_{-0.03}$	$-7.47^{+0.08}_{-0.10}$
RA_0 [mas]			$-2.1^{+0.2}_{-0.2}$		$-2.0^{+0.2}_{-0.2}$		$-2.2^{+0.2}_{-0.2}$
Dec_0 [mas]			$-0.2^{+0.3}_{-0.3}$		$-0.2^{+0.3}_{-0.3}$		$-0.2^{+0.3}_{-0.3}$
PA [deg]			85^{+4}_{-3}		85^{+4}_{-3}		85^{+5}_{-3}
d_L [Mpc]	$39.2^{+5.4}_{-8.6}$	$31.3^{+3.0}_{-3.6}$	$43.7^{+1.4}_{-1.4}$	$23.7^{+3.8}_{-3.4}$	$43.0^{+1.4}_{-1.4}$	$38.6^{+2.5}_{-3.0}$	$44.3^{+1.4}_{-1.3}$
θ_v [deg]		$50.1^{+5.1}_{-5.4}$	$18.2^{+1.2}_{-1.5}$	$62.7^{+5.0}_{-4.3}$	$19.8^{+1.3}_{-1.8}$	$35.2^{+5.7}_{-6.2}$	$17.2^{+1.1}_{-1.2}$

θ_{JN} [deg]	146^{+16}_{-18}	$129.9^{+5.1}_{-5.4}$	$161.8^{+1.2}_{-1.5}$	$117.3^{+5.0}_{-4.3}$	$160.2^{+1.3}_{-1.8}$	$144.8^{+5.7}_{-6.2}$	$162.8^{+1.1}_{-1.2}$
$\mathcal{M}[M_\odot]$	$1.1975^{+0.0001}_{-0.0001}$	$1.1975^{+0.0001}_{-0.0001}$	$1.1975^{+0.0001}_{-0.0001}$	$1.1975^{+0.0001}_{-0.0001}$	$1.1975^{+0.0001}_{-0.0001}$	$1.1975^{+0.0001}_{-0.0001}$	$1.1975^{+0.0001}_{-0.0001}$
q	$0.88^{+0.08}_{-0.10}$	$0.87^{+0.08}_{-0.09}$	$0.88^{+0.08}_{-0.09}$	$0.88^{+0.8}_{-0.9}$	$0.89^{+0.07}_{-0.08}$	$0.87^{+0.08}_{-0.09}$	$0.87^{+0.08}_{-0.09}$
a_1	$0.02^{+0.02}_{-0.01}$	$0.02^{+0.02}_{-0.01}$	$0.02^{+0.02}_{-0.01}$	$0.02^{+0.02}_{-0.01}$	$0.02^{+0.02}_{-0.01}$	$0.02^{+0.02}_{-0.01}$	$0.02^{+0.02}_{-0.01}$
a_2	$0.02^{+0.02}_{-0.01}$	$0.02^{+0.02}_{-0.01}$	$0.02^{+0.02}_{-0.01}$	$0.02^{+0.02}_{-0.01}$	$0.02^{+0.01}_{-0.02}$	$0.02^{+0.02}_{-0.02}$	$0.02^{+0.02}_{-0.01}$
θ_1 [deg]	81^{+34}_{-34}	81^{+32}_{-34}	82^{+33}_{-34}	83^{+33}_{-33}	74^{+31}_{-30}	79^{+34}_{-32}	80^{+33}_{-32}
θ_2 [deg]	84^{+36}_{-36}	82^{+35}_{-34}	84^{+34}_{-35}	81^{+34}_{-34}	95^{+34}_{-31}	82^{+34}_{-36}	85^{+37}_{-36}
$\phi_{1,2}$ [deg]	174^{+126}_{-121}	177^{+122}_{-121}	181^{+117}_{-121}	178^{+118}_{-120}	177^{+125}_{-118}	178^{+117}_{-119}	176^{+120}_{-118}
ϕ_{JL} [deg]	178^{+122}_{-122}	174^{+124}_{-119}	179^{+120}_{-125}	176^{+122}_{-120}	180^{+119}_{-120}	6177^{+120}_{-121}	175^{+120}_{-116}
ψ [deg]	88^{+61}_{-68}	88^{+53}_{-73}	89^{+62}_{-60}	68^{+43}_{-60}	89^{+62}_{-61}	90^{+61}_{-65}	89^{+61}_{-61}
Λ_1	250^{+355}_{-172}	274^{+385}_{-187}	270^{+350}_{-184}	280^{+356}_{-193}	309^{+335}_{-201}	268^{+333}_{-179}	269^{+336}_{-183}
Λ_2	423^{+547}_{-289}	425^{+534}_{-292}	422^{+513}_{-287}	452^{+533}_{-307}	448^{+498}_{-300}	447^{+537}_{-305}	429^{+532}_{-294}

The parameter medians and 16th-84th percentiles are collected in Table 6. The second column reports the results of the GW-only fit, while the third and fourth column refer to the fit including the broad-band afterglow and GW (GW+AG), and to the complete fit that also includes the centroid (GW+AG+C), respectively.

The results from the GW fit are in agreement with previous works [3, 7, 194], the H_0 value from the GW-only fit is $H_0 = 77^{+21}_{-10}$ km/s/Mpc (median, 16th-84th percentiles), see Fig. 29, bottom panel, and Fig. 30. As we already pointed out above, one of the main sources of uncertainty in the GW measurement of the inclination and of the distance (and H_0) is due to their degeneracy, see the light blue contours in Fig. 29, top panel. This means that it is hard to distinguish whether a source is further away with the binary orbit facing Earth (face-on or face-off), or closer but highly inclined (edge-on, [230]). If we assume to have inclinations from 0 to 90 deg (like in our case), d_L is a decreasing function of the inclination (viewing angle, θ_v). Another independent messenger is needed to break this degeneracy, which, in this case, comes from the afterglow.

The afterglow light curve alone, however, is not enough to efficiently break this degeneracy. Including it in the fit, only helps in shrinking the degeneracy region, see green filled contours in Fig. 29, top panel, the uncertainty on the viewing angle is reduced by a factor ~ 3 (from $\theta_{JN} = 146^{+16}_{-18}$deg to $129.9^{+5.1}_{-5.4}$deg), the one on the distance by a factor ~ 2 (from $d_L = 39.2^{+5.4}_{-8.6}$ Mpc to $31.3^{+3.0}_{-3.6}$ Mpc). However, this is not an accurate measurement, in fact the medians are on the high-θ_v–low-d_L end of the GW 1σ region, leading to quite a low distance (and large viewing angle, $\theta_v = 50.1^{+5.1}_{-5.4}$deg), which is however within 3σ from the generally accepted value of ~ 40 Mpc. The H_0 value from the GW+AG fit is quite high: we have $H_0 = 96^{+13}_{-10}$ km/s/Mpc (median, 16th-84th percentiles), see the green filled contours in Fig. 29, bottom panel, and Fig. 30, top panel.

As explained in more details in Sections 4.3.1 and 4.3.3, this result is mostly driven by the possible presence of a late time additional component, which can be seen in the top panel of Fig. 28. The GW+AG model (dotted line) fits very well the light curve, especially the data points at late time. The latter force the model to prefer a high θ_v with respect to the fit including also the jet centroid motion, GW+AG+C, represented with a solid line. Indeed, Wang and Giannios [236], using the same messengers but limiting the light curve data up to $\sim$ 300 days (when no flux deviation is present yet), retrieve $H_0 = 69.5 \pm 4$ km/s/Mpc, with a $d_L = 43.4 \pm 1$ Mpc and $\theta_v = 22 \pm 1$ deg. The jet structure model they use is from 3-dimensional general-relativistic megnetohydrodynamical simulations. Also Wang et al. [237] fit the afterglow light curve and include an additional component at late times, a sub-relativistic kilonova outflow. They estimate $H_0 = 71.80^{+4.15}_{-4.07}$ km/s/Mpc. The kilonova component helps in the fit of the light curve, keeping the viewing angle around 30 deg. Also in this case, they model the jet using hydrodynamic simulations. Guidorzi et al. [105] get $H_0 = 75.5^{+11.6}_{-9.6}$ km/s/Mpc, assuming a Top Hat jet and fitting the afterglow data up to 40 days from the merger. The latter is the reason why the H_0 uncertainties are larger with respect to more recent works, their θ_v posterior distribution peaks at $\sim$30 deg. However, the Top Hat jet is not the best choice for GW170817 light curve, as it cannot reproduce the slope before the peak.

In Section 4.3.3 the possible late time excess in the GW+AG fit is accounted for with a constant flux component. In this case, the results are in agreement with the

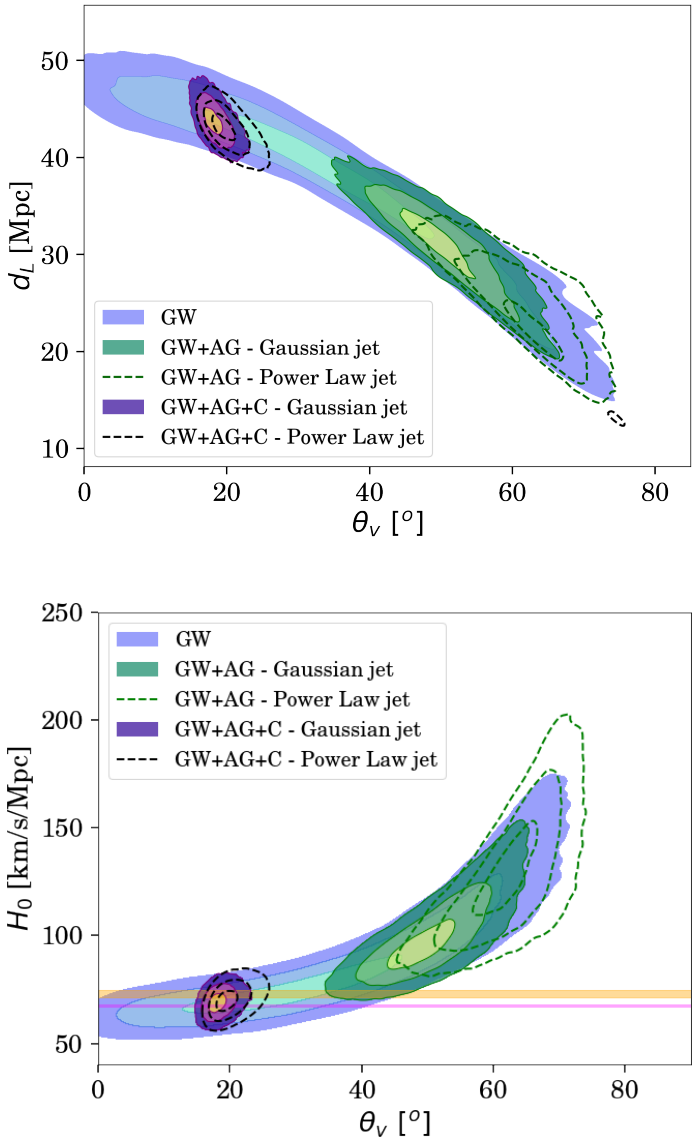

Figure 29: Top panel. Contour plot of the viewing angle and luminosity distance for the GW, GW+AG and GW+AG+C fits. The contours represent the 68%, 95%, 99.7% probability regions. Bottom panel. The same contour plot as above, but switching to H_0, instead of d_L. The magenta and yellow regions represent the 1 σ of the *Planck* and SHoES measurements respectively. The Gaussian jet results are represented with filled contours, while the power law jet with empty contours and dashed lines.

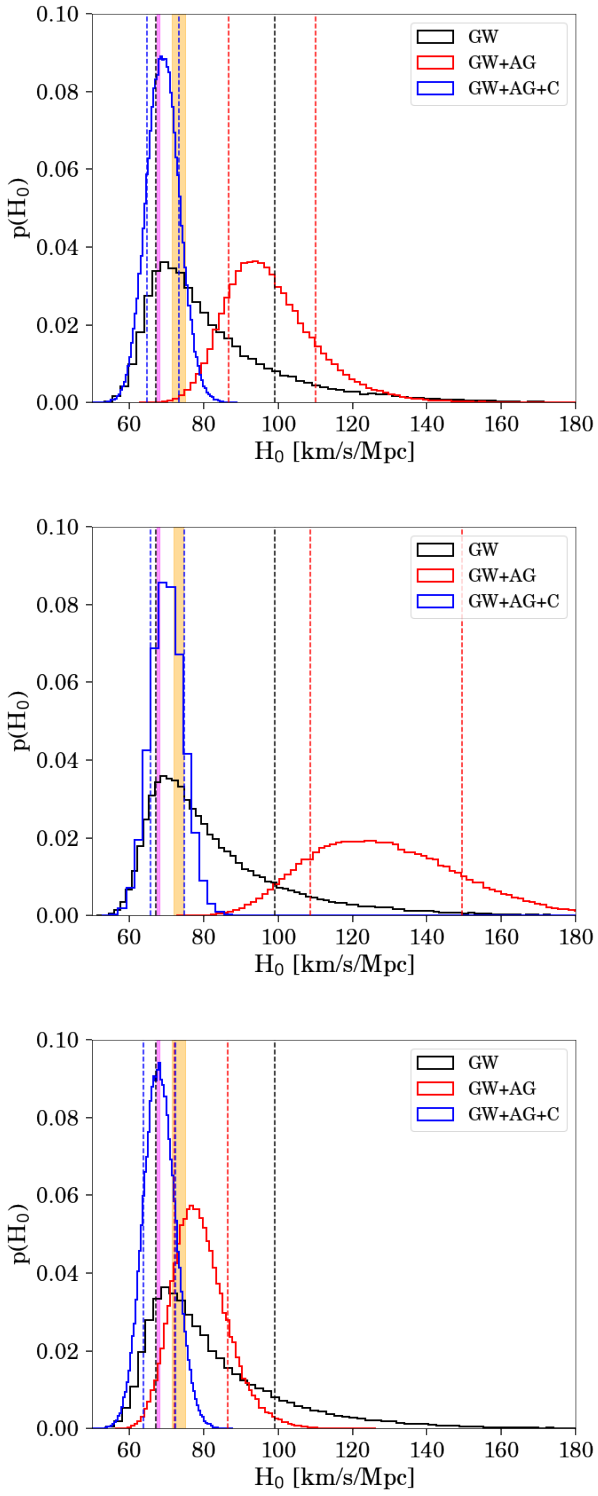

Figure 30: Histograms of the Hubble constant H_0 posterior from the GW-only fit, in black, the GW+AG in red and the GW+AG+C in blue. The vertical dashed lines represent the 16th and 84th percentiles of each distribution. The magenta and yellow shaded regions represent the 1σ interval of the *Planck* and SH0ES measurements respectively. Top panel: Gaussian jet. Central panel: power law jet. Bottom panel: Gaussian jet with the addition of a constant component at late times.

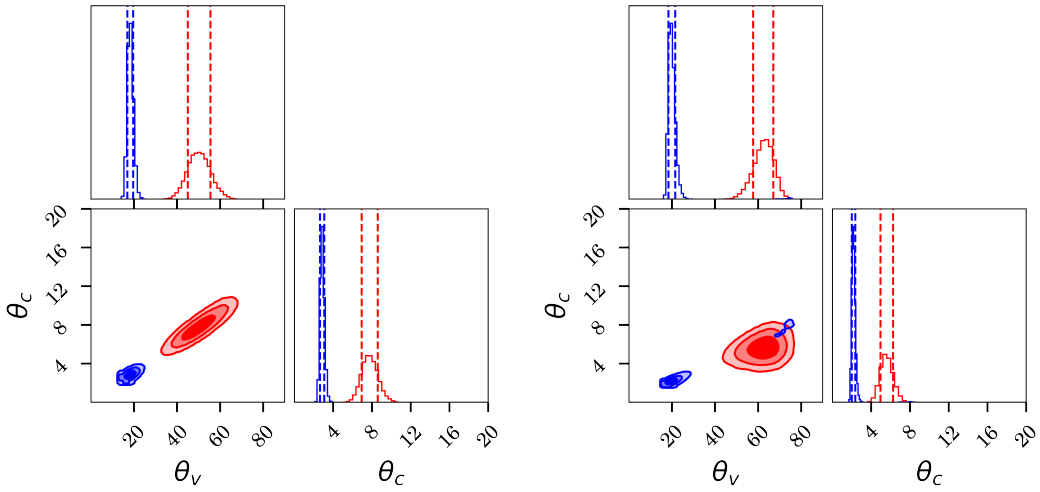

Figure 31: Contour plots of the viewing angle and jet opening angle. The contours represent the 68%, 95%, 99.7% probabilities. The blue contour lines represent the result from the joint GW+AG+C fit, while the red ones represent the result from the GW+AG fit. Left panel: Gaussian jet. Right panel: power law jet.

aforementioned works, see the complete analysis in Section 4.3.3. It is also interesting to note that the similar results of these works are obtained using different jet structures. We will come back to this point and explore how H_0 changes depending on the jet structure in Section 4.3.2.

From these results, we find that limiting the analysis to GW+AG domains could be subject to possible systematics in the H_0 determination due to the detections at late times in the afterglow light curve. This adds up to the degeneracy between θ_v and θ_c, proper of a Gaussian modelling of the jet, that is evident in the left panel of Fig. 31. Here the marginalised, 2D posterior probability distributions for the jet opening angle θ_c and the viewing angle θ_v are shown in the cases of the the joint GW+AG fit (in red contours).

For the reasons stated above, in order to break both the $d_L - \theta_v$ GW degeneracy and the $\theta_v - \theta_c$ EM one, we have to include not only the afterglow light curve, but also the centroid motion in the analysis. It should be noted that the sole centroid motion is not enough to break the $d_L - \theta_v$ degeneracy, being itself subjected to some level of degeneracy between these two parameters, see Section 4.3.4 for a more detailed discussion.

The results for the GW+AG+C fit, using both the afterglow and the centroid, are written in Table 6, fourth column. This fit not only shifts the viewing angle to lower values, but also shrinks further the degeneracy between θ_v and θ_c, see left panel of Fig. 31, blue contours. This happens because the relativistic jet motion strongly constrain the viewing angle. In Fig. 28, bottom panel, the jet positions are well reconstructed by the model, within 1σ, while in top panel, we see that the GW+AG+C model does not fit well the late time light curve, especially in the X-rays and in the radio bands, unlike the GW+AG fit, recognising it as a possible excess not due to the afterglow emission. We can account for this adding a constant flux component at late times. The latter helps in fitting that part of the light curve, but results in very similar posteriors to the GW+AG+C fit without it (see the full results in Section 4.3.3). This shows that, adding the afterglow centroid motion

in the analysis, provides robustness to the fit. The discrepancy in the fit of the light curve at late time when including the jet centroid motion is due to the fits preference for two different viewing angles and types of jet: the GW+AG fit prefers a large θ_v, a broader jet profile and less energy on the jet axis, while the GW+AG+C fit prefers a small θ_v, a highly collimated jet with a large energy on the jet axis and a less dense circumburst medium. We go into detail of this differences in Sec. 4.3.1.

The θ_v and d_L posteriors of the GW+AG+C fit are in the low-θ_v–high-d_L GW 1σ region of the degeneracy, predicting a distance of $43.7^{+1.4}_{-1.4}$ Mpc and a viewing angle of $18.2^{+1.2}_{-1.5}$ deg. The centroid addition in the fit helps in shrinking the uncertainties in these parameters, which are smaller by a factor of 4-5 for the distance and 8-9 for θ_v with respect to the GW analysis, breaking their degeneracy, see the purple and yellow filled contours in the top panel of Fig. 29. From the GW+AG+C fit we obtain $H_0 = 69.0^{+4.4}_{-4.3}$ km/s/Mpc (median, 16th-84th percentiles). It is to be noted that, adding the centroid in the analysis, brings to an about three times more precise H_0 measurement than the GW-only standard-siren measurement. The *Planck* estimate of 67.4 ± 0.5 km/s/Mpc [179] and the SHoES value of 74.0 ± 1.4 km/s/Mpc [192], are both within 1σ, see Fig. 29, bottom panel, and Fig. 30, top panel. This result is in agreement also with other works, like Hotokezaka et al. [121], who use the posteriors from GW, and fit the afterglow flux and the centroid motion, finding $H_0 = 68.9^{+4.7}_{-4.6}$ km/s/Mpc. Palmese et al. [169] use the same model as Wang et al. [237] (hydrodynamic simulations), and use a prior on the jet break Lorentz factor from the centroid measurements, which acts also on the jet opening angle and on the viewing angle. They find $H_0 = 75.46^{+5.34}_{-5.39}$ km/s/Mpc. Leaving the Lorentz factor free leads to an opening angle of around 7 deg, which is instead consistent with our GW+AG results for θ_c.

In this analysis, the values of θ_v and θ_c from the GW+AG+C fit are in agreement with other works that included the centroid motion in their analysis. Ghirlanda et al. [93] predicts $\theta_c = 3.1 \pm 1$ deg, with a viewing angle of about 15 deg, Mooley et al. [154] and Mooley, Anderson, and Lu [155] an opening angle of < 5 deg, and a viewing angle < 24 deg, while Ren et al. [189] find $\theta_c = 3.1$ deg and $\theta_v = 17.4$ deg.

4.3.1 *About the difference between GW+AG and GW+AG+C fits*

The GW+AG and GW+AG+C produce quite different results, not only regarding the Hubble constant, the luminosity distance and the viewing angle, but also the energetics and microphysics of the jet. Indeed, while the GW+AG fit results in a large θ_v, a broader jet profile and less energy on the jet axis, the GW+AG+C fit results in a small θ_v, a highly collimated jet with a large energy on the jet axis and a less dense circumburst medium. The viewing angle values are about 5σ away, which is quite singular, considering that the event is the same. This, as we stated above, is due to the light curve data points at late times, which are well captured by the GW+AG fit, but not by the GW+AG+C fit, see Fig. 28. In particular, when including the afterglow centroid motion in the fit, the latter prevails over the light curve data points at late times, resulting in a low viewing angle and a fit of the light curve that, at late times, shows deviations from the flux observations.

In the GW+AG+C, the centroid motion is able to constrain very well θ_v to $18.2^{+1.2}_{-1.5}$ deg, which then translates into a constraint also on $\theta_c = 2.85^{+0.24}_{-0.20}$ deg.

This happens because of the degeneracy between the two angles, proper of the Gaussian jet light curve (see Fig. 31). In fact, its rising slope depends on their ratio, which, in this fit, is about 6.4. In the GW+AG, instead, there are no constraints on θ_v or θ_c individually, but just on their ratio, from the rising slope of the light curve [see also 158, 197]. This still leads to the same ratio of about 6.5, but $\theta_v = 50.1^{+5.1}_{-5.4}$ deg and $\theta_c = 7.73^{+0.86}_{-0.80}$ deg, about 5 sigma away from the GW+AG+C case.

The GW+AG fit, not being constrained by the centroid data set, is free to account for the mild decay of the light curve at late times by anticipating the non-relativistic phase. In particular, the non-relativistic time ([197] and Section 1.2.3) is $t_{NR} = 880^{+290}_{-210}$ days (GW+AG), with respect to $t_{NR} = 13000^{+2700}_{-2400}$ days (GW+AG+C). Therefore, at late times, according to the parameters of the GW+AG fit, the jet is non-relativistic. The anticipation of the relativistic phase is obtained mainly by acting on the E_0, n_0 parameters. However, the one order of magnitude lower energy and two orders of magnitude higher circumburst density would shift the flux at low values and the break at earlier times, since $t_b \propto (E_0/n_0)^{1/3}(\theta_v + 1.24\theta_c)^{8/3}$ [197]. This is balanced by the fit with higher values of θ_c and θ_v, in order to bring back the jet break (the peak) at about 130 days, and to adjust the rising slope of the light curve. This influences also the early decreasing slope (before the non-relativistic phase), as a higher θ_c (wider jet) provides a larger surface area, so the jet is brighter and the flux is higher. The parameters d_L, ϵ_e, ϵ_B have mainly the role of shifting the flux. ϵ_e and ϵ_B also controls the positions of the synchrotron spectrum frequencies ν_c and ν_m: the increase in E_0 of the GW+AG+C fit has to be followed by a decrease in these two parameters (see eq.(22)), since the spectral shape is very well constrained. Moreover, the low values of ϵ_e and ϵ_B (especially for the GW+AG+C fit, in agreement with [198] who use the same model), are probably due to the high value of $E_0 \sim 10^{54.5}$ erg, indicating that, with such high energy, its fraction in the accelerated electrons and magnetic field can be low, and still give a good light curve fit. The p parameter stays the same in the two fits, as it is constrained by the spectrum. θ_W is unconstrained in both fits, however it is better constrained in the GW+AG fit, mainly because θ_c is larger, and, being a Gaussian jet, θ_w has to be lower than θ_c.

In other words, the good fit in the GW+AG case is provided by a combined effect of the high θ_c (in the decreasing slope right after the peak) and the anticipation of the non-relativistic phase (in the slope at late times).

4.3.2 *Changing the structure of the jet*

In the case of a power law jet, the degeneracy between θ_v and θ_c is not as strong as for the Gaussian geometry, the rising phase slope is a function of b, θ_v and θ_c (see Eq.(33) of [197]). This can be seen in the right panel of Fig. 31, where the GW+AG fit is represented in red contours. The GW+AG and GW+AG+C are written in the fifth and sixth column of Table 6, while the fits of the afterglow light curve and centroid motion are in Fig. 32. Also for this jet structure, the GW+AG and GW+AG+C produce quite different results, and the reasoning in Section 4.3.1 is still valid. The majority of the parameters from the GW+AG+C and GW+AG fits, assuming a power law model, are in agreement within 1σ with the Gaussian jet model, this is probably due to the fact that, at early times, the afterglow light curve rises, so b has to be large. At the same time, the larger is b, the more the Gaussian

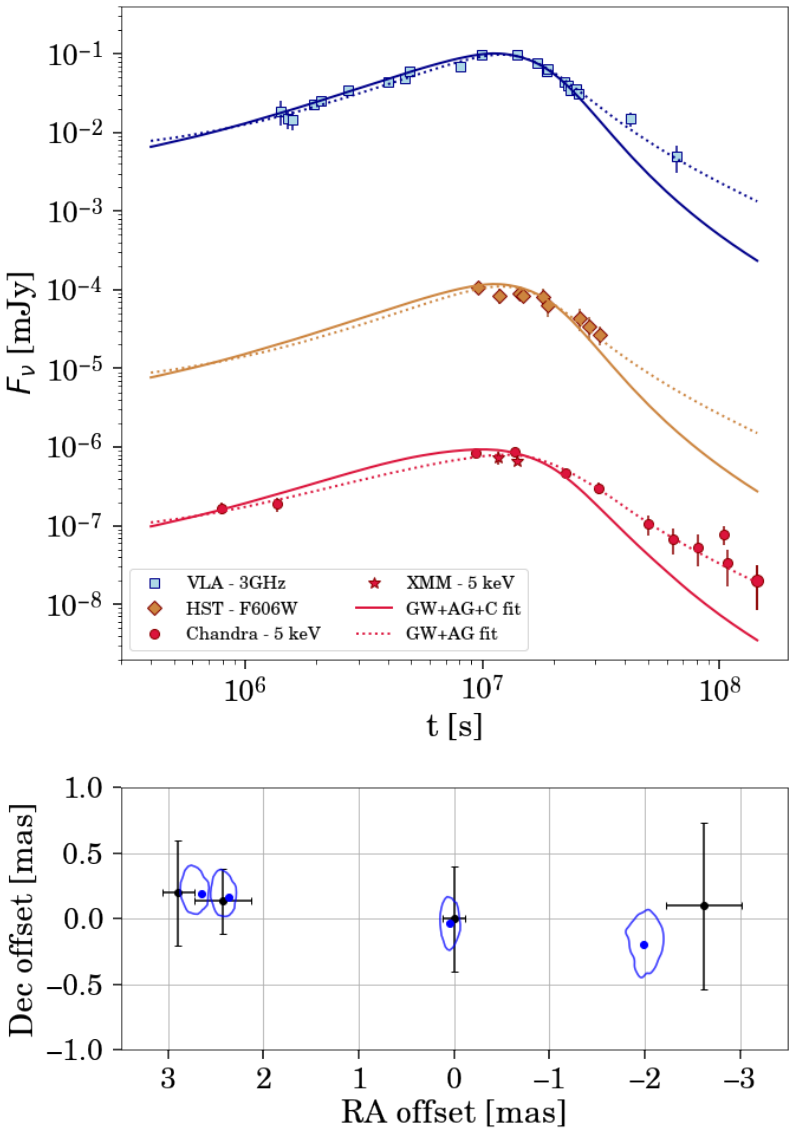

Figure 32: Same as Fig. 28, but assuming a power law structure for the jet.

and power law structures are similar. For example, in the case of the GW+AG+C fit, for $b = 10.8$, the $E(\theta)$ of a Gaussian and power law structures are very similar within $\sim 3\theta_c$, after which the decay is shallower for the power law structure.

The GW+AG fit produces a larger $\theta_v = 62.7^{+5.0}_{-4.3}$ deg, a smaller $\theta_c = 5.57^{+0.69}_{-0.62}$ deg and smaller $d_L = 23.7^{+3.8}_{-3.4}$ Mpc, than the Gaussian jet, these parameters are, however, in agreement within 2σ with the latter. The 2D posterior for θ_v and d_L are represented in Fig. 29, top panel, in green dashed contours. The microphysics and the energetics are in agreement within 1σ with the Gaussian jet results.

In the GW+AG+C fit, the parameters are in agreement within 1σ with the Gaussian jet model, except for $\theta_c = 2.18^{+0.20}_{-0.16}$ deg, which is within 2σ. The θ_v and θ_c 2D posteriors for the power law jet are represented in the right panel of Fig. 31, we can see that at 3σ there are samples with large viewing angles, usually preferred instead from the GW+AG fits. The results for θ_v is $19.8^{+1.3}_{-1.8}$ deg and for $d_L = 43.0^{+1.4}_{-1.4}$ Mpc. The 2D posterior distributions of θ_v and d_L are in Fig. 29, top panel, in black dashed contours, almost superimposed to the Gaussian jet results

(purple and yellow coloured contours). Also in this case there is a small region of the parameter space at 3σ at large θ_v and small d_L, which gets cancelled when estimating H_0, bottom panel.

The H_0 values retrieved in these fits are $70.2^{+4.6}_{-4.4}$ km/s/Mpc for the GW+AG+C fit, and 127^{+22}_{-19} km/s/Mpc (medians, 16th-84th percentiles) for the GW+AG fit, the H_0 posteriors are represented in the central panel of Fig. 30, in blue and red respectively. For this event, if we use the complete data set (the most robust fit), the change in jet model does not significantly influence H_0, the power law jet predicts an H_0 larger than 1.2 km/s/Mpc, which is a 2% difference, with respect to a Gaussian jet, but still in agreement within the uncertainties. In the GW+AG there is a 30% difference, but the two H_0s are compatible within 1σ.

In order to assess if the unknown jet structure leads to systematics in the estimation of H_0, I simulate an afterglow light curve and centroid movement using a Gaussian jet, which are then fitted twice, assuming a Gaussian and a power law structure. To keep this simulation as similar to GW170817 as possible, the simulated EM dataset is composed of the GW170817 detection times, errors and frequencies, with fluxes and positions predicted by the model, with a Gaussian variation. The EM data sets are simulated assuming a Gaussian jet and the parameters in Table 6, medians in the fourth column. In this way, we do not include the excess in the flux at late times, which we are not interested in, as we are focusing on the influence of the jet structure. These EM data sets are then fitted with GW two times, one assuming a Gaussian jet, and the other assuming a power law jet.

For both jet structures, the parameters of the GW, the energetics and microphysics are in agreeement within 1σ with the median values in Table 6, fourth column. Focusing on the distance and the geometry of the system, assuming a Gaussian jet, we have $\theta_v = 19.3^{+1.5}_{-1.7}$ deg, $\theta_c = 3.01^{+0.28}_{-0.25}$ deg and $d_L = 43.8^{+1.5}_{-1.7}$ Mpc, while for a power law jet $\theta_v = 20.2^{+1.6}_{-1.8}$ deg, $\theta_c = 2.40^{+0.24}_{-0.21}$ deg and $d_L = 43.6^{+1.5}_{-1.5}$ Mpc. As for the case of GW170817, the power law jet tends to give a slightly higher (lower) viewing angle (jet opening angle), which is in agreement within 2σ with the simulated values. This, however, does not influence much the luminosity distance. The H_0 posteriors retrieved from these fits are represented in Fig. 33, with purple (Gaussian jet fit) and green (power law jet fit) colors. It seems that the Hubble constant, as d_L, is not influenced by the different structure, resulting in $H_0 = 68.8^{+4.5}_{-4.4}$ km/s/Mpc for a Gaussian jet and $H_0 = 69.4^{+4.5}_{-4.4}$ km/s/Mpc for a power law jet (medians, 16th-84th percentiles). This is a less than 1% difference, which is well inside the 1σ range, nonetheless is also at the same level of the *Planck* uncertainty on H_0. For this reason, in the future, with a larger number of events, it could be important to assess if this, at the moment negligible difference, is just a statistical fluctuation or a real fluctuation due to the changing jet structure.

4.3.3 *Adding a constant component in the flux at late times*

In the case of GW170817, the high viewing angle preference mainly arise at late times, where there is a flux excess. This is either due to some missing emission at late times in the jet model itself, or due to a new component becoming visible, like a kilonova afterglow or the emission from a long-lived pulsar, in the former case we expect to see a rising flux in future observations, in the latter a constant flux [107, 177, 224]. If a flux additive component is included in the fit, indeed the

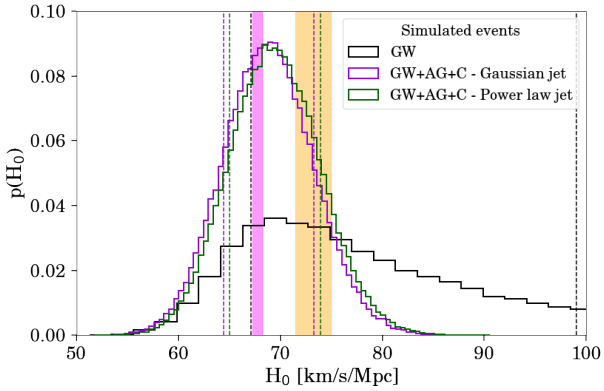

Figure 33: Histogram of the H_0 posterior distribution for a simulated event. The GW-only fit is represented in black (same distribution as Fig. 30), the GW+AG+C assuming a Gaussian jet in the fit is represented in violet, while the GW+AG+C assuming a power law jet is represented in green. The vertical dashed lines represent the 16th and 84th percentiles of each distribution. The magenta and yellow shaded regions represent the 1σ interval of the *Planck* and SH0ES measurements respectively.

jet viewing angle slightly decreases, see for example Balasubramanian et al. [21], Hajela et al. [108], Ryan et al. [198], Troja et al. [225], and Wang et al. [237].

I fit the same data set in Fig. 28, adding a constant flux component of the type $F_\nu = F_{\nu,agpy} + 10^c$, where $F_{\nu,agpy}$ is the flux predicted by AFTERGLOWPY and c is a parameter in the fit. This is done only at late times and at all frequencies. The c parameter has three possible values, depending on the frequency: c_{radio}, with a uniform prior in [-3.5,-2], $c_{optical}$ with a uniform prior in [-5.5, -4.5] and $c_{X\text{-rays}}$, with uniform prior in [-8, -7].

The results of the GW+AG+C and GW+AG fit are written in Table 6, last two columns, while the fit of the broad-band afterglow light curve and centroid motion are in Fig. 34.

This model can well fit the afterglow light curve and centroid motion, in both cases. The parameters values from the GW+AG+C fit are in agreement within 1σ with the ones from the simple Gaussian jet model (Table 6, fourth column). In the GW+AG+C the viewing angle $\theta_v = 17.2^{+1.1}_{-1.2}$ deg is lower with respect to the simple Gaussian jet model, so the distance $d_L = 44.3^{+1.4}_{-1.3}$ Mpc is slightly larger (see, for example, Fig. 35, top panel). The viewing angle and the jet opening angle are better constrained, but the error on the distance is unvaried with respect to the previous analysis. This fit leads to an H_0 of $68.0^{+4.4}_{-4.2}$ km/s/Mpc (see bottom panel of Fig. 30 and bottom panel of Fig. 35), which is in agreement with the value from the GW+AG+C fit with a simple Gaussian jet.

The inclusion of a constant component that accounts for the late-time behaviour does not significantly influence the parameter posteriors with respect to the model without it, so we can say that the GW+AG+C fit and model are robust.

In the case of the GW+AG fit, the addition of the constant component brings some improvements in the results. The jet parameters are compatible at most within 2σ with the GW+AG+C (with constant) fit, except for $\theta_c = 5.37^{+0.97}_{-0.87}$ deg and $\theta_v = 35.2^{+5.7}_{-6.2}$ deg, which are within 3σ. Thanks to the inclusion of the constant component at late times, the viewing angle decreases with respect to the

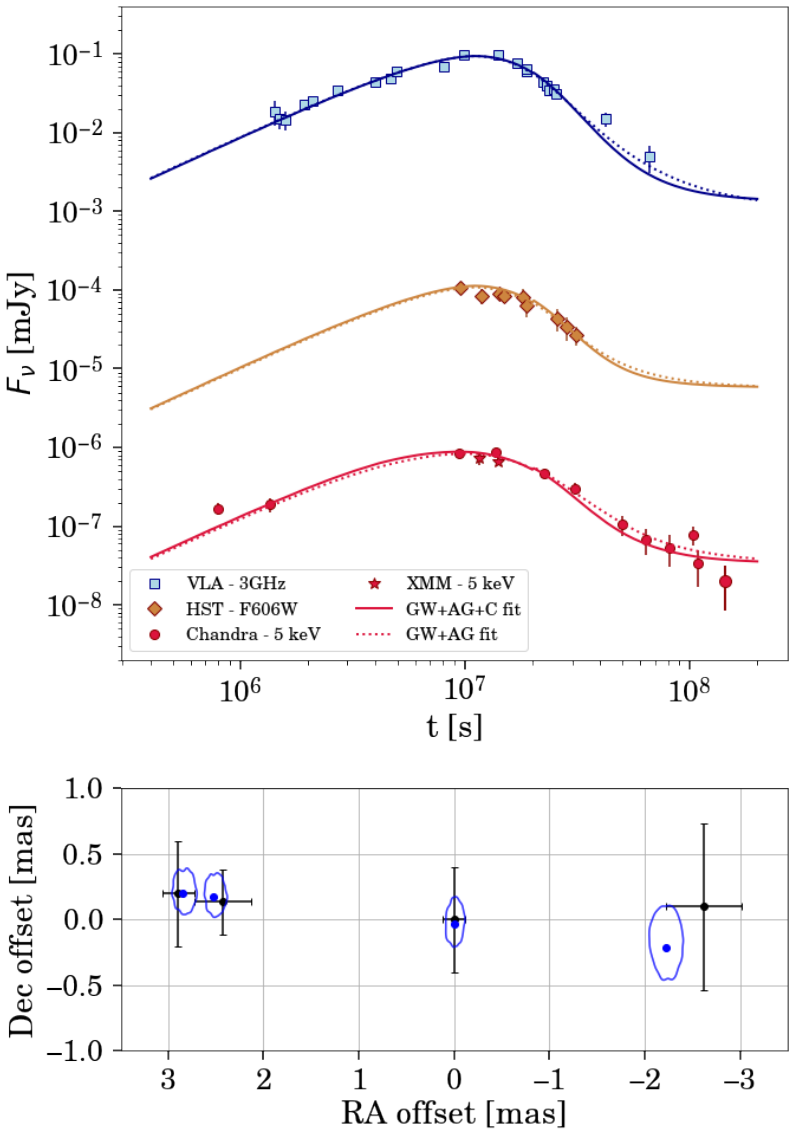

Figure 34: Same as Fig. 28, but including an additional constant flux component in the model at late times.

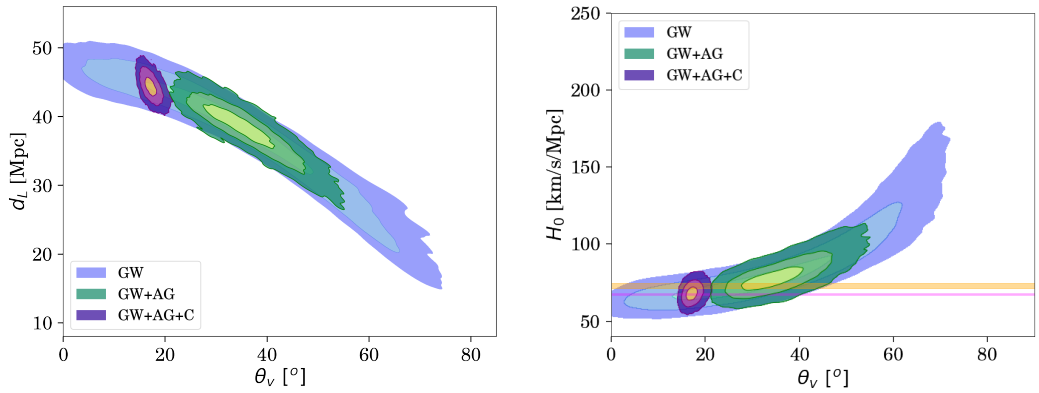

Figure 35: Same as Fig. 29, but using a Gaussian jet with the addition of a constant flux component at late times.

GW+AG fit with the simple Gaussian jet model, and the error on the distance is about 2 times better that the GW fit, cutting part of the tails of the $\theta_v - d_L$ degeneracy, see Fig. 35, top panel. Indeed, the retrieved Hubble constant value is $78.5^{+7.9}_{-6.4}$ km/s/Mpc, see the bottom panels of Fig. 30 and Fig. 35, that is compatible within 1σ with the GW+AG+C fit, including a constant component. Moreover, this result is compatible within 1σ with Guidorzi et al. [105], Wang and Giannios [236], and Wang et al. [237].

4.3.4 *The degeneracy $d_L - \theta_v$ for the jet centroid motion*

Unfortunately, also for the afterglow centroid motion there is a dependency on both the distance and the viewing angle. In fact, the magnitude of jet centroid motion in the sky can be estimated as

$$\Delta\theta_{cent} = \Delta t_{obs} \frac{d\theta_{cent}}{dt_{obs}} \tag{60}$$

where Δt_{obs} represents the time period of the observations and $d\theta_{cent}/dt_{obs}$ the apparent velocity of the remnant in the sky. The latter can be written as [see also 146]

$$\frac{d\theta_{cent}}{dt_{obs}} = \frac{\beta_{app} c}{d_A} \tag{61}$$

where d_A is the angular distance, c is the speed of light and $\beta_{app} = \beta \sin(\theta_v)/(1 - \beta\cos(\theta_v))$, where $\beta = \sqrt{1 - 1/\Gamma^2}$ and Γ is the jet Lorentz factor. We can assume to observe the jet at the jet break, when the velocity is at its peak [103, 198] and $\Gamma = 1/\theta_v$ (this is an overestimation, in reality, the velocity of the jet depends also on the energy of the jet and the circumburst medium, for example, a denser medium will produce a more luminous afterglow that moves slower, see [198]). For small θ_v, $\beta \sim 1$, so

$$\beta_{app} \simeq \frac{2}{\theta_v} \tag{62}$$

and the afterglow centroid motion in the sky can be written as

$$\Delta\theta_{cent} \simeq \Delta t_{obs} \frac{2c}{\theta_v d_A}. \tag{63}$$

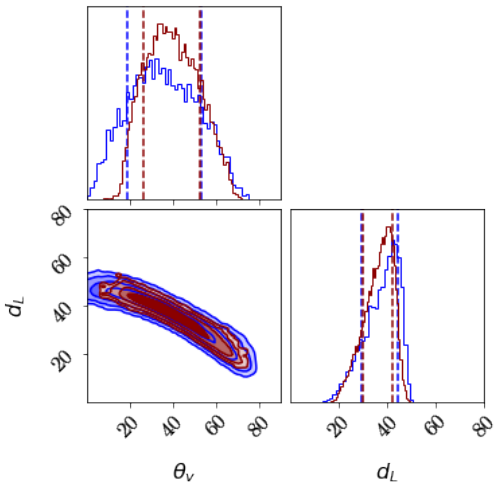

Figure 36: Contour plot of the viewing angle and luminosity distance. The contours represent the 68%, 95%, 99.7% and 99.99% probabilities. The blue contour lines represent the result from the GW fit, while the dark red lines represent the result from a fit using GW and centroid alone.

Also in this case, d_L (and d_A) is a decreasing function of θ_v. In the case of on-axis observers ($\theta_v < \theta_c$), the jet moves along the line of sight, so no displacement is visible. Because of the reasoning above, the centroid alone is not enough to break the GW degeneracy, indeed, a fit including only the centroid and the GW leads to no constraint on θ_v or d_L, see Fig. 36.

4.4 SUMMARY AND FINAL REMARKS

Utilizing GW to estimate the Hubble constant H_0, commonly referred to as the standard sirens method, proves to be a potent approach for addressing the Hubble tension. Nevertheless, a significant challenge lies in the degeneracy between the viewing angle and the luminosity distance of the event, preventing the achievement of the precision levels attained by *Planck* and SH0ES. This chapter employs the standard sirens method to estimate H_0, incorporating additional constraints to alleviate the aforementioned degeneracy.

With respect to the previous Chapter, here I add to the GW170817 EM data set the jet centroid motion from VLBI and HST. Thanks to a joint fit of EM and GW data sets, I estimate the Hubble constant and test its robustness depending on the data set used, on the assumed structure of the jet and on the presence of a possible late time flux excess in the afterglow light curve.

A GW-only fit leads to an Hubble constant value of $H_0 = 77^{+21}_{-10}$ km/s/Mpc (median, 16th-84th percentiles). The almost 20% error is due to the degeneracy stated above. The latter can be broken exploiting independent EM messengers, like the afterglow light curve and centroid motion, at least in the case of GW170817.

In GW+AG analysis, the GW and the afterglow light curve are joined. This fit reduces the $\theta_v - d_L$ degeneracy, but gives $H_0 = 96^{+13}_{-10}$ km/s/Mpc. This high value follows from the low value of distance ($d_L = 31.3^{+3.0}_{-3.6}$ Mpc) and high value of viewing angle ($\theta_v = 50.1^{+5.1}_{-5.4}$deg). This behaviour is caused by a possible late time excess in the afterglow flux, these data points are well modelled and are driving

the result of the fit. Therefore, for the specific case of GW170817, using only the afterglow as EM counterpart is not enough to get a reliable measurement of H_0.

The GW+AG+C fit, instead, joining the GW, the afterglow light curve and the centroid motion, breaks the $\theta_v - d_L$ degeneracy and results in $H_0 = 69.0^{+4.4}_{-4.3}$ km/s/Mpc, which is in agreement with other estimations of this parameter using GW170817 and is about 3 times more precise than the GW-only H_0 measurement. This is because of the very strong constraint on the viewing angle given by the afterglow centroid data set. As a consequence, the latter model does not fit well (even if the residuals are $\leqslant 3.5\sigma$) the late time flux data points. The viewing angle is $\theta_v = 18.2^{+1.2}_{-1.5}$deg and the distance is $d_L = 43.7^{+1.4}_{-1.4}$ Mpc. Thus, in the GW+AG+C fit a small value of θ_v, and consequently a highly collimated jet and a large energy on the jet axis, is preferred. In the GW+AG fit a large θ_v, with a broader profile and less energy on the jet axis, is preferred instead.

The possible excess in the afterglow light curve at late times can be explained as either something missing in the jet model, or as a new emission becoming visible [107, 177, 224]. In either cases, adding a constant flux component to the GW+AG+C model at late times leads to posterior probabilities that are in agreement within 1σ with the fit without this constant component ($H_0 = 68.0^{+4.4}_{-4.2}$ km/s/Mpc), but helps in better fit the late times data. This shows that the model and the GW+AG+C results are robust. Instead, adding this constant flux component to the fit of GW+AG leads to more acceptable values of viewing angle, luminosity distance and Hubble constant: $\theta_v = 35.2^{+5.7}_{-6.2}$ deg, $d_L = 38.6^{+2.5}_{-3.0}$ Mpc and $H_0 = 78.5^{+7.9}_{-6.4}$ km/s/Mpc. The latter is compatible within 1σ with the GW+AG+C fit.

Finally, it seems that the Hubble constant is not influenced by the assumption on the structure of the jet (either Gaussian or power law), at the present level of precision.

It is to be noted that other systematic uncertainties in the Hubble constant estimation can arise from the estimation of the peculiar velocity of the host galaxy [118, 161]. The latter, in this work (see Eq. (59)), is included in the Hubble flow velocity [3]. In this analysis, a shift in the NGC4993 peculiar velocity of ~ 140 km/s leads to a shift in H_0 of ~ 4 km/s/Mpc, in agreement with Nicolaou et al. [161]. This is still inside the H_0 precision reached in this work, but, for a larger number of events, will become one of the main sources of uncertainty.

The best H_0 precision reached with this method is 4 km/s/Mpc, in the case of GW+AG+C fit. This is not good enough to prefer either the *Planck* or the SHoES H_0, yet. More events are needed to reach their level of precision. However, in the future, we do not expect many events that have coincident detections of GW, afterglow light curve and centroid motion, see the next Chapter for a detailed explanation.

In conclusion, the introduction of additional constraints derived from astronomical observations has the potential to introduce systematic biases that may impact standard sirens measurements [49, 102, 161]. In this Chapter, I demonstrate that the viewing angle in EM modeling is influenced by the type of data set utilized. Therefore, it is crucial to incorporate all available messengers in the analysis to ensure robust results.

Currently, the uncertainty associated with standard sirens methods remains too large in comparison to early or late-time Universe H_0s. However, future efforts should focus on minimizing biases. For instance, in cases resembling GW170817,

measurements at very late times could either confirm or qualify the milder decrease of flux as a systematic effect. Concerning jet centroid studies, obtaining measurements at both early and late times is crucial for constraining motion and viewing angles. To achieve this, highly sensitive instruments such as *Athena* in the X-rays [178] or SKA (Square Kilometre Array) in the radio band [39] are necessary. Looking ahead to the mid-2030s, facilities like the Next Generation VLA (ngVLA) with mas resolution or lower [25] hold promise for detecting the motion of relativistic jets.

5

CONCLUSIONS AND FUTURE PROSPECTS

The binary neutron star merger GW170817 has significantly paved the path for multi-messenger astrophysics by emitting radiation throughout various phases of its existence, with gravitational radiation, a GRB and its afterglow, and a kilonova. Jointly modelling all this information, through Bayesian analysis, leads to improved characterization of the event, not only for the parameters in common between the analysed messengers, but also, as a back reaction, in the correlated parameters. The general agreement from the literature is that the system is at about 40 Mpc distance, and the jet is inclined of ~20-30 deg from our line of sight. In this thesis, the joint Bayesian analysis of the GW, the afterglow radio, optical and X-rays light curve and jet centroid motion of GW170817, is carried out to address the pressing questions outlined in the Introduction.

The joint bayesian fit of GW and EM, in particular afterglow light curve, domains is used to tackle a pressing issue in the astrophysics of GRB jets, which is the energetics and the structure of the jet. In particular, the jet opening angle θ_c is particularly relevant for the energy of the explosions, which then affects also the central engine and the rates of short GRBs. However, θ_c is correlated with the viewing angle θ_v, so it is very difficult to obtain a precise estimation of them singularly. In Chapter 3 it is shown that, in the case of GW170817, a joint analysis of the two messengers can ease the degeneracy, but does not completely break it. In particular, assuming a Gaussian structure for the jet and fixing the luminosity distance to 41 Mpc, the angles are already very well constrained in the EM-only fit, with $\theta_v = 38^{+2}_{-2}$ deg and $\theta_c = 7.0^{+0.4}_{-0.5}$ deg, thanks to the well sampled light curve, both at early and late times in the X-rays and radio band. Therefore, the GW domain eases the degeneracy at 5σ, but leaves the 1σ errors unvaried, leading to $\theta_v = 34^{+2}_{-2}$ deg and $\theta_c = 6.2^{+0.4}_{-0.5}$ deg, just shifting the median value of the posterior distributions. The jet opening angle is fundamental to evaluate the beaming factor $< (1 - \cos\theta_c)^{-1} >$, which is the fraction of GRBs that points toward Earth. The latter, in turn, affects the calculations of the burst true energetics. The θ_c ~6 deg is in agreement with the average opening angle estimated in population studies and simulations (between 3 and 6 deg [71, 92]). In this analysis, the isotropic-equivalent kinetic energy is $E_0 \sim 10^{52}$ erg (this is an approximation, since in the case of a structured jet the integral over the energy distribution should be done), while the beaming corrected kinetic energy is $\sim 7 \times 10^{49}$ erg. This energetics is, again, in agreement with population studies of short GRBs [71, 81], with median values of $\sim 10^{49}$ erg. The jet opening angle also influence the estimation of the true event rate. In fact, the emission from the jet is visible only for observers within the jet cone. Therefore, the true event rate should be larger by a factor $1/(1 - \cos\theta_c)$, with respect to the observed one. We will expand the discussion on GRB rates in the following Sections.

The structure of the jet determines the properties of the emission for different observers, therefore influencing also the detectability of these source and, in particular, the rate of low luminosity off-axis events. GW170817 was the first GRB seen off axis, as the light curve with an early rising phase shows. This mild rising phase is the proof of the presence of a structured jet. Infact, in the case of a uniform jet, the rising slope would have been steeper. While the Top-Hat jet can be discarded when analysing GW170817 afterglow light curve, the Gaussian and power law jets give both a good fit and we cannot prefer one of the two. The power law jet seems to better fit only the first X-ray data point at ~ 8 days. However, the kind of power law jet preferred in the fit (with the power law index of ~ 10) is similar to a Gaussian structure, as the wings are quite steep. This uncertainty is probably due to the lack of early detections in both radio and X-ray bands. Indeed, the difference between the two structures is expected mainly at early times, since, after the jet break, the whole jet is visible and the emission is dominated by the most energetic core.

The high value of viewing angle (above 30 deg) aforementioned is mainly due to a marginal late time flux excess in the X-rays and radio bands. This is due to the fact that, not placing any external constraint on the viewing angle, the fit is free to account and model this possible late time flux excess combining the choice of a high θ_c, therefore a higher flux, and the anticipation of the non-relativistic phase. Fortunately, in the case of GW170817, there is another data set, the relativistic jet motion, captured in the radio images from VLBI and optical images by HST. The latter, assuming a Gaussian jet, strongly constraints the viewing angle to $\theta_v = 18.2^{+1.2}_{-1.5}$ deg, and the jet opening angle to $2.85^{+0.24}_{-0.20}$ deg. Even accounting for a new emission at late times including an additive constant flux, leads to the same results. In general, the inclusion of the centroid motion in the analysis moves the preference of the fit to a highly collimated jet with high energy on the jet axis, with respect to a fit that includes only GW and afterglow light curve. Indeed, in this case, the isotropic kinetic energy is $E_0 = 10^{54}$ erg, which gives $\sim 10^{51}$ erg corrected for the beaming factor, a quite high value, near to the high end of the kinetic energy distribution of short GRBs [71, 81].

A still unexplained issue in the astrophysics of GW170817 is what in this thesis is found to be a marginal flux excess at late times, in the radio and optical bands, mentioned also above. The latter strongly influence the GW170817 features, leading to biases in the viewing angle, and consequently on θ_c and the energetics. This flux excess is probably not due to the jet structure modelling, as at this late times, we are looking at the whole jet (since we are after the jet break). In this phase the emission is dominated by the core, which is the most energetic part. A more likely, and more exciting hypothesis, is that a new emission is becoming visible, from the remnant of the merger, or from the kilonova. The former could be a long-lived NS. Despite simulations show that long-lived NSs, as merger remnants, are able to produce a jet, its Lorentz factor would be much smaller than the GRB case [53], thus pointing in favour of a BH remnant. On the other hand, the emission from the kilonova at late times is called kilonova afterglow. In this case, the material that undergoes radioactive heating and produce the kilonova, then continues to expand into the circumburst medium. This ejecta can sweep up ambient material (as the GRB jet does) and drive a synchrotron-producing forward shock wave: the kilonova afterglow [157]. However, at the moment, the flux is only slightly above

to the sensitivity of the available instruments, like *Chandra* in the X-rays or VLA in the radio band, so the detection of this counterpart is going to be difficult.

The pressing issue in cosmology that is introduced at the beginning of this thesis is the Hubble tension between the late and early time Universe. In Chapter 4, the luminosity distance is left free, in order to estimate the very Hubble constant. A GW-only analysis leads to a poor precision, because of the degeneracy between the luminosity distance and the inclination. This, coupled with the afterglow light curve at late times, which seems to suggest an excess in the flux with respect to a simple Gaussian jet model, is strongly influencing the results of the joint analysis of the GW and afterglow light curve. Therefore, either we account for this excess in the analysis, or another data set is needed to break both the GW $d_L - \theta_v$ and the EM $\theta_v - \theta_c$ degeneracies. In the first case, including a constant additive flux component in the fit of the afterglow light curve in the GW and afterglow analysis, brings $H_0 = 78.5^{+7.9}_{-6.4}$ km/s/Mpc, which is compatible within 1σ with *Planck* and 2σ with SHoES measurements, but does not have the precision needed to prefer one of the two. In the second case, the jet centroid motion is included in the fit, with the GW and the afterglow light curve. This constraints precisely H_0 to $69.0^{+4.4}_{-4.3}$ km/s/Mpc, which is about 3 times more precise than the GW-only H_0 measurement. This is thanks to the fact that both the GW $d_L - \theta_v$ and the EM $\theta_v - \theta_c$ degeneracies are broken. In this fit, the viewing angle has a 10 times more precise estimation, and the luminosity distance a 5 times more precise estimation with respect to a GW-only analysis. This H_0 measurement is in agreement with other estimations of this parameter using GW170817 and is in agreement within 1σ with both *Planck* and SHoES. Moreover, it is found in this thesis that the Hubble constant is not influenced by the assumption on the structure of the jet (either Gaussian or power law), at the present level of precision. This is a very powerful tool to help in the Hubble tension, however, we need better precision to reach the *Planck* or SHoES level.

5.1 FUTURE PERSPECTIVES

More binary NS events, with the associated GW, GRB and its afterglow, and kilonova, are necessary to improve our understanding of GRB's jets, particularly the off-axis events, for which the jet structure plays a fundamental role, but also to improve the precision on the Hubble constant. At the moment, the GW Observing run O4 is running (started in May 2023 and will last 20 calendar months, up to early 2025), while O5 is due after 2027.

The issue of the geometry, and in particular the estimation of the jet opening angle, and the structure identification could be very challenging to explore for distant events, which are much more likely than GW170817. In particular, in Chapter 3 we extend the same methodology applied to GW170817 to two GW170817-like events situated at greater distances (70 and 136.5 Mpc) and occurring during the O4 observing run. In the EM-only fit the further is the event, the worse is this degeneracy, leaving at 136.5 Mpc the two angles unconstrained above 1σ. This is simply due to the fact that the flux decreases with distance, so the rise of the afterglow drops below the sensitivity of all instruments: this part is what places the most stringent constraints on the structure of the jet, depending on its steepness. Moreover, it also constraints the ratio of θ_v and θ_c, assuming a Gaussian structure.

Even including the GW domain acts only on θ_v, so at large distance, θ_c is still unconstrained above 1σ. This causes a large uncertainty on θ_c, which is 7^{+15}_{-2} deg, and consequently on the beaming factor. The latter leads to a beaming corrected kinetic energy between $\sim 5 \times 10^{49}$ erg and $\sim 6 \times 10^{50}$ erg, which is almost an order of magnitude range (1σ range), taking the median value of the isotropic kinetic energy of $\sim 10^{52}$ erg. These results assume the mock event inclination to be the same as GW170817, however, the higher the distance, the higher is the probability to get a more aligned event. In such cases, the flux is higher, and the light curve would be better sampled, probably leading to a more precise estimation of the jet core angle and viewing angle (thanks to the detection of the jet break in the light curve). At 70 Mpc, instead, the EM dataset can constrain better these angles. There is still a strong degeneracy, which is, however, broken by the GW domain, giving results comparable to the ones of GW170817. Therefore, up to this distance, we are still able to constraint the jet opening angle, if we include the GW information on the viewing angle. However, the expected number of events below this distance is below 0.1 yr^{-1}, see Fig.39 for both O4 and O5, taking the VLA sensitivity as a reference. Therefore, the need for more sensitive instruments is clear.

As time goes by, there is the exciting possibility to detect the kilonova afterglow for GW170817, and therefore explain the possible late time excess in the afterglow light curve. The kilonova afterglow has never been detected, but it is indeed predicted by the modelling on binary NS mergers. However, the GW170817 flux is now near the sensitivity level of the available instruments, like for example *Chandra*, therefore it could be difficult to actually detect such an emission. For further events, new instruments with high sensitivity will be fundamental, like *Athena* in the X-rays. With such an instrument, in a GW170817-like case, it would be very easy to routinely detect and study the kilonova afterglow, see Fig.9. Some examples of expected light curves are in Fig. 37, for different ejecta masses M_{ej} and velocities β. The kilonova afterglows of shock waves with velocities higher than 0.2 should be detectable with *Athena*. These correspond to the afterglow of the "blue" kilonova observed in GW170817. While the "red" (slower) kilonova should be in a high density environment to be detected. The kilonova afterglow emission offers an independent way of estimating the mass of the ejecta, which is fundamental also to reconstruct the heavy elements formation.

With more of such events also the Hubble tension could be addressed. For example, in order to reach the *Planck* or the SHoES H_0 level of precision, if we assume an error on H_0 of 4 km/s/Mpc, we would need $\sim$ 60 events and $\sim$ 10 events respectively. However, realistically, it is unlikely to see even just another one centroid motion measurement during O4 and O5, as it will be shown in the following Section. For this reason, the achievable precision on H_0 can be of about 7 km/s/Mpc, assuming a well sampled afterglow light curve like GW170817. This means that $\sim$ 200 events and $\sim$ 30 events are needed to reach the *Planck* or the SHoES level respectively.

5.1.1 *Prospects for jet centroid observations*

The best precision on the Hubble constant in this thesis is given by the joint fit of GW, afterglow light curve and centroid motion. In this Section, we estimate the likelihood that a new GW event, followed by the detection of the afterglow light

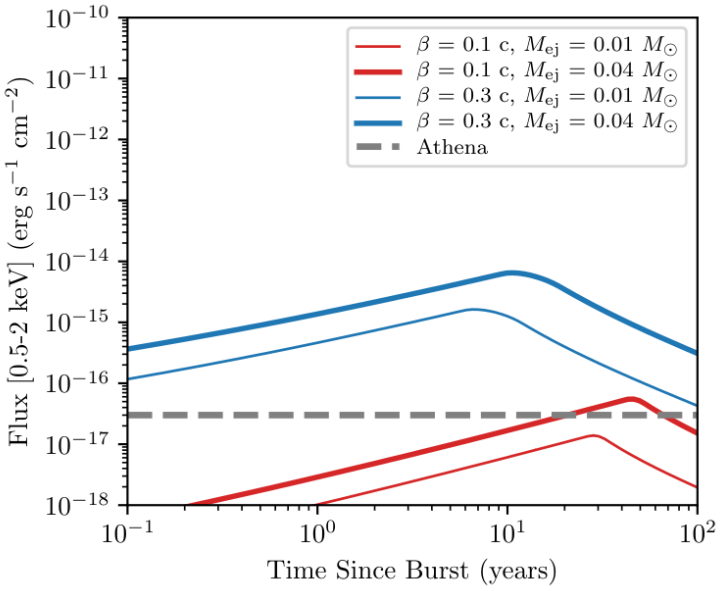

Figure 37: Light curves of a kilonova afterglow at the same distance of GW170817 at different characteristic ejecta velocities and ejecta masses. See Piro et al. [178] for the parameters values of the kilonova modelling. The fiducial Athena sensitivity is $3 \times 10^{-17} ergs^{-1} cm^{-2}$ in 0.5-2 keV band [178].

curve and the measurement of the afterglow centroid motion, is seen in the next GW Observing runs O4 and O5.

These estimations are based on GW population synthesis simulations by Petrov et al. [173]. In the latter, a sample of simulated compact binaries is drawn with a realistic astrophysical distributions of masses, spins, distances, and sky locations. Then their GW signals are simulated and Gaussian noise is added. A cut based on the threshold for detection of $S/N > 8$ for BNSs is applied. This results into a GW rate for binary NS mergers of $34^{+78}_{-25} yr^{-1}$ in O4 and $190^{+410}_{-130} yr^{-1}$ in O5 [173]. From these GW simulations, I generate the EM counterparts of 1482 and 2307 binary NS events detectable in O4 [213] and in O5 [214] respectively, assuming a Gaussian jet. Each GW event is characterized by an inclination and a luminosity distance, which I use to generate their afterglow light curve and centroid motion. For inclinations larger than 90 deg, they are converted in EM viewing angles as explained in Section 3.2.1. We assume all the other parameters to be the same as GW170817 (see Table 6, fourth column). Moreover, we assume that all the events are well localized and easy to be followed up by the radio telescopes. This will lead to optimistic rates. We adopt VLBI as the reference radio facility, both for O4 and O5, so we assume a sensitivity in the radio band of 24μJy (the observations of GW170817 afterglow centroid motion reached an RMS of about 8μJy), and a resolution of 1.5 mas [93]. These performances can be achieved also, for example, with the European VLBI Network (EVN)[1].

The centroid data set is composed of the same detection times of GW170817, but we adopt fluxes and positions predicted by the model. We assume that the afterglow centroid motion is visible if the offset between two data points is above the assumed resolution and its flux is above the sensitivity. This strategy is fixed for all events. In general the best strategy to detect the centroid motion would be

1 EVN website

to have two (or more) observations separated by a long period of time, however, as the time goes by, the flux decreases, risking a non detection at late times. Therefore, in general, it is probably best to observe the event as often as possible, maybe even have closer observations with respect to the GW170817 strategy.

In the case of O4, the GW rate of events is 34^{+78}_{-25} yr^{-1} [173]. Regarding jet centroid observations, we find that only 0.13% of events has a detectable afterglow flux and centroid, see red dots in Fig. 38, in agreement with Mastrogiovanni et al. [146]. This translate into a rate of $0.05^{+0.11}_{-0.03}$ yr^{-1}, therefore it is very unlikely that the jet centroid will be measured again during O4. In the case of the O5 run, the predicted GW rate is 190^{+410}_{-130} yr^{-1}. The jet centroid motion is visible in 0.09% of the cases leading to a rate of $0.17^{+0.36}_{-0.12}$ yr^{-1}. This rate is slightly larger than O4, despite the same number of GW events at distances lower than 100 Mpc (~ 1 yr^{-1} both for O4 and O5). For this reason, we can say that the rate fluctuation is just due to the small number of events. As is shown in Fig. 38, at large distances we mainly see on-axis or almost on-axis events (with a small θ_v), these events will not have a visible jet motion, as the observer is within (or just outside) the jet's opening angle. This results in a small or null offset, which is hardly detected with sensitivities of the order of the mas. However, if the jet has a large viewing angle, the peak of the afterglow will be at low fluxes, not reaching the VLBI sensitivity. Indeed, for the O4 run, the events that have a coincident detectable GW, afterglow light curve and centroid motion are very similar to GW170817 (at small distances and with $\theta_v \sim 20$ deg, red dots in Fig. 38).

Focusing instead only on afterglow detections during O4 and O5, we require that the light curve is sampled with at least 3 or 4 data points in the rising phase. We take VLA as the reference instrument: it can achieve an RMS of 2μJy (see Chapter 3), therefore we assume a 3σ sensitivity of 6μJy. We take as condition for the detection, that the afterglow flux is above 24 μJy. An example of observing strategy is presented in Fig.25. In O4, we find that 7% of the total have detectable flux, resulting in a rate of $2.4^{+5.5}_{-1.8}$ yr^{-1} (for the whole sky). In O5, instead, we find 6%, resulting in a rate of 11^{+25}_{-8} yr^{-1}. The slightly lower event fraction of O5 with respect to O4 is due to the fact that O5 will probe larger distances. In particular the median achievable luminosity distance in O4 is 350 Mpc, while in O5 is 600 Mpc. Looking at Fig.39, we can see that the rates up to ~400 Mpc (average distance of O4) are similar for both O4 and O5, and this explains the small difference.

Therefore, in the future, we expect no centroid detections, but about 2 and 10 events per year in O4 and O5 respectively, which should both last ~2 years.

5.2 PROSPECTS FOR EINSTEIN PROBE DETECTION OF A GW COUNTERPART

Einstein Probe (EP) is a mission of the Chinese Academy of Sciences (CAS), in collaboration with the European Space Agency (ESA) and the Max Planck Institute for extraterrestrial Physics (MPE), Germany, dedicated to time-domain high-energy astrophysics. Its primary goals are to discover high-energy transients and monitor variable objects. It has two telescopes on board: the Wide-field X-ray Telescope (WXT), which has a very large instantaneous field-of-view (3600 square degrees) achieved by using established technology of lobster-eye optics. Unprecedentedly high sensitivity with respect to previous and existing X-ray all-sky monitors

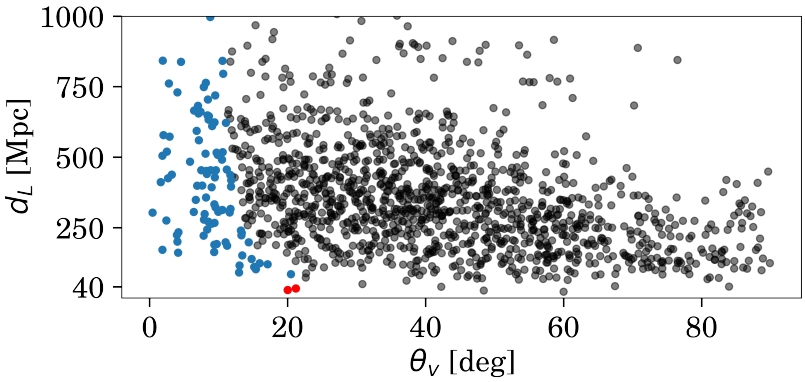

Figure 38: The dots represent GW events simulated by [173], in the case of the O4 run [213]. Depending on their θ_v and d_L, we highlight in blue the ones that have a detectable afterglow counterpart in the radio band and in red the ones that have also a detectable afterglow centroid motion.

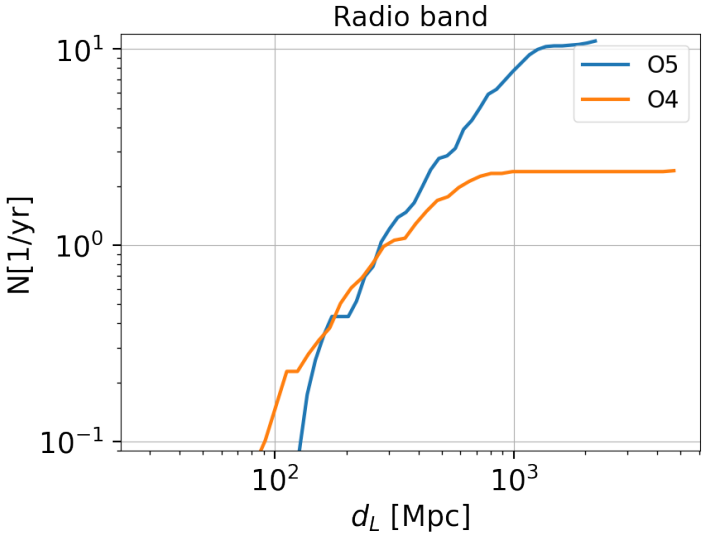

Figure 39: The expected rates of binary NS mergers with a radio counterpart detectable by VLA, depending on the luminosity distance.

(eROSITA and XMM-Newton). The bandpass is 0.5-4.0 keV [251]; the Follow-up X-ray Telescope (FXT), which is an X-ray focusing telescope (Wolter-I optics) with a larger effective area to perform follow-up characterization. It has a narrow field of view (60 arcmin in diameter) and a source localization error of 5-15 arcsec (90% c.l.) depending on the source strength. The bandpass is 0.5-10 keV [251, 255]. EP was successfully launched the 9th of January, 2024, the expected lifetime is 3 years, overlapping with the GW observing run O4.

I present here the expected rates for the number of NS binary mergers to be detected as multi-messenger sources during the GW O4 run by Einstein Probe. These expectations are, again, based on GW population synthesis simulations by Petrov et al. [173]. For each GW event, I generate the EM counterparts, in particular the prompt emission of a GRB and its afterglow, for both a Gaussian jet is assumed. Regarding the afterglow, the energetics and the microphysics are fixed to the ones of GW170817, as also the jet opening angle. For it to be detectable, the maximum of the light curve, at early times if the object is on axis, or at some days/months if the jet is off-axis, must be above the sensitivity of FXT or WXT. Regarding the prompt emission, we assume the same energetics and duration of GW170817 in the Fermi-GBM detector (10-1000 keV [96]), and the unabsorbed flux (the absorbed one is just a factor 0.1 lower) is extrapolated to the 0.5-4 keV band of WXT.

These are optimistic rates, since we assume that all the mergers result in a successful jet (in Colombo et al. [54] half does).

5.2.1 *GRBs prompt emission*

The observation scenario considered for the detection of the prompt phase of a GRB is the following: WXT carries out survey observations of X-ray transients of few seconds and detects a source simultaneously with GW and within the GW sky region. Considering the 1s sensitivity[2] of WXT (0.5 - 4 keV, 5σ, $\sim 9 \times 10^{-9} erg/cm^2/s$), we expect about 0.04 $yr^{-1}sr^{-1}$ events with an EM counterpart in the WXT FOV, all on axis events, see Fig.40. Therefore, in the EP lifetime, we do not expect to see any prompt emission as counterpart of a GW event.

5.2.2 *X-ray afterglow*

EP-WXT is programmed to carry out fast observations of GW counterparts. In particular, in the cases where a rough localization is given by high energy satellites, like *Fermi*-GBM, where the mean 90% credible region area is $\sim$ 200 deg^2 [97], or by GW detectors, the predicted 90% credible area for O4[3] is $\sim$ 1800 deg^2, the best instrument to point is WXT. Infact, these areas are easily covered by the wide WXT FOV (3600 deg^2, 1 sr) in one pointing. In this case, assuming that EP can be on source after some minutes from the GW trigger (the typical on source time of WXT [251]), we expect about 3 yr^{-1} events detectable by WXT, see Fig.41, blue lines. All the detectable counterparts are from on-axis or close to on axis events (dotted and dashed lines in Fig. 41). This is assuming the typical exposure time of 1000s for WXT [251], see vertical purple line in the Figure.

2 https://ep.bao.ac.cn/ep/cms/article/view?id=38

3 https://emfollow.docs.ligo.org/userguide/capabilities.html#detection-rate-and-localization-accuracy

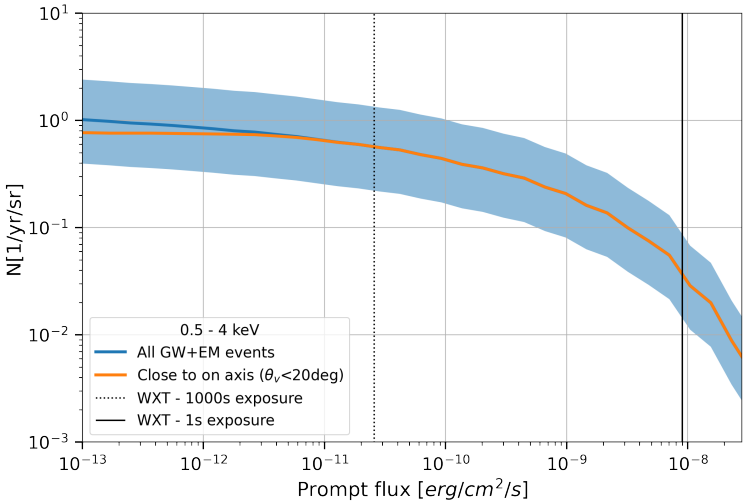

Figure 40: Rate of O4 GW events with a detectable prompt counterpart, on the x axis the flux in the WXT 0.5 - 4 keV band. The blue and orange lines represent the whole population of binaries and the binaries with a viewing angle lower than 20 deg respectively. The vertical black line represents the WXT sensitivity in a 1 s exposure. The sensitivity for 1000s exposure is represented with a vertical dotted line for reference. The blue shaded region represent the uncertainty given by the GW-only rates, reported in [173]. The GW170817 extrapolated flux in the band 0.5 - 4 keV is 2×10^{-10} erg/cm^2/s, which is below the sensitivity of WXT. The rates are normalized per 3 yr^{-1} sr^{-1}.

Once the X-ray afterglow has been identified with WXT, FXT (having a higher sensitivity, green vertical line in Fig.41) can follow up the source in the following hours and days. We expect also that FXT will carry out follow up observations of *bona fide* counterparts in other wavelengths. In this case, the identification of an optical counterpart, a kilonova, has a timescale of some days, so the instrument cannot be on source earlier, while the waiting time for the refined localization from high energy satellites can take some hours. In this cases, after some hours we expect about 5 yr^{-1} events with an FXT detectable afterglow (only about 0.1 yr^{-1} events detectable by WXT), mainly on axis or close to on axis events, see Fig.41, light green curves. This is because the light curves of the detectable events are mainly decreasing, since we are on axis or close to on axis. After some days, instead, we expect 3 yr^{-1} events to be detectable by FXT, see Fig.41, lime curves.

It is to be noted that the FXT rates for observations starting at 4 hours and 2 days (Fig.41) after the merger are similar. This is because also the light curves are alike, as the simulated events are clustered aroud the median distance of 350 Mpc for the GW O4 simulations. Moreover, all the jet parameters, except the viewing angle and the distance are fixed. Indeed, 65% of the light curves detectable at 4 hrs still detectable at 2 days.

Therefore, during O4, we expect about 5 events per year with an X-ray afterglow detectable by EP.

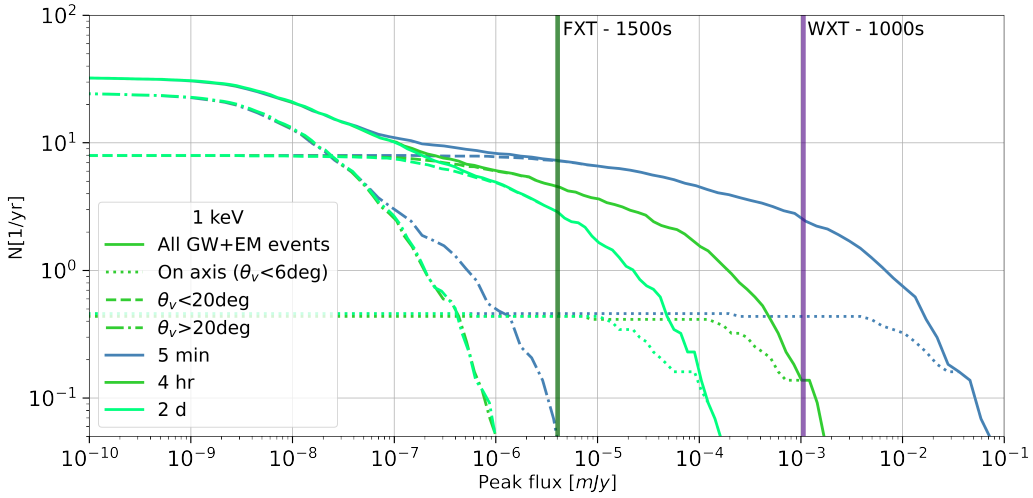

Figure 41: Rates of O4 GW events with a detectable X-ray afterglow counterpart, on the x axis the flux density in mJy at 1 keV. The colors represent different on source times: blue for 5 minutes, light green for 4 hours and lime for 2 days. The solid and dotted lines represent the whole population of binaries and the on axis binaries (viewing angle lower than 6 deg) respectively, while the dashed line represents the close to on axis case and the dot-dashed line represents the off-axis one. The vertical shaded lines represents the FXT sensitivity in a 1500 s exposure and the WXT sensitivity in a 1000 s exposure.

5.3 CONCLUDING REMARKS

As demonstrated in this thesis, GW170817 represents an event extremely rich in information, encompassing a broad spectrum from astrophysics to gravitation and cosmology. However, the ones presented in this work are not the only fields enriched by the study of binary NS mergers. Indeed, another possible field of astrophysics in which binary neutron star mergers can be useful is the NS equation of state, where new tighter constraints on the masses can be placed thanks to the joint fit of the kilonova emission and the GW. Many studies exploited Bayesian methods to combine GW and the associated kilonova AT2017gfo, this provides improved estimates on the mass ratio and tidal deformability [40, 47, 55, 56, 62, 160, 181, 182, 184, 185]. The kilonova emission modelling depends on several other parameters, for example the asymmetry (or symmetry) of the ejecta. This can influence the kilonova emission [42, 246], leading also to constraints on the inclination of the system. Therefore, in the absence of the centroid motion (which is the best at constraining the inclination), kilonova emission could help in constraining the degeneracy between the inclination and the jet opening angle, proper of the afterglow modelling. This, as a consequence, would also lead to a constraint on the distance thanks to the GW modelling. Indeed, the future step for this work is the inclusion of the kilonova emission in the joint fit. Moreover, also the prompt emission of the GRB can be included, the latter (but also the kilonova) shares the inclination parameter with the other models. The final goal is to apply the complete analysis to a future binary NS event with EM counterparts, to be detected in O4 and/or O5.

From the rates presented in the previous Sections, we see that in O4 the expected number of binary NS mergers with EM counterparts is less than 10 (either in the X-rays or radio band). In O5, assuming a duration of about 2 years, we expect about

20 events with a radio counterpart. Moreover, the EP mission is formally approved for 3 years, but will probably continue operations for longer, maybe superimposing with O5. With a sample of ~20 events, population studies can be done, allowing to study the light curves and the relativistic jet features. In particular, these will enrich our knowledge about the typical jet opening angles and about the energetics. The off-axis events will offer a unique position to study the structure of the jet, maybe helping in understand which type of structure better describe the jet. The Hubble constant precision, with such number of events, would reach ~1.6 km/s/Mpc, which is very near to the SHoES precision of 1.4 km/s/Mpc.

Moreover, in the further future, not only facilities like *Athena* in the X-rays, will be fundamental, but also new GW detectors, like KAGRA and LIGO India, which will play a major role in constraining the localization of the GW event, helping the search for EM counterparts. A break trough will be Einstein Telescope (ET, construction is expected to start in 2030s), it will have an order of magnitude better sensitivity and a wider accessible frequency band with respect to LIGO and Virgo detectors. ET will be a ground-based GW interferometer, the arm length will be increased with respect to LIGO and Virgo and it will be composed of either two L-shaped detectors, or one triangular shape detector, with three nested interferometers [38]. ET will detect tens of thousand of binary NS mergers [38], giving actually the reverse problem, which is how to chose the events to be followed up by EM facilities. For example, since the GW inclination is better constrained when the source is edge-on, the priority in the follow up of these events should go to the face-on events (so with an on-axis jet), where the EM constraints on the inclination are solid [195].

The future is gravitationally and electromagnetically bright, if we have patience.

BIBLIOGRAPHY

[1] J. Aasi et al. "Advanced LIGO." In: *Class. Quant. Grav.* 32 (2015), p. 074001. DOI: 10.1088/0264-9381/32/7/074001.

[2] B. P. Abbott et al. "LIGO: the Laser Interferometer Gravitational-Wave Observatory." In: *Reports on Progress in Physics* 72.7 (2009), p. 076901. DOI: 10.1088/0034-4885/72/7/076901.

[3] B. P. Abbott et al. "A gravitational-wave standard siren measurement of the Hubble constant." In: *Nature* 551.7678 (2017), 85–88. ISSN: 1476-4687. DOI: 10.1038/nature24471.

[4] B. P. Abbott et al. "GW170817: Observation of Gravitational Waves from a Binary Neutron Star Inspiral." In: *Phys. Rev. Lett.* 119 (16 2017), p. 161101. DOI: 10.1103/PhysRevLett.119.161101.

[5] B. P. Abbott et al. "Gravitational Waves and Gamma-Rays from a Binary Neutron Star Merger: GW170817 and GRB 170817A." In: *Astrophysical Journal* 848.2 (2017), p. L13. DOI: 10.3847/2041-8213/aa920c.

[6] B. P. Abbott et al. "Multi-messenger Observations of a Binary Neutron Star Merger." In: *Astrophysical Journal* 848.2 (2017), p. L12. DOI: 10.3847/2041-8213/aa91c9.

[7] B. P. Abbott et al. "Properties of the Binary Neutron Star Merger GW170817." In: *Phys. Rev. X* 9 (1 2019), p. 011001. DOI: 10.1103/PhysRevX.9.011001.

[8] B. P. Abbott et al. "Prospects for observing and localizing gravitational-wave transients with Advanced LIGO, Advanced Virgo and KAGRA." In: *Living Rev. in Relativ.* 23 (1 2020), p. 3. DOI: 10.1007/s41114-020-00026-9.

[9] B. Abbott et al. "Observation of Gravitational Waves from a Binary Black Hole Merger." In: *Physical Review Letters* 116.6 (2016). DOI: 10.1103/physrevlett.116.061102.

[10] R. Abbott et al. "The population of merging compact binaries inferred using gravitational waves through GWTC-3." In: *arXiv e-prints*, arXiv:2111.03634 (Nov. 2021), arXiv:2111.03634.

[11] R. Abbott et al. "Open data from the first and second observing runs of Advanced LIGO and Advanced Virgo." In: *SoftwareX* 13 (2021), p. 100658. DOI: 10.1016/j.softx.2021.100658.

[12] T. Accadia et al. "Virgo: a laser interferometer to detect gravitational waves." In: *Journal of Instrumentation* 7.3 (Mar. 2012), p. 3012. DOI: 10.1088/1748-0221/7/03/P03012.

[13] F. Acernese et al. "Advanced Virgo: a second-generation interferometric gravitational wave detector." In: *Class. Quant. Grav.* 32.2 (2015), p. 024001. DOI: 10.1088/0264-9381/32/2/024001.

[14] C Affeldt et al. "Advanced techniques in GEO 600." In: *Classical and Quantum Gravity* 31.22 (2014), p. 224002. DOI: 10.1088/0264-9381/31/22/224002.

[15] L. Amati et al. "Intrinsic spectra and energetics of BeppoSAX Gamma-Ray Bursts with known redshifts." In: *A&A* 390 (July 2002), pp. 81–89. DOI: 10.1051/0004-6361:20020722.

[16] L. Amati. "The $E_{p,i}$-E_{iso} correlation in gamma-ray bursts: updated observational status, re-analysis and main implications." In: *MNRAS* 372.1 (Oct. 2006), pp. 233–245. DOI: 10.1111/j.1365-2966.2006.10840.x.

[17] K. A. Arnaud. "XSPEC: The First Ten Years." In: *Astronomical Data Analysis Software and Systems V*. Ed. by G. H. Jacoby and J. Barnes. Vol. 101. Astronomical Society of the Pacific Conference Series. Jan. 1996, p. 17.

[18] G. Ashton et al. "BILBY: A User-friendly Bayesian Inference Library for Gravitational-wave Astronomy." In: *Astrophysical Journals* 241.2, 27 (Apr. 2019), p. 27. DOI: 10.3847/1538-4365/ab06fc.

[19] Y. Aso, Y. Michimura, K. Somiya, M. Ando, O. Miyakawa, T. Sekiguchi, D. Tatsumi, and H. Yamamoto. "Interferometer design of the KAGRA gravitational wave detector." In: *Phys. Rev.D* 88.4, 043007 (Aug. 2013), p. 043007. DOI: 10.1103/PhysRevD.88.043007.

[20] P. Astone et al. "IGEC2: A 17-month search for gravitational wave bursts in 2005–2007." In: *Phys. Rev. D* 82 (2 2010), p. 022003. DOI: 10.1103/PhysRevD.82.022003.

[21] A. Balasubramanian, A. Corsi, K. P. Mooley, M. Brightman, G. Hallinan, K. Hotokezaka, D. L. Kaplan, D. Lazzati, and E. J. Murphy. "Continued Radio Observations of GW170817 3.5 yr Post-merger." In: *ApJ Lett.* 914.1 (2021), p. L20. DOI: 10.3847/2041-8213/abfd38.

[22] A. Balasubramanian, A. Corsi, K. P. Mooley, K. Hotokezaka, D. L. Kaplan, D. A. Frail, G. Hallinan, D. Lazzati, and E. J. Murphy. "GW170817 4.5 Yr After Merger: Dynamical Ejecta Afterglow Constraints." In: *ApJ* 938.1, 12 (Oct. 2022), p. 12. DOI: 10.3847/1538-4357/ac9133.

[23] D. Band et al. "BATSE Observations of Gamma-Ray Burst Spectra. I. Spectral Diversity." In: *ApJ* 413 (Aug. 1993), p. 281. DOI: 10.1086/172995.

[24] S. Barthelmy, G. Chincarini, D. Burrows, et al. "An origin for short gamma-ray bursts unassociated with current star formation." In: *Nature* 437 (Oct. 2005), pp. 994–996. DOI: 10.1038/nature04392.

[25] A. Beasley et al. "Multiwavelength Astrophysics in the Era of the ngVLA and the US ELT Program." In: *Bulletin of the AAS* 51.7 (2019).

[26] K. Belczynski, R. Perna, T. Bulik, V. Kalogera, N. Ivanova, and D. Q. Lamb. "A Study of Compact Object Mergers as Short Gamma-Ray Burst Progenitors." In: *ApJ* 648.2 (2006), pp. 1110–1116. DOI: 10.1086/505169.

[27] A. M. Beloborodov and P. Mészáros. "Photospheric Emission of Gamma-Ray Bursts." In: *Space Science Reviews* 207.1-4 (2017), pp. 87–110. DOI: 10.1007/s11214-017-0348-6.

[28] P. Beniamini and J. Granot. "Properties of GRB light curves from magnetic reconnection." In: *MNRAS* 459.4 (July 2016), pp. 3635–3658. DOI: 10.1093/mnras/stw895.

[29] P. Beniamini and T. Piran. *Ultrafast compact binaries mergers*. 2023.

[30] M. G. Bernardini, R. Margutti, G. Chincarini, C. Guidorzi, and J. Mao. "Gamma-ray burst long lasting X-ray flaring activity." In: *A&A* 526, A27 (Feb. 2011), A27. DOI: 10.1051/0004-6361/201015703.

[31] S. Bernuzzi, A. Nagar, T. Dietrich, and T. Damour. "Modeling the Dynamics of Tidally Interacting Binary Neutron Stars up to the Merger." In: *Phys. Rev. Lett.* 114.16 (2015). DOI: 10.1103/physrevlett.114.161103.

[32] P. N. Bhat et al. "Temporal deconvolution study of long and short gamma-ray burst light curves." In: *ApJ* 744.2 (2011), p. 141. DOI: 10.1088/0004-637X/744/2/141.

[33] L. Blanchet, T. Damour, B. R. Iyer, C. M. Will, and A. G. Wiseman. "Gravitational Radiation Damping of Compact Binary Systems to Second Post-Newtonian Order." In: *Phys. Rev. Lett.* 74 (18 1995), pp. 3515–3518. DOI: 10.1103/PhysRevLett.74.3515.

[34] R. D. Blandford and C. F. McKee. "Fluid dynamics of relativistic blast waves." In: *Physics of Fluids* 19 (Aug. 1976), pp. 1130–1138. DOI: 10.1063/1.861619.

[35] R. D. Blandford and R. L. Znajek. "Electromagnetic extraction of energy from Kerr black holes." In: *MNRAS* 179 (May 1977), pp. 433–456. DOI: 10.1093/mnras/179.3.433.

[36] G. Boella, R. C. Butler, G. C. Perola, L. Piro, L. Scarsi, and J. A. Bleeker. "BeppoSAX, the wide band mission for X-ray astronomy." In: *Astron. Astrophys. Suppl. Ser.* 122.2 (1997), pp. 299–307. DOI: 10.1051/aas:1997136.

[37] C. R. Bom and A. Palmese. *Standard Siren Cosmology with Gravitational Waves from Binary Black Hole Mergers in Active Galaxy Nuclei*. 2023.

[38] M. Branchesi et al. "Science with the Einstein Telescope: a comparison of different designs." In: *Journal of Cosmology and Astroparticle Physics* 2023.07 (July 2023), p. 068. ISSN: 1475-7516. DOI: 10.1088/1475-7516/2023/07/068.

[39] R. Braun, A. Bonaldi, T. Bourke, E. Keane, and J. Wagg. "Anticipated Performance of the Square Kilometre Array – Phase 1 (SKA1)." In: *arXiv e-prints*, arXiv:1912.12699 (Dec. 2019), arXiv:1912.12699. DOI: 10.48550/arXiv.1912.12699.

[40] M. Breschi, A. Perego, S. Bernuzzi, W. Del Pozzo, V. Nedora, D. Radice, and D. Vescovi. "AT2017gfo: Bayesian inference and model selection of multi-component kilonovae and constraints on the neutron star equation of state." In: *MNRAS* 505.2 (2021), 1661–1677. ISSN: 1365-2966. DOI: 10.1093/mnras/stab1287.

[41] J. Buchner. "Nested sampling methods." In: *Statistics Surveys* 17.none (2023). DOI: 10.1214/23-ss144.

[42] M. Bulla. "POSSIS: predicting spectra, light curves, and polarization for multidimensional models of supernovae and kilonovae." In: *MNRAS* 489.4 (Nov. 2019), pp. 5037–5045. DOI: 10.1093/mnras/stz2495.

[43] M. Bulla, M. W. Coughlin, S. Dhawan, and T. Dietrich. "Multi-Messenger Constraints on the Hubble Constant through Combination of Gravitational Waves, Gamma-Ray Bursts and Kilonovae from Neutron Star Mergers." In: *Universe* 8.5 (2022), p. 289. ISSN: 2218-1997. DOI: 10.3390/universe8050289.

[44] M. Burgay et al. "An increased estimate of the merger rate of double neutron stars from observations of a highly relativistic system." In: *Nature* 426.6966 (Dec. 2003), pp. 531–533. DOI: 10.1038/nature02124.

[45] E. Burns. "Neutron star mergers and how to study them." In: *Living Reviews in Relativity* 23.1 (2020). ISSN: 1433-8351. DOI: 10.1007/s41114-020-00028-7.

[46] D. N. Burrows, D. Grupe, C. Kouveliotou, S. Patel, N. Gehrels, P. Meszaros, B. Zhang, and R. Wijers. "Chandra observation of GRB 050509b." In: *GRB Coordinates Network* 3415 (Jan. 2005), p. 1.

[47] C. D. Capano, I. Tews, S. M. Brown, B. Margalit, S. De, S. Kumar, D. A. Brown, B. Krishnan, and S. Reddy. "Stringent constraints on neutron-star radii from multimessenger observations and nuclear theory." In: *Nature Astronomy* 4.6 (2020), 625–632. ISSN: 2397-3366. DOI: 10.1038/s41550-020-1014-6.

[48] D. J. Champion, D. R. Lorimer, M. A. McLaughlin, J. M. Cordes, Z. Arzoumanian, J. M. Weisberg, and J. H. Taylor. "PSR J1829+2456: a relativistic binary pulsar." In: *MNRAS* 350.4 (June 2004), pp. L61–L65. DOI: 10.1111/j.1365-2966.2004.07862.x.

[49] H.-Y. Chen. "Systematic Uncertainty of Standard Sirens from the Viewing Angle of Binary Neutron Star Inspirals." In: *Phys. Rev. Lett.* 125 (20 2020), p. 201301. DOI: 10.1103/PhysRevLett.125.201301.

[50] H.-Y. Chen, M. Fishbach, and D. E. Holz. "A two per cent Hubble constant measurement from standard sirens within five years." In: *Nature* 562.7728 (2018), pp. 545–547. DOI: 10.1038/s41586-018-0606-0.

[51] H.-Y. Chen, C.-J. Haster, S. Vitale, W. M. Farr, and M. Isi. "A standard siren cosmological measurement from the potential GW190521 electromagnetic counterpart ZTF19abanrhr." In: *MNRAS* 513.2 (Apr. 2022), pp. 2152–2157. ISSN: 0035-8711. DOI: 10.1093/mnras/stac989.

[52] G. Chincarini et al. "Unveiling the origin of X-ray flares in gamma-ray bursts." In: *MNRAS* 406.4 (Aug. 2010), pp. 2113–2148. DOI: 10.1111/j.1365-2966.2010.17037.x.

[53] R. Ciolfi. "Collimated outflows from long-lived binary neutron star merger remnants." In: *MNRAS* 495.1 (June 2020), pp. L66–L70. DOI: 10.1093/mnrasl/slaa062.

[54] A. Colombo, O. S. Salafia, F. Gabrielli, G. Ghirlanda, B. Giacomazzo, A. Perego, and M. Colpi. "Multi-messenger Observations of Binary Neutron Star Mergers in the O4 Run." In: *ApJ* 937.2 (2022), p. 79. DOI: 10.3847/1538-4357/ac8d00.

[55] M. W. Coughlin, T. Dietrich, B. Margalit, and B. D. Metzger. "Multimessenger Bayesian parameter inference of a binary neutron star merger." In: *MNRAS Lett.* 489.1 (Aug. 2019), pp. L91–L96. ISSN: 1745-3925. DOI: 10.1093/mnrasl/slz133.

[56] M. W. Coughlin et al. "Constraints on the neutron star equation of state from AT2017gfo using radiative transfer simulations." In: *MNRAS* 480.3 (Aug. 2018), pp. 3871–3878. ISSN: 0035-8711. DOI: 10.1093/mnras/sty2174.

[57] D. A. Coulter et al. "Swope Supernova Survey 2017a (SSS17a), the optical counterpart to a gravitational wave source." In: *Science* 358.6370 (2017), pp. 1556–1558. DOI: 10.1126/science.aap9811.

[58] C. Cutler and E. Flanagan. "Gravitational waves from merging compact binaries: How accurately can one extract the binary's parameters from the inspiral waveform?" In: *Physical Review D* 49.6 (Mar. 1994), 2658–2697. ISSN: 0556-2821. DOI: 10.1103/physrevd.49.2658.

[59] P. D'Avanzo. "Short gamma-ray bursts: A review." In: *Journal of High Energy Astrophysics* 7 (2015). Swift 10 Years of Discovery, a novel approach to Time Domain Astronomy, pp. 73–80. ISSN: 2214-4048. DOI: https://doi.org/10.1016/j.jheap.2015.07.002.

[60] L. Desjardins. *Introduction to the Hubble Space Telescope Data Handbooks, Version 9.0*. Baltimore: STScI, 2019.

[61] T. Dietrich, S. Bernuzzi, and W. Tichy. "Closed-form tidal approximants for binary neutron star gravitational waveforms constructed from high-resolution numerical relativity simulations." In: *Phys. Rev. D* 96 (12 2017), p. 121501. DOI: 10.1103/PhysRevD.96.121501.

[62] T. Dietrich, M. W. Coughlin, P. T. H. Pang, M. Bulla, J. Heinzel, L. Issa, I. Tews, and S. Antier. "Multimessenger constraints on the neutron-star equation of state and the Hubble constant." In: *Science* 370.6523 (2020), pp. 1450–1453. DOI: 10.1126/science.abb4317.

[63] T. Dietrich, A. Samajdar, S. Khan, N. K. Johnson-McDaniel, R. Dudi, and W. Tichy. "Improving the NRTidal model for binary neutron star systems." In: *Phys. Rev. D* 100 (4 2019), p. 044003. DOI: 10.1103/PhysRevD.100.044003.

[64] T. Dietrich et al. "Matter imprints in waveform models for neutron star binaries: Tidal and self-spin effects." In: *Phys. Rev. D* 99.2 (2019). ISSN: 2470-0029. DOI: 10.1103/physrevd.99.024029.

[65] G Drouart and T Falkendal. "Mr-Moose: an advanced SED-fitting tool for heterogeneous multi-wavelength data sets." In: *MNRAS* 477.4 (Apr. 2018), pp. 4981–5000. ISSN: 0035-8711. DOI: 10.1093/mnras/sty831.

[66] H. van Eerten, K. Leventis, Z. Meliani, R. A. M. J. Wijers, and R. Keppens. "Gamma-ray burst afterglows from transrelativistic blast wave simulations." In: *MNRAS* 403.1 (Mar. 2010), pp. 300–316. ISSN: 0035-8711. DOI: 10.1111/j.1365-2966.2009.16109.x.

[67] H. van Eerten and G. Ryan. *Scaling relations for gamma-ray burst afterglow light curves and centroid motion independent of jet structure and dynamics*. 2023.

[68] H. van Eerten, W. Zhang, and A. MacFadyen. "Off-axis gamma-ray burst afterglow modeling based on a two-dimensional axisymmetric hydrodynamics simulation." In: *Astrophysical Journal* 722.1 (2010), pp. 235–247. DOI: 10.1088/0004-637x/722/1/235.

[69] D. Eichler, M. Livio, T. Piran, et al. "Nucleosynthesis, neutrino bursts and gamma-rays from coalescing neutron stars." In: *Nature* 340 (July 1989), pp. 126–128. DOI: 10.1038/340126a0.

[70] A. Einstein. In: *Sitzungsber. Preuss. Akad. Wiss.* 688.1 (1916).

[71] A. R. Escorial et al. *The Jet Opening Angle and Event Rate Distributions of Short Gamma-ray Bursts from Late-time X-ray Afterglows*. 2022.

[72] P. A. Evans et al. "Swift and NuSTAR observations of GW170817: Detection of a blue kilonova." In: *Science* 358.6370 (2017), pp. 1565–1570. DOI: 10.1126/science.aap9580.

[73] S. Fairhurst. "Triangulation of gravitational wave sources with a network of detectors." In: *New Journal of Physics* 11.12, 123006 (Dec. 2009), p. 123006. DOI: 10.1088/1367-2630/11/12/123006.

[74] S. M. Feeney, H. V. Peiris, S. M. Nissanke, and D. J. Mortlock. "Prospects for Measuring the Hubble Constant with Neutron-Star–Black-Hole Mergers." In: *Physical Review Letters* 126.17 (2021). DOI: 10.1103/physrevlett.126.171102.

[75] L. S. Finn. "Detection, measurement, and gravitational radiation." In: *Phys. Rev. D* 46 (12 1992), pp. 5236–5249. DOI: 10.1103/PhysRevD.46.5236.

[76] L. S. Finn and D. F. Chernoff. "Observing binary inspiral in gravitational radiation: One interferometer." In: *Phys. Rev. D* 47 (6 1993), pp. 2198–2219. DOI: 10.1103/PhysRevD.47.2198.

[77] G. J. Fishman and C. A. Meegan. "Gamma-Ray Bursts." In: *ARA&A* 33 (Jan. 1995), pp. 415–458. DOI: 10.1146/annurev.aa.33.090195.002215.

[78] G. J. Fishman et al. "The First BATSE Gamma-Ray Burst Catalog." In: *ApJ Supplement* 92 (May 1994), p. 229. DOI: 10.1086/191968.

[79] W. Fong and E. Berger. "The Locations of Short Gamma-Ray Bursts as Evidence for Compact Object Binary Progenitors." In: *ApJ* 776.1, 18 (Oct. 2013), p. 18. DOI: 10.1088/0004-637X/776/1/18.

[80] W. Fong, E. Berger, and D. B. Fox. "Hubble Space Telescope Observations of Short Gamma-Ray Burst Host Galaxies: Morphologies, Offsets, and Local Environments." In: *ApJ* 708.1 (Jan. 2010), pp. 9–25. DOI: 10.1088/0004-637X/708/1/9.

[81] W. Fong, E. Berger, R. Margutti, and B. A. Zauderer. "A Decade of Short-duration Gamma-Ray Burst Broadband Afterglows: Energetics, Circumburst Densities, and Jet Opening Angles." In: *ApJ* 815.2, 102 (Dec. 2015), p. 102. DOI: 10.1088/0004-637X/815/2/102.

[82] W. Fong et al. "The Optical Afterglow of GW170817: An Off-axis Structured Jet and Deep Constraints on a Globular Cluster Origin." In: *ApJ* 883.1 (2019), p. L1. DOI: 10.3847/2041-8213/ab3d9e.

[83] W. Fong et al. "Short GRB Host Galaxies. I. Photometric and Spectroscopic Catalogs, Host Associations, and Galactocentric Offsets." In: *ApJ* 940.1 (2022), p. 56. DOI: 10.3847/1538-4357/ac91d0.

[84] D. Foreman-Mackey. "corner.py: Scatterplot matrices in Python." In: *JOSS* 1.2 (2016), p. 24. DOI: 10.21105/joss.00024.

[85] D. B. Fox et al. "The afterglow of GRB 050709 and the nature of the short-hard gamma-ray bursts." In: *Nature* 437 (Oct. 2005), pp. 845–850. DOI: 10.1038/nature04189.

[86] T. J. Galama et al. "An unusual supernova in the error box of the γ-ray burst of 25 April 1998." In: *Nature* 395.6703 (Oct. 1998), pp. 670–672. DOI: 10.1038/27150.

[87] N. Gehrels, C. Sarazin, P. O'Brien, et al. "A short gamma-ray burst apparently associated with an elliptical galaxy at redshift z = 0.225." In: *Nature* 437 (Oct. 2005), pp. 851–854. DOI: 10.1038/nature04142.

[88] N. Gehrels et al. "A new γ-ray burst classification scheme from GRB060614." In: *Nat* 444.7122 (Dec. 2006), pp. 1044–1046. DOI: 10.1038/nature05376.

[89] M. E. Gertsenshtein and V. I. Pustovoit. "On the Detection of Low Frequency Gravitational Waves." In: *Sov. Phys. JETP* 16 (1962), p. 433.

[90] G. Ghirlanda, G. Ghisellini, and A. Celotti. "The spectra of short gamma-ray bursts." In: *A&A* 422.3 (2004), pp. L55–L58. DOI: 10.1051/0004-6361:20048008.

[91] G. Ghirlanda, L. Nava, G. Ghisellini, A. Celotti, and C. Firmani. "Short versus long gamma-ray bursts: spectra, energetics, and luminosities." In: *A&A* 496.3 (2009), pp. 585–595. DOI: 10.1051/0004-6361/200811209.

[92] G. Ghirlanda et al. "Short gamma-ray bursts at the dawn of the gravitational wave era." In: *A& A* 594 (2016), A84. DOI: 10.1051/0004-6361/201628993.

[93] G. Ghirlanda et al. "Compact radio emission indicates a structured jet was produced by a binary neutron star merger." In: *Science* 363.6430 (2019), pp. 968–971. DOI: 10.1126/science.aau8815.

[94] G. Gianfagna, L. Piro, F. Pannarale, H. Van Eerten, F. Ricci, and G. Ryan. "Potential biases and prospects for the Hubble constant estimation via electromagnetic and gravitational-wave joint analyses." In: *Monthly Notices of the Royal Astronomical Society* 528.2 (Jan. 2024), pp. 2600–2613. ISSN: 0035-8711. DOI: 10.1093/mnras/stae198.

[95] G. Gianfagna, L. Piro, F. Pannarale, H. Van Eerten, F. Ricci, G. Ryan, and E. Troja. "Joint analysis of gravitational-wave and electromagnetic data of mergers: breaking an afterglow model degeneracy in GW170817 and in future events." In: *MNRAS* 523.3 (June 2023), pp. 4771–4784. ISSN: 0035-8711. DOI: 10.1093/mnras/stad1728.

[96] A. Goldstein et al. "An Ordinary Short Gamma-Ray Burst with Extraordinary Implications: Fermi -GBM Detection of GRB 170817A." In: *Astrophysical Journal* 848.2 (2017), p. L14. DOI: 10.3847/2041-8213/aa8f41.

[97] A. Goldstein et al. "Evaluation of Automated Fermi GBM Localizations of Gamma-Ray Bursts." In: *The Astrophysical Journal* 895.1 (2020), p. 40. DOI: 10.3847/1538-4357/ab8bdb.

[98] V. Z. Golkhou and N. R. Butler. "UNCOVERING THE INTRINSIC VARIABILITY OF GAMMA-RAY BURSTS." In: *ApJ* 787.1 (2014), p. 90. DOI: 10.1088/0004-637X/787/1/90.

[99] B. P. Gompertz, P. T. O'Brien, and G. A. Wynn. "Magnetar powered GRBs: explaining the extended emission and X-ray plateau of short GRB light curves." In: *MNRAS* 438.1 (Dec. 2013), pp. 240–250. ISSN: 0035-8711. DOI: 10.1093/mnras/stt2165.

[100] J. Goodman. "Are gamma-ray bursts optically thick?" In: *ApJ Letters* 308 (Sept. 1986), p. L47. DOI: 10.1086/184741.

[101] O. Gottlieb, S. Moseley, T. Ramirez-Aguilar, A. Murguia-Berthier, M. Liska, and A. Tchekhovskoy. "On the Jet–Ejecta Interaction in 3D GRMHD Simulations of a Binary Neutron Star Merger Aftermath." In: *Apj Lett* 933.1 (June 2022), p. L2. ISSN: 2041-8213. DOI: 10.3847/2041-8213/ac7728.

[102] T. Govreen-Segal and E. Nakar. "Analytic model for off-axis GRB afterglow images – geometry measurement and implications for measuring H_0." In: *MNRAS* 524.1 (2023), pp. 403–425. DOI: 10.1093/mnras/stad1628.

[103] J. Granot and A. Loeb. "Radio Imaging of Gamma-Ray Burst Jets in Nearby Supernovae." In: *ApJ* 593.2 (2003), p. L81. DOI: 10.1086/378262.

[104] J. Granot and R. Sari. "The Shape of Spectral Breaks in Gamma-Ray Burst Afterglows." In: *ApJ* 568.2 (2002), p. 820. DOI: 10.1086/338966.

[105] C. Guidorzi et al. "Improved Constraints on Ho from a Combined Analysis of Gravitational-wave and Electromagnetic Emission from GW170817." In: *ApJ* 851.2 (2017), p. L36. DOI: 10.3847/2041-8213/aaa009.

[106] P. W. Guilbert, A. C. Fabian, and M. J. Rees. "Spectral and variability constraints on compact sources." In: *MNRAS* 205 (Nov. 1983), pp. 593–603. DOI: 10.1093/mnras/205.3.593.

[107] A. Hajela et al. "Two Years of Nonthermal Emission from the Binary Neutron Star Merger GW170817: Rapid Fading of the Jet Afterglow and First Constraints on the Kilonova Fastest Ejecta." In: *ApJ* 886.1 (2019), p. L17. DOI: 10.3847/2041-8213/ab5226.

[108] A. Hajela et al. "Evidence for X-Ray Emission in Excess to the Jet-afterglow Decay 3.5 yr after the Binary Neutron Star Merger GW 170817: A New Emission Component." In: *ApJ Lett.* 927.1 (2022), p. L17. DOI: 10.3847/2041-8213/ac504a.

[109] G. Hallinan et al. "A radio counterpart to a neutron star merger." In: *Science* 358.6370 (2017), pp. 1579–1583. DOI: 10.1126/science.aap9855.

[110] M. Hannam, P. Schmidt, A. Bohé, L. Haegel, S. Husa, F. Ohme, G. Pratten, and M. Pürrer. "Simple Model of Complete Precessing Black-Hole-Binary Gravitational Waveforms." In: *Phys. Rev. Lett.* 113 (15 2014), p. 151101. DOI: 10.1103/PhysRevLett.113.151101.

[111] D. Hartmann. "Afterglows from the largest explosions in the universe." In: *Proceedings of the National Academy of Sciences of the United States of America* 96 (May 1999), pp. 4752–5. DOI: 10.1073/pnas.96.9.4752.

[112] S. W. Hawking and W. Israel. *Three Hundred Years of Gravitation*. 1989.

[113] R. C. Hilborn. "Does GW170814 rule out non-tensorial gravitational wave polarization?" In: *Classical and Quantum Gravity* 38.8 (Mar. 2021), p. 085003. ISSN: 1361-6382. DOI: 10.1088/1361-6382/abe9f4.

[114] T. Hinderer et al. "Distinguishing the nature of comparable-mass neutron star binary systems with multimessenger observations: GW170817 case study." In: *Phys. Rev. D* 100 (6 2019), p. 063021. DOI: 10.1103/PhysRevD.100.063021.

[115] J. Hjorth et al. "The optical afterglow of the short Gamma-ray burst GRB 050709." In: *Nature* 437 (Oct. 2005), pp. 859–861. DOI: 10.1038/nature04174.

[116] J. Hjorth and J. S. Bloom. *The Gamma-Ray Burst - Supernova Connection*. 2011.

[117] J. Hjorth and J. S. Bloom. "The GRB–supernova connection." In: *Gamma-ray Bursts*. Ed. by C. Kouveliotou, R. A. M. J. Wijers, and S. Woosley. Cambridge Astrophysics. Cambridge University Press, 2012, 169–190. DOI: 10.1017/CBO9780511980336.010.

[118] J. Hjorth, A. J. Levan, N. R. Tanvir, J. D. Lyman, R. Wojtak, S. L. Schrøder, I. Mandel, C. Gall, and S. H. Bruun. "The Distance to NGC 4993: The Host Galaxy of the Gravitational-wave Event GW170817." In: *ApJl* 848.2, L31 (Oct. 2017), p. L31. DOI: 10.3847/2041-8213/aa9110.

[119] D. E. Holz and S. A. Hughes. "Using Gravitational-Wave Standard Sirens." In: *ApJ* 629.1 (2005), pp. 15–22. DOI: 10.1086/431341.

[120] K. Hotokezaka, K. Kiuchi, K. Kyutoku, T. Muranushi, Y. ichiro Sekiguchi, M. Shibata, and K. Taniguchi. "Remnant massive neutron stars of binary neutron star mergers: Evolution process and gravitational waveform." In: *Phys. Rev. D* 88.4 (2013). DOI: 10.1103/physrevd.88.044026.

[121] K. Hotokezaka, E. Nakar, O. Gottlieb, S. Nissanke, K. Masuda, G. Hallinan, K. P. Mooley, and A. T. Deller. "A Hubble constant measurement from superluminal motion of the jet in GW170817." In: *Nature Astronomy* 3 (2018), pp. 940–944.

[122] Y.-J. Huang et al. "Orphan GRB Afterglow Searches with the Pan-STARRS1 COSMOS Survey." In: *ApJ* 897.1, 69 (July 2020), p. 69. DOI: 10.3847/1538-4357/ab8f9a.

[123] D. Kasen, B. Metzger, J. Barnes, E. Quataert, and E. Ramirez-Ruiz. "Origin of the heavy elements in binary neutron-star mergers from a gravitational-wave event." In: *Nature* 551.7678 (2017), pp. 80–84. DOI: 10.1038/nature24453.

[124] R. E. Kass and A. E. Raftery. "Bayes Factors." In: *Journal of the American Statistical Association* 90.430 (1995), pp. 773–795. DOI: 10.1080/01621459.1995.10476572.

[125] J. I. Katz. "Two Populations and Models of Gamma-Ray Bursts." In: *ApJ* 422 (Feb. 1994), p. 248. DOI: 10.1086/173723.

[126] J. I. Katz and T. Piran. "Persistent Counterparts to Gamma-Ray Bursts." In: *ApJ* 490.2 (1997), p. 772. DOI: 10.1086/304913.

[127] R. W. Klebesadel, I. B. Strong, and R. A. Olson. "Observations of Gamma-Ray Bursts of Cosmic Origin." In: *ApJ Letters* 182 (June 1973), p. L85. DOI: 10.1086/181225.

[128] S. Kobayashi, T. Piran, and R. Sari. "Can Internal Shocks Produce the Variability in Gamma-Ray Bursts?" In: *ApJ* 490 (Nov. 1997), p. 92. DOI: 10.1086/512791.

[129] C. Kouveliotou, C. A. Meegan, G. J. Fishman, N. P. Bhat, M. S. Briggs, T. M. Koshut, W. S. Paciesas, and G. N. Pendleton. "Identification of Two Classes of Gamma-Ray Bursts." In: *ApJ Letters* 413 (Aug. 1993), p. L101. DOI: 10.1086/186969.

[130] P. Kumar and A. Panaitescu. "Afterglow Emission from Naked Gamma-Ray Bursts." In: *ApJ* 541.2 (Oct. 2000), L51–L54. ISSN: 0004-637X. DOI: 10.1086/312905.

[131] D. Lazzati, E. Ramirez-Ruiz, and G. Ghisellini. "Possible detection of hard X-ray afterglows of short Γ-ray bursts." In: *A& A* 379.3 (2001), pp. L39–L43. DOI: 10.1051/0004-6361:20011485.

[132] D. Lazzati, B. J. Morsony, and M. C. Begelman. "Short duration gamma-ray bursts from off-axis collapsars." In: *ApJ* 717.1 (2010), pp. 239–244. DOI: 10.1088/0004-637x/717/1/239.

[133] A. Le Tiec and J. Novak. *Theory of Gravitational Waves*. 2016.

[134] C. N. Leibler and E. Berger. "The Stellar Ages and Masses of Short Gamma-ray Burst Host Galaxies: Investigating the Progenitor Delay Time Distribution and the Role of Mass and Star Formation in the Short Gamma-ray Burst Rate." In: *ApJ* 725.1 (Dec. 2010), pp. 1202–1214. DOI: 10.1088/0004-637X/725/1/1202.

[135] A. J. Levan et al. "Heavy-element production in a compact object merger observed by JWST." In: *Nature* 626.8000 (Oct. 2023), 737–741. ISSN: 1476-4687. DOI: 10.1038/s41586-023-06759-1.

[136] A. Levan et al. "A long-duration gamma-ray burst of dynamical origin from the nucleus of an ancient galaxy." In: (2022). DOI: 10.21203/rs.3.rs-2298504/v1.

[137] L.-X. Li and B. Paczyński. "Transient Events from Neutron Star Mergers." In: *ApJ Letters* 507.1 (Nov. 1998), pp. L59–L62. DOI: 10.1086/311680.

[138] V. M. Lipunov et al. "The First Detection of an Orphan Burst at the Rise Phase." In: *Astronomy Letters* 48.11 (Nov. 2022), pp. 623–635. DOI: 10.1134/S1063773722110093.

[139] A. I. MacFadyen and S. E. Woosley. "Collapsars: Gamma-Ray Bursts and Explosions in "Failed Supernovae"." In: *ApJ* 524.1 (Oct. 1999), pp. 262–289. DOI: 10.1086/307790.

[140] G. A. MacLachlan, A. Shenoy, E. Sonbas, K. S. Dhuga, B. E. Cobb, T. N. Ukwatta, D. C. Morris, A. Eskandarian, L. C. Maximon, and W. C. Parke. "Minimum variability time-scales of long and short GRBs." In: *MNRAS* 432.2 (2013), pp. 857–865. DOI: 10.1093/mnras/stt241.

[141] S. Makhathini et al. "The Panchromatic Afterglow of GW170817: The Full Uniform Data Set, Modeling, Comparison with Previous Results, and Implications." In: *ApJ* 922.2, 154 (Dec. 2021), p. 154. DOI: 10.3847/1538-4357/ac1ffc.

[142] R. Margutti, G. Chincarini, J. Granot, C. Guidorzi, E. Berger, M. G. Bernardini, N. Gehrels, A. M. Soderberg, M. Stamatikos, and E. Zaninoni. "X-ray flare candidates in short gamma-ray bursts." In: *MNRAS* 417.3 (Nov. 2011), pp. 2144–2160. DOI: 10.1111/j.1365-2966.2011.19397.x.

[143] R. Margutti et al. "The prompt-afterglow connection in gamma-ray bursts: a comprehensive statistical analysis of Swift X-ray light curves." In: *MNRAS* 428.1 (Oct. 2012), pp. 729–742. ISSN: 0035-8711. DOI: 10.1093/mnras/sts066.

[144] R. Margutti et al. "The Electromagnetic Counterpart of the Binary Neutron Star Merger LIGO/Virgo GW170817. V. Rising X-Ray Emission from an Off-axis Jet." In: *ApJ* 848.2 (2017), p. L20. DOI: 10.3847/2041-8213/aa9057.

[145] R. Margutti et al. "The Binary Neutron Star Event LIGO/Virgo GW170817 160 Days after Merger: Synchrotron Emission across the Electromagnetic Spectrum." In: *Astrophysical Journal Letters* 856.1, L18 (Mar. 2018), p. L18. DOI: 10.3847/2041-8213/aab2ad.

[146] S. Mastrogiovanni, R. Duque, E. Chassande-Mottin, F. Daigne, and R. Mochkovitch. "The potential role of binary neutron star merger afterglows in multimessenger cosmology." In: *A&A* 652, A1 (Aug. 2021), A1. DOI: 10.1051/0004-6361/202040229.

[147] A. Mei et al. "Gigaelectronvolt emission from a compact binary merger." In: *Nature* 612.7939 (2022), pp. 236–239. DOI: 10.1038/s41586-022-05404-7.

[148] P Meszaros. "Gamma-ray bursts." In: *Reports on Progress in Physics* 69.8 (2006), pp. 2259–2321. DOI: 10.1088/0034-4885/69/8/r01.

[149] P. Meszaros, M. J. Rees, and H. Papathanassiou. "Spectral Properties of Blast-Wave Models of Gamma-Ray Burst Sources." In: *ApJ* 432 (Sept. 1994), p. 181. DOI: 10.1086/174559.

[150] B. D. Metzger, G. Martínez-Pinedo, S. Darbha, E. Quataert, A. Arcones, D. Kasen, R. Thomas, P. Nugent, I. V. Panov, and N. T. Zinner. "Electromagnetic counterparts of compact object mergers powered by the radioactive decay of r-process nuclei." In: *MNRAS* 406.4 (Aug. 2010), pp. 2650–2662. DOI: 10.1111/j.1365-2966.2010.16864.x.

[151] B. D. Metzger, E. Quataert, and T. A. Thompson. "Short-duration gamma-ray bursts with extended emission from protomagnetar spin-down." In: *MNRAS* 385.3 (Mar. 2008), pp. 1455–1460. ISSN: 0035-8711. DOI: 10.1111/j.1365-2966.2008.12923.x.

[152] J. MichałowskI et al. "The second-closest gamma-ray burst: sub-luminous GRB 111005A with no supernova in a super-solar metallicity environment." In: *A& A* 616, A169 (Sept. 2018), A169. DOI: 10.1051/0004-6361/201629942.

[153] A. A. Michelson and E. W. Morley. "On the relative motion of the Earth and the luminiferous ether." In: *American Journal of Science* (1887).

[154] K. P. Mooley, A. T. Deller, O. Gottlieb, E. Nakar, G. Hallinan, S. Bourke, D. A. Frail, A. Horesh, A. Corsi, and K. Hotokezaka. "Superluminal motion of a relativistic jet in the neutron-star merger GW170817." In: *Nature* 561.7723 (2018), 355–359. ISSN: 1476-4687. DOI: 10.1038/s41586-018-0486-3.

[155] K. P. Mooley, J. Anderson, and W. Lu. "Optical superluminal motion measurement in the neutron-star merger GW170817." In: *Nature* 610.7931 (2022), pp. 273–276. DOI: 10.1038/s41586-022-05145-7.

[156] G. E. Moss, L. R. Miller, and R. L. Forward. "Photon-Noise-Limited Laser Transducer for Gravitational Antenna." In: *Appl. Opt.* 10.11 (1971), pp. 2495–2498. DOI: 10.1364/AO.10.002495.

[157] E. Nakar and T. Piran. "Detectable radio flares following gravitational waves from mergers of binary neutron stars." In: *Nature* 478.7367 (2011), 82–84. ISSN: 1476-4687. DOI: 10.1038/nature10365.

[158] E. Nakar and T. Piran. "Afterglow Constraints on the Viewing Angle of Binary Neutron Star Mergers and Determination of the Hubble Constant." In: *ApJ* 909.2 (2021), p. 114. DOI: 10.3847/1538-4357/abd6cd.

[159] R. Narayan, B. Paczynski, and T. Piran. "Gamma-Ray Bursts as the Death Throes of Massive Binary Stars." In: *ApJ Letters* 395 (Aug. 1992), p. L83. DOI: 10.1086/186493.

[160] M. Nicholl, B. Margalit, P. Schmidt, G. P. Smith, E. J. Ridley, and J. Nuttall. "Tight multimessenger constraints on the neutron star equation of state from GW170817 and a forward model for kilonova light-curve synthesis." In: *MNRAS* 505.2 (2021), 3016–3032. ISSN: 1365-2966. DOI: 10.1093/mnras/stab1523.

[161] C. Nicolaou, O. Lahav, P. Lemos, W. Hartley, and J. Braden. "The impact of peculiar velocities on the estimation of the Hubble constant from gravitational wave standard sirens." In: *MNRAS* 495.1 (Apr. 2020), 90–97. ISSN: 1365-2966. DOI: 10.1093/mnras/staa1120.

[162] S. Nissanke, D. E. Holz, S. A. Hughes, N. Dalal, and J. L. Sievers. "Exploring Short Gamma-ray Bursts as Gravitational-wave Standard Sirens." In: *ApJ* 725.1 (Dec. 2010), pp. 496–514. DOI: 10.1088/0004-637X/725/1/496.

[163] J. P. Norris, G. F. Marani, and J. T. Bonnell. "Connection between Energy-dependent Lags and Peak Luminosity in Gamma-Ray Bursts." In: *ApJ* 534.1 (2000), p. 248. DOI: 10.1086/308725.

[164] J. P. Norris, N. Gehrels, and J. D. Scargle. "HETEROGENEITY IN SHORT GAMMA-RAY BURSTS." In: *ApJ* 735.1 (2011), p. 23. DOI: 10.1088/0004-637X/735/1/23.

[165] J. A. Nousek et al. "Evidence for a Canonical Gamma-Ray Burst Afterglow Light Curve in the Swift XRT Data." In: *ApJ* 642.1 (May 2006), pp. 389–400. DOI: 10.1086/500724.

[166] B. O'Connor and E. Troja. "Continued Chandra monitoring of GW170817 at 4.8 yr post-merger." In: *GRB Coordinates Network* 32065 (May 2022), p. 1.

[167] B. Paczynski. "Gamma-ray bursters at cosmological distances." In: *ApJ Letters* 308 (Sept. 1986), pp. L43–L46. DOI: 10.1086/184740.

[168] B. Paczynski and G. Xu. "Neutrino Bursts from Gamma-Ray Bursts." In: *ApJ* 427 (June 1994), p. 708. DOI: 10.1086/174178.

[169] A. Palmese, R. Kaur, A. Hajela, R. Margutti, A. McDowell, and A. MacFadyen. *A standard siren measurement of the Hubble constant using GW170817 and the latest observations of the electromagnetic counterpart afterglow*. 2023.

[170] A. Panaitescu and P. Kumar. "Analytic Light Curves of Gamma-Ray Burst Afterglows: Homogeneous versus Wind External Media." In: *ApJ* 543.1 (Nov. 2000), 66–76. ISSN: 1538-4357. DOI: 10.1086/317090.

[171] A. Panaitescu, P. Kumar, and R. Narayan. "Observational Prospects for Afterglows of Short-Duration Gamma-Ray Bursts." In: *ApJ* 561.2 (2001), p. L171. DOI: 10.1086/324678.

[172] B. Patricelli, M. G. Bernardini, M. Mapelli, P. D'Avanzo, F. Santoliquido, G. Cella, M. Razzano, and E. Cuoco. "Prospects for multimessenger detection of binary neutron star mergers in the fourth LIGO–Virgo–KAGRA observing run." In: *MNRAS* 513.3 (2022), pp. 4159–4168. DOI: 10.1093/mnras/stac1167.

[173] P. Petrov, L. P. Singer, M. W. Coughlin, V. Kumar, M. Almualla, S. Anand, M. Bulla, T. Dietrich, F. Foucart, and N. Guessoum. "Data-driven Expectations for Electromagnetic Counterpart Searches Based on LIGO/Virgo Public Alerts." In: *ApJ* 924.2 (2022), p. 54. DOI: 10.3847/1538-4357/ac366d.

[174] T. Piran. "Gamma-ray bursts and the fireball model." In: *Phys. Rep.* 314.6 (June 1999), pp. 575–667. DOI: 10.1016/S0370-1573(98)00127-6.

[175] T. Piran. "The physics of gamma-ray bursts." In: *Reviews of Modern Physics* 76.4 (2005), 1143–1210. ISSN: 1539-0756. DOI: 10.1103/revmodphys.76.1143.

[176] L. Piro et al. "Iron line signatures in X-ray afterglows of GRB by BeppoSAX." In: *A&AS* 138 (Sept. 1999), pp. 431–432. DOI: 10.1051/aas:1999296.

[177] L Piro et al. "A long-lived neutron star merger remnant in GW170817: constraints and clues from X-ray observations." In: *MNRAS* 483.2 (Nov. 2018), pp. 1912–1921. ISSN: 0035-8711. DOI: 10.1093/mnras/sty3047.

[178] L. Piro et al. "Athena synergies in the multi-messenger and transient universe." In: *Experimental Astronomy* 54 (Sept. 2022). DOI: 10.1007/s10686-022-09865-6.

[179] Planck Collaboration et al. "Planck2018 results: VI. Cosmological parameters." In: *A&A* 641 (Sept. 2020), A6. ISSN: 1432-0746. DOI: 10.1051/0004-6361/201833910.

[180] E. Poisson and C. M. Will. "Gravitational waves from inspiraling compact binaries: Parameter estimation using second-post-Newtonian waveforms." In: *Phys. Rev. D* 52 (2 1995), pp. 848–855. DOI: 10.1103/PhysRevD.52.848.

[181] G. Raaijmakers, S. K. Greif, K. Hebeler, T. Hinderer, S. Nissanke, A. Schwenk, T. E. Riley, A. L. Watts, J. M. Lattimer, and W. C. G. Ho. "Constraints on the Dense Matter Equation of State and Neutron Star Properties from NICER's Mass–Radius Estimate of PSR J0740+6620 and Multimessenger Observations." In: *ApJ Lett.* 918.2 (2021), p. L29. ISSN: 2041-8213. DOI: 10.3847/2041-8213/ac089a.

[182] G. Raaijmakers et al. "The Challenges Ahead for Multimessenger Analyses of Gravitational Waves and Kilonova: A Case Study on GW190425." In: *ApJ* 922.2 (2021), p. 269. ISSN: 1538-4357. DOI: 10.3847/1538-4357/ac222d.

[183] J. L. Racusin, E. W. Liang, D. N. Burrows, A. Falcone, T. Sakamoto, B. B. Zhang, B. Zhang, P. Evans, and J. Osborne. "JET BREAKS AND ENERGETICS OF Swift GAMMA-RAY BURST X-RAY AFTERGLOWS." In: *ApJ* 698.1 (2009), p. 43. DOI: 10.1088/0004-637X/698/1/43.

[184] D. Radice and L. Dai. "Multimessenger parameter estimation of GW170817." In: *The European Physical Journal A* 55.4 (2019). ISSN: 1434-601X. DOI: 10.1140/epja/i2019-12716-4.

[185] D. Radice, A. Perego, F. Zappa, and S. Bernuzzi. "GW170817: Joint Constraint on the Neutron Star Equation of State from Multimessenger Observations." In: *ApJ* 852.2 (2018), p. L29. DOI: 10.3847/2041-8213/aaa402.

[186] J. S. Read, L. Baiotti, J. D. E. Creighton, J. L. Friedman, B. Giacomazzo, K. Kyutoku, C. Markakis, L. Rezzolla, M. Shibata, and K. Taniguchi. "Matter effects on binary neutron star waveforms." In: *Phys. Rev. D* 88 (4 2013), p. 044042. DOI: 10.1103/PhysRevD.88.044042.

[187] M. J. Rees and P. Meszaros. "Relativistic fireballs - Energy conversion and time-scales." In: *MNRAS* 258 (Sept. 1992), p. 41. DOI: 10.1093/mnras/258.1.41P.

[188] M. J. Rees and P. Meszaros. "Unsteady Outflow Models for Cosmological Gamma-Ray Bursts." In: *ApJ Letters* 430 (Aug. 1994), p. L93. DOI: 10.1086/187446.

[189] J. Ren, D.-B. Lin, L.-L. Zhang, K. Wang, X.-Y. Li, X.-G. Wang, and E.-W. Liang. "Constraining the Jet Launching Time of GRB 170817A by Utilizing the Baryon Loading." In: *ApJ* 901.2, L26 (Oct. 2020), p. L26. DOI: 10.3847/2041-8213/abb672.

[190] L. Rezzolla, B. Giacomazzo, L. Baiotti, J. Granot, C. Kouveliotou, and M. A. Aloy. "The missing link: merging neutron stars naturally produce jet-like structures and can power short gamma-ray bursts." In: *Astrophysical Journal* 732.1 (2011), p. L6. DOI: 10.1088/2041-8205/732/1/l6.

[191] J. Rhoads. "How to tell a jet from a balloon: A proposed test for beaming in gamma-ray bursts." English (US). In: *Astrophysical Journal* 487.1 PART II (1997), pp. L1–L4. ISSN: 0004-637X. DOI: 10.1086/310876.

[192] A. G. Riess, S. Casertano, W. Yuan, L. M. Macri, and D. Scolnic. "Large Magellanic Cloud Cepheid Standards Provide a 1% Foundation for the Determination of the Hubble Constant and Stronger Evidence for Physics beyond ΛCDM." In: *ApJ* 876.1, 85 (May 2019), p. 85. DOI: 10.3847/1538-4357/ab1422.

[193] J. D. Romano and N. J. Cornish. "Detection methods for stochastic gravitational-wave backgrounds: a unified treatment." In: *Living Rev. in Relativ.* 20.1 (2017). ISSN: 1433-8351. DOI: 10.1007/s41114-017-0004-1.

[194] I. M. Romero-Shaw et al. "Bayesian inference for compact binary coalescences with bilby: validation and application to the first LIGO–Virgo gravitational-wave transient catalogue." In: *MNRAS* 499.3 (2020), 3295–3319. ISSN: 1365-2966. DOI: 10.1093/mnras/staa2850.

[195] S. Ronchini, M. Branchesi, G. Oganesyan, B. Banerjee, U. Dupletsa, G. Ghirlanda, J. Harms, M. Mapelli, and F. Santoliquido. "Perspectives for multimessenger astronomy with the next generation of gravitational-wave detectors and high-energy satellites." In: *A & A* 665 (Sept. 2022), A97. ISSN: 1432-0746. DOI: 10.1051/0004-6361/202243705.

[196] Rossi, A. et al. "A quiescent galaxy at the position of the long GRB 050219A." In: *A&A* 572 (2014), A47. DOI: 10.1051/0004-6361/201423865.

[197] G. Ryan, H. van Eerten, L. Piro, and E. Troja. "Gamma-Ray Burst Afterglows in the Multimessenger Era: Numerical Models and Closure Relations." In: *ApJ* 896.2 (2020), p. 166. DOI: 10.3847/1538-4357/ab93cf.

[198] G. Ryan, H. van Eerten, E. Troja, L. Piro, B. O'Connor, and R. Ricci. *Modelling of Long-Term Afterglow Counterparts to Gravitational Wave Events: The Full View of GRB 170817A*. Oct. 2023.

[199] G. B. Rybicki and A. P. Lightman. *Radiative processes in astrophysics*. 1979.

[200] O. S. Salafia, C. Barbieri, S. Ascenzi, and M. Toffano. "Gamma-ray burst jet propagation, development of angular structure, and the luminosity function." In: *A&A* 636 (2020), A105. DOI: 10.1051/0004-6361/201936335.

[201] O. S. Salafia, G. Ghisellini, A. Pescalli, G. Ghirlanda, and F. Nappo. "Structure of gamma-ray burst jets: intrinsic versus apparent properties." In: *MNRAS* 450.4 (May 2015), 3549–3558. ISSN: 0035-8711. DOI: 10.1093/mnras/stv766.

[202] O. S. Salafia and G. Ghirlanda. "The Structure of Gamma Ray Burst Jets." In: *Galaxies* 10.5 (2022). ISSN: 2075-4434. DOI: 10.3390/galaxies10050093.

[203] R. Salvaterra, B. Devecchi, M. Colpi, and P. D'Avanzo. "On the offset of short gamma-ray bursts." In: *MNRAS* 406.2 (July 2010), pp. 1248–1252. ISSN: 0035-8711. DOI: 10.1111/j.1365-2966.2010.16752.x.

[204] R. Sari and T. Piran. "Hydrodynamic Timescales and Temporal Structure of Gamma-Ray Bursts." In: *ApJ Letters* 455 (Dec. 1995), p. L143. DOI: 10.1086/309835.

[205] R. Sari, T. Piran, and R. Narayan. "Spectra and Light Curves of Gamma-Ray Burst Afterglows." In: *ApJ Letters* 497.1 (Apr. 1998), pp. L17–L20. DOI: 10.1086/311269.

[206] V. Savchenko et al. "INTEGRAL Detection of the First Prompt Gamma-Ray Signal Coincident with the Gravitational-wave Event GW170817." In: *Astrophysical Journal Letters* 848.2, L15 (Oct. 2017), p. L15. DOI: 10.3847/2041-8213/aa8f94.

[207] M. Sawicki. "SEDfit: Software for Spectral Energy Distribution Fitting of Photometric Data." In: *Publications of the Astronomical Society of the Pacific* 124.921 (2012), p. 1208. DOI: 10.1086/668636.

[208] B. F. Schutz. "Determining the Hubble constant from gravitational wave observations." In: *Nat* 323.6086 (Sept. 1986), pp. 310–311. DOI: 10.1038/323310a0.

[209] B. F. Schutz. "Networks of gravitational wave detectors and three figures of merit." In: *Classical and Quantum Gravity* 28.12 (2011), p. 125023. DOI: 10.1088/0264-9381/28/12/125023.

[210] L. I. Sedov. *Similarity and Dimensional Methods in Mechanics*. Academic Press, New York, 1959.

[211] Y. Sekiguchi, K. Kiuchi, K. Kyutoku, M. Shibata, and K. Taniguchi. "Dynamical mass ejection from the merger of asymmetric binary neutron stars: Radiation-hydrodynamics study in general relativity." In: *Phys. Rev. D* 93.12 (2016). DOI: 10.1103/physrevd.93.124046.

[212] D. M. Siegel. "GW170817 –the first observed neutron star merger and its kilonova: Implications for the astrophysical site of the r-process." In: *The European Physical Journal A* 55.11 (Nov. 2019). ISSN: 1434-601X. DOI: 10.1140/epja/i2019-12888-9.

[213] L. Singer. *Data-driven expectations for electromagnetic counterpart searches based on LIGO/Virgo public alerts: O4 simulations*. This Zenodo entry is part 1 of 4 of a multi-entry dataset. This entry contains simulations for O4. 2021. DOI: 10.5281/zenodo.4765750.

[214] L. Singer. *Data-driven expectations for electromagnetic counterpart searches based on LIGO/Virgo public alerts: O5 simulations*. This Zenodo entry is part 1 of 4 of a multi-entry dataset. This entry contains simulations for O5. 2021. DOI: 10.5281/zenodo.4765752.

[215] J. Skilling. "Nested Sampling." In: *AIP Conference Proceedings* 735.1 (Nov. 2004), pp. 395–405. ISSN: 0094-243X. DOI: 10.1063/1.1835238.

[216] J. Skilling. "Nested sampling for general Bayesian computation." In: *Bayesian Analysis* 1.4 (2006), pp. 833 –859. DOI: 10.1214/06-BA127.

[217] R. J. E. Smith, G. Ashton, A. Vajpeyi, and C. Talbot. "Massively parallel Bayesian inference for transient gravitational-wave astronomy." In: *MNRAS* 498.3 (Aug. 2020), pp. 4492–4502. DOI: 10.1093/mnras/staa2483.

[218] V. Smolčić et al. "The VLA-COSMOS 3 GHz Large Project: Continuum data and source catalog release." In: *A&A* 602 (2017), A1. DOI: 10.1051/0004-6361/201628704.

[219] J. S. Speagle. "dynesty: a dynamic nested sampling package for estimating Bayesian posteriors and evidences." In: *MNRAS* 493.3 (Feb. 2020), pp. 3132–3158. ISSN: 0035-8711. DOI: 10.1093/mnras/staa278.

[220] G. Tagliaferri et al. "An unexpectedly rapid decline in the X-ray afterglow emission of long γ-ray bursts." In: *Nature* 436.7053 (Aug. 2005), pp. 985–988. DOI: 10.1038/nature03934.

[221] G. Taylor. "The Formation of a Blast Wave by a Very Intense Explosion. I. Theoretical Discussion." In: *Proceedings of the Royal Society of London Series A* 201.1065 (Mar. 1950), pp. 159–174. DOI: 10.1098/rspa.1950.0049.

[222] S. R. Taylor, J. R. Gair, and I. Mandel. "Cosmology using advanced gravitational-wave detectors alone." In: *Physical Review D* 85.2 (2012). DOI: 10.1103/physrevd.85.023535.

[223] E Troja, H van Eerten, G Ryan, R Ricci, J. M. Burgess, M. H. Wieringa, L Piro, S. B. Cenko, and T Sakamoto. "A year in the life of GW 170817: the rise and fall of a structured jet from a binary neutron star merger." In: *MNRAS* 489.2 (Aug. 2019), pp. 1919–1926. ISSN: 0035-8711. DOI: 10.1093/mnras/stz2248.

[224] E Troja, H van Eerten, B Zhang, G Ryan, L Piro, R Ricci, B O'Connor, M. H. Wieringa, S. B. Cenko, and T Sakamoto. "A thousand days after the merger: Continued X-ray emission from GW170817." In: *MNRAS* 498.4 (2020), 5643–5651. ISSN: 1365-2966. DOI: 10.1093/mnras/staa2626.

[225] E. Troja, B. O'Connor, G. Ryan, L. Piro, R. Ricci, B. Zhang, T. Piran, G. Bruni, S. B. Cenko, and H. van Eerten. "Accurate flux calibration of GW170817: is the X-ray counterpart on the rise?" In: *MNRAS* 510.2 (Feb. 2022), pp. 1902–1909. DOI: 10.1093/mnras/stab3533.

[226] E. Troja, L. Piro, G. Ryan, H. van Eerten, R. Ricci, M. H. Wieringa, S. Lotti, T. Sakamoto, and S. B. Cenko. "The outflow structure of GW170817 from late-time broad-band observations." In: *MNRAS* 478.1 (July 2018), pp. L18–L23. DOI: 10.1093/mnrasl/sly061.

[227] E. Troja et al. "The X-ray counterpart to the gravitational-wave event GW170817." In: *Nature* 551.7678 (Nov. 2017), pp. 71–74. DOI: 10.1038/nature24290.

[228] E. Troja et al. "A nearby long gamma-ray burst from a merger of compact objects." In: *Nature* 612.7939 (2022), pp. 228–231. DOI: 10.1038/s41586-022-05327-3.

[229] C. S. Unnikrishnan. "LIGO-India: A Decadal Assessment on Its Scope, Relevance, Progress, and Future." In: *arXiv e-prints*, arXiv:2301.07522 (Jan. 2023), arXiv:2301.07522. DOI: 10.48550/arXiv.2301.07522.

[230] S. A. Usman, J. C. Mills, and S. Fairhurst. "Constraining the Inclinations of Binary Mergers from Gravitational-wave Observations." In: *ApJ* 877.2 (2019), p. 82. DOI: 10.3847/1538-4357/ab0b3e.

[231] L. Verde, T. Treu, and A. G. Riess. "Tensions between the early and late Universe." In: *Nature Astronomy* 3.10 (2019), pp. 891–895. DOI: 10.1038/s41550-019-0902-0.

[232] M. Vietri. "GeV Photons from Ultrahigh Energy Cosmic Rays Accelerated in Gamma Ray Bursts." In: *Phys. Rev. Lett.* 78.23 (June 1997), pp. 4328–4331. DOI: 10.1103/PhysRevLett.78.4328.

[233] V. A. Villar et al. "The Combined Ultraviolet, Optical, and Near-infrared Light Curves of the Kilonova Associated with the Binary Neutron Star Merger GW170817: Unified Data Set, Analytic Models, and Physical Implications." In: *ApJ* 851.1 (2017), p. L21. DOI: 10.3847/2041-8213/aa9c84.

[234] J. Villasenor, D. Lamb, G. Ricker, et al. "Discovery of the short gamma-ray burst GRB 050709." In: *Nature* 437 (Oct. 2005), pp. 855–858. DOI: 10.1038/nature04213.

[235] L. Wade, J. D. E. Creighton, E. Ochsner, B. D. Lackey, B. F. Farr, T. B. Littenberg, and V. Raymond. "Systematic and statistical errors in a Bayesian approach to the estimation of the neutron-star equation of state using advanced gravitational wave detectors." In: *Phys. Rev. D* 89 (10 2014), p. 103012. DOI: 10.1103/PhysRevD.89.103012.

[236] H. Wang and D. Giannios. "Multimessenger Parameter Estimation of GW170817: From Jet Structure to the Hubble Constant." In: *ApJ* 908.2 (2021), p. 200. DOI: 10.3847/1538-4357/abd39c.

[237] Y.-Y. Wang, S.-P. Tang, Z.-P. Jin, and Y.-Z. Fan. "The Late Afterglow of GW170817/GRB 170817A: A Large Viewing Angle and the Shift of the Hubble Constant to a Value More Consistent with the Local Measurements." In: *ApJ* 943.1 (2023), p. 13. DOI: 10.3847/1538-4357/aca96c.

[238] Y.-Y. Wang, S.-P. Tang, X.-Y. Li, Z.-P. Jin, and Y.-Z. Fan. "Prospects of calibrating afterglow modeling of short GRBs with gravitational wave inclination angle measurements and resolving the Hubble tension with a GW-GRB association event." In: *Phys. Rev. D* 106.2 (2022). DOI: 10.1103/physrevd.106.023011.

[239] E. Waxman, S. R. Kulkarni, and D. A. Frail. "Implications of the Radio Afterglow from the Gamma-Ray Burst of 1997 May 8." In: *ApJ* 497.1 (1998), p. 288. DOI: 10.1086/305467.

[240] E. Waxman. "γ-Ray Burst Afterglow: Confirming the Cosmological Fireball Model." In: *ApJ* 489.1 (1997), p. L33. DOI: 10.1086/310960.

[241] J. Weber. "Detection and Generation of Gravitational Waves." In: *Phys. Rev.* 117 (1 1960), pp. 306–313. DOI: 10.1103/PhysRev.117.306.

[242] L. Wen and Y. Chen. "Geometrical expression for the angular resolution of a network of gravitational-wave detectors." In: *Phys. Rev.D* 81.8, 082001 (Apr. 2010), p. 082001. DOI: 10.1103/PhysRevD.81.082001.

[243] R. A. M. J. Wijers, M. J. Rees, and P. Mészáros. "Shocked by GRB 970228: the afterglow of a cosmological fireball." In: *MNRAS* 288.4 (July 1997), pp. L51–L56. ISSN: 0035-8711. DOI: 10.1093/mnras/288.4.L51.

[244] C. M. Will. "The Confrontation between General Relativity and Experiment." In: *Living Rev. Relativ.* 14 (2014), p. 4. DOI: 10.12942/lrr-2014-4.

[245] R. Willingale et al. "Testing the Standard Fireball Model of Gamma-Ray Bursts Using Late X-Ray Afterglows Measured by Swift." In: *ApJ* 662.2 (June 2007), pp. 1093–1110. DOI: 10.1086/517989.

[246] R. T. Wollaeger, C. L. Fryer, E. A. Chase, C. J. Fontes, M. Ristic, A. L. Hungerford, O. Korobkin, R. O'Shaughnessy, and A. M. Herring. "A Broad Grid of 2D Kilonova Emission Models." In: *ApJ* 918.1, 10 (Sept. 2021), p. 10. DOI: 10.3847/1538-4357/ac0d03.

[247] K. C. Wong et al. "HoLiCOW – XIII. A 2.4 per cent measurement of Ho from lensed quasars: 5.3σ tension between early- and late-Universe probes." In: *MNRAS* 498.1 (2019), pp. 1420–1439. DOI: 10.1093/mnras/stz3094.

[248] S. E. Woosley. "Gamma-Ray Bursts from Stellar Mass Accretion Disks around Black Holes." In: *ApJ* 405 (Mar. 1993), p. 273. DOI: 10.1086/172359.

[249] K. Yagi and N. Yunes. "Love number can be hard to measure." In: *Phys. Rev. D* 89 (2 2014), p. 021303. DOI: 10.1103/PhysRevD.89.021303.

[250] S. A. Yost, F. A. Harrison, R. Sari, and D. A. Frail. "A Study of the Afterglows of Four Gamma-Ray Bursts: Constraining the Explosion and Fireball Model." In: *ApJ* 597.1 (2003), p. 459. DOI: 10.1086/378288.

[251] W. Yuan, C. Zhang, Y. Chen, and Z. Ling. "The Einstein Probe Mission." In: *Handbook of X-ray and Gamma-ray Astrophysics*. Springer Nature Singapore, 2022, pp. 1–30. DOI: 10.1007/978-981-16-4544-0_151-1.

[252] B.-B. Zhang, B. Zhang, E.-W. Liang, Y.-Z. Fan, X.-F. Wu, A. Pe'er, A. Maxham, H. Gao, and Y.-M. Dong. "A Comprehensive Analysis of Fermi Gamma-ray Burst Data. I. Spectral Components and the Possible Physical Origins of LAT/GBM GRBs." In: *ApJ* 730.2, 141 (Apr. 2011), p. 141. DOI: 10.1088/0004-637X/730/2/141.

[253] B. Zhang. "Synchrotron radiation in Γ-ray bursts prompt emission." In: *Nature Astronomy* 4.3 (2020), pp. 210–211. DOI: 10.1038/s41550-020-1041-3.

[254] B. Zhang, Y. Z. Fan, J. Dyks, S. Kobayashi, P. Mészáros, D. N. Burrows, J. A. Nousek, and N. Gehrels. "Physical Processes Shaping Gamma-Ray Burst X-Ray Afterglow Light Curves: Theoretical Implications from the Swift X-Ray Telescope Observations." In: *ApJ* 642.1 (May 2006), pp. 354–370. DOI: 10.1086/500723.

[255] J. Zhang et al. "Estimate of the background and sensitivity of the follow-up X-ray telescope onboard Einstein Probe." In: *Astroparticle Physics* 137 (2022), p. 102668. ISSN: 0927-6505. DOI: https://doi.org/10.1016/j.astropartphys.2021.102668.